Diffusion and Precipitation Models for Silicon Gettering and Ultra Shallow Junction Formation

Hsiu-Wu Guo

A dissertation submitted in partial fulfillment
of the requirements for the degree of

Doctor of Philosophy

University of Washington

2008

Program Authorized to Offer Degree: Electrical Engineering

University of Washington
Graduate School

This is to certify that I have examined this copy of a doctoral dissertation by

Hsiu-Wu Guo

and have found that it is complete and satisfactory in all respects,
and that any and all revisions required by the final
examining committee have been made.

Chair of the Supervisory Committee:

_____

Scott T. Dunham

Reading Committee:

_____

Scott T. Dunham

_____

Karl F. Böhringer

_____

Babak Parviz

Date: _____

Signature_____

Date_____

University of Washington

Abstract

Diffusion and Precipitation Models for Silicon Gettering and Ultra Shallow Junction Formation

Hsiu-Wu Guo

Chair of the Supervisory Committee:
Professor Scott T. Dunham
Electrical Engineering

The progress of MOSFET evolution in the IC industry over the past few years has relied on rapid miniaturization, new materials, or new structures. At the same time, more constraints on the level of metal contamination were established to maintain device characteristics and chip yield. A fully kinetic precipitation model (FKPM) was previously developed to describe the complex behavior of precipitates, which depended on the thermal history of the samples, and a reduced moment-based model (RKPM) further improved the computing efficiency. In this work, these models were further developed and adapted to study ultra shallow junction (USJ) formation and gettering processes.

Low energy implantation is necessary to achieve shallow dopant distribution in USJ formation. A very short annealing at high temperature follows to ensure high dopant activation and minimize dopant diffusion. Modeling of transient enhance diffusion (TED) was performed with the incorporation of interstitial clusters and 311 defects. In addition, it is known that C can provide a highly efficient sink for excess interstitials during the annealing process. C diffusion path and clustering mechanisms were confirmed by utilizing ab-initio calculations. Studies of stress effects on TED and C diffusion/clustering were done to provide insightful guidance for optimizing the fabrication processes.

Metal contamination degrades gate oxide integrity and increases leakage currents. Gettering is a common method to reduce these unintentional metal impurities in the electrical

active regions of semiconductor devices. This work includes modeling of the Cu out-diffusion process, and iron gettering via ion implantation. Through simulations based on physically-based models, gettering behavior over a wide range of conditions can be well predicted.

TABLE OF CONTENTS

Page

LIST OF FIGURES

LIST OF TABLES

GLOSSARY

AKPM: Analytical kinetic precipitation model.

BIC: Boron interstitial cluster.

BZ: Brillouin zone.

CMOS: Complementary metal-oxide-semiconductor.

DFA: Delta function approximation.

DFT: Density functional theory.

DLTS: Deep level transient spectroscopy.

EG: Extrinsic gettering.

EOR: End of range.

FEOL: Front end of line.

FKPM: Full kinetic precipitation model.

FZ: Float zone.

GGA: Generalized gradient approximation.

HRTEM: High resolution transmission electron microscopy.

HTST: Harmonic transition state theory.

IC: Integrated circuits.

IG: Intrinsic gettering.

ITRS: International technology roadmap for semiconductors.

KLMC: Kinetic lattice Monte Carlo.

MBE: Molecular beam epitaxy

MOSFET: Metal oxide semiconductor field effect transistor.

NEB: Nudged elastic band.

NMOS: Negative-channel metal-oxide-semiconductor.

ORTC: Overall roadmap technology characteristics.

PMOS: Positive-channel metal-oxide-semiconductor.

RFKPM: Rediscretized full kinetic precipitation model.

RKPM: Reduced-moment based precipitation model.

RTA: Rapid thermal anneal.

S/D: Source/drain.

SEM: Scanning electron microscopy.

SIMS: Secondary ion mass spectroscopy.

SOI: Silicon-on-insulator.

SRH: Shockley-Read-Hall.

SRP: Spreading resistance profiling.

TCAD: Technology computer aided design.

TED: Transient enhanced diffusion.

TEM: Transmission electron microscopy.

TID: Transient ion drift.

TXRF: Total reflection X-ray fluorescence.

USJ: Ultra shallow junction.

VASP: Vienna *ab-initio* simulation package.

VLSI: Very large scale integration.

XRF: X-ray fluorescence.

XTEM: Cross-sectional transmission electron microscopy.

ACKNOWLEDGMENTS

First I would like to express my gratitude to Professor Scott T. Dunham for his guidance and support throughout my research. I thank him for his inspirational insight and knowledge in process and device simulation. His encouragement to present at international conferences leads to many opportunities for me to see more advanced research. Next, I would like to thank my committee members: Babak Parviz, Karl Böhringer, Tai-Chang Chen, and J. Nathan Kutz for their valuable suggestions and assistance in reading my dissertation.

Several funding supports include Semiconductor Research Corporation (SRC), Silicon Wafer Engineering and Defect Science (SiWEDS), and Washington Technology Center (WTC). I also thank our system administration, leaded by Lee Damon, for providing an excellent computing environment. Much appreciation goes to Intel and AMD for donating computing clusters, which were used for all the calculations.

Special thanks to Dr. Chen-Luen Shih, who graduated from our group in 2005. It was a pleasure sharing a lab with him and many enjoyable discussions both personal and professional. The knowledge he passed on to me in performing experiments and operating characterization tools broadened my research area substantially. I would also like to thank all of the previous and current members of the Nanotechnology Modeling Group (NTML): Zudian Qin, Milan Diebel, Chen-Luen Shih, Chihak Ahn, Kjersti Kleven, Rui Deng, Baruch Feldman, Bart Trzynadlowski, Phillip Liu, Haoyu Lai, Renyu Chen, etc. I am particularly thankful to Kjersti Kleven for revising my manuscript.

Many thanks to other friends in Seattle who enriched my experience while at the University of Washington. The Marinos (Kristi, Bradley and Deborah, William and Rose, Joseph and Tara, and Anthony) were always there as my own family. I would like to mention my Taiwanese friends who shared a lot of the same experience in study abroad and many

potluck parties together: Celest Lee, Chinwan Wang, Li-Chia Feng, Chloe Lee, Ying-Ju Lee and Chih-Peng Hsu, and the Hang family. Also thank you to Oliver Röhn, Robert Baxter, Lindsay Craig, and friends from FIUTS 2001 for the many great times we had together from BBQs and dinner parties to road trips and game nights.

I give the greatest gratitude to my loving family in Taiwan (my parents: Pao-Fu and Lee-Ching; and my brothers: Shih-Ho and Shih-Men). My parents always encouraged, guided, and provided me with all means to pursue my education. This task would not have been possible without their support.

At last, but not least, I like to express my appreciation to my fiancé: Kristi Lynn Marino.

DEDICATION

To my parents,

Pao-Fu and Lee-Ching,

my fiancé,

Kristi.

Chapter 1

INTRODUCTION

Rapid scaling of the metal-oxide-semiconductor field-effect transistor (MOSFET) has driven the silicon industry after the first experimental observation of the transistor at Bell Laboratories in 1947 [136]. In the early stage of transistor scaling, Gordon Moore postulated in 1945 that the number of transistors on a chip would increase exponentially over time [50, 51] and this has held as the feature size decreased exponentially from micrometers to nanometers. In the last two decades, *the International Technology Roadmap for Semiconductors* (ITRS) [1] has presented a world-wide consensus on the research and development required to meet Moore's law. Table. 1.1 shows the 2005 technology requirements for current and future devices. Future progress requires new materials and device structures to fulfill the challenge set by ITRS. Both commercially employed strained silicon [150] and silicon-on-insulator (SOI) [133] can increase the performance of the MOSFET without scaling channel length. In an example of MOSFETs at the 90-nm logic technology node (Fig. 1.1) [150], stress was introduced to enhance the carrier mobility using a novel low cost process flow. Other research work has been focused on the ultra thin body devices, carbon nanotubes, and III-V materials to improve the device performance. Furthermore, high-k/metal-gate material and self-aligned silicide for gate and contact are expected to be widely adopted in 45-nm logic technology node.

Due to the extremely high cost of fabrication processes, technology computer aided design (TCAD) is used to provide an economical way to study materials and devices. The effective application of TCAD requires substantial development of physical models from atomistic to continuum levels. In this work, we focus on the modeling and simulation in the area of front end of line processes (FEOL). ITRS pointed out that modeling of ultra-shallow-junction (USJ) formation is one of the key challenges. Approaches include very low

Table 1.1: Overall Roadmap Technology Characteristic (ORTC) table for the 2005 ITRS [1].

Year of production	2005	2007	2010	2013	2016
DRAM stagger-contacted (M1) 1/2 pitch [nm]	80	65	45	32	22
MPU/ASIC stagger-contacted (M1) 1/2 pitch [nm]	90	68	45	32	22
Flash Unconnected Poly Si 1/2 pitch [nm]	76	57	40	28	20
MPU printed gate length [nm]	54	42	30	21	15
MPU physical gate length [nm]	32	25	18	13	9

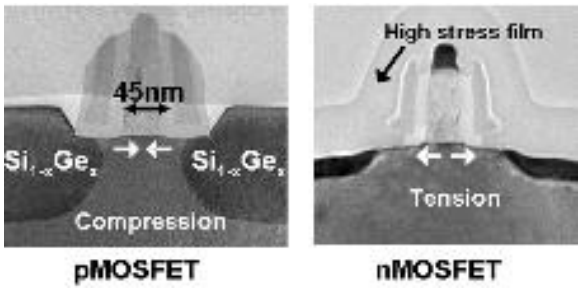

Figure 1.1: TEM images of 90-nm p-type and n-type MOSFET from Thompson *et al.* [150]. Uniaxial strain is introduced using $Si_{1-x}Ge_x$ in source and drain regions for p-type MOSFET, while Si nitride-capping layer gives large tensile stress to n-type MOSFET.

energy implantation (<500 eV) with particular focus on thermal annealing and diffusion of dopants [1]. With the incorporation of stress/strain in the modern device, such as 90-nm MOSFETs shown in Fig. 1.1, modeling of stress and its influence on dopant diffusion and activation becomes necessary.

This work is categorized into two main parts in order to understand and overcome the issues of "*contamination*" and "*dopant diffusion.*" Wafer cleaning and surface preparation continue to evolve in parallel to the development of future devices. Metal contamination degrades the integrity of gate dielectrics, because the impurity atoms tend to precipitate at the silicon/gate dielectric interface, which lowers the gate dielectric breakdown voltage [65], and become recombination/generation centers for free carriers. Therefore, ITRS requires

the critical metal concentration to be below $0.5\times10^{10}\text{cm}^{-2}$ at the gate dielectric interface and $1\times10^{10}\text{cm}^{-2}$ at other surface [1]. Gettering is a common method to reduce these unintentional metal impurities in the electrically active regions of semiconductor devices. It dissolves unwanted metal impurities followed by their diffusion to and capture in the regions where they do not have an impact on device performance. The work on gettering includes modeling of the copper out-diffusion process, which has a strong dependence on the surface conditions, and iron gettering via ion implantation.

In today's technology, dopant atoms are commonly introduced through ion implantation to give accurate dose and distribution. To accompany the scaling of semiconductor devices, the doping concentrations at source/drain (S/D) regions need to be increased in order to keep the sheet resistance low at the junctions. The challenge of controlling "*dopant diffusion*" arises at such small feature sizes, when both high doping and dopant activation have to be simultaneously achieved. Ion implantation creates substantial damage (excess interstitials (I) and vacancies (V)) in the lattice which must be repaired by subsequent annealing at high temperature. These excess point defects can either form clusters, recombine with each other, or diffuse and recombine at the surface during the annealing process. {311} and dislocation loops are the products of I clustering process, which control the level of excess interstitials. From a microscopic view, dopant atoms diffuse with the assistance of the excess point defects, leading to challenges in the formation of USJ. B atoms diffuse via interstitial mechanism, and a substantial amount of B diffusion is observed during annealing due to the transient interstitial supersaturation, a phenomenon which is known as transient-enhanced diffusion (TED). In addition, the implanted dopant atoms must a occupy lattice site to contribute to the electrical activity. However, the formation of electrically-inactive dopant-interstitial pairs often occurs under the presence of excess interstitials during this high temperature annealing. Therefore, high temperature and short annealing time are desired to minimize the TED effect and further increase the dopant activation. Rapid thermal annealing (RTA) and laser thermal annealing are currently the common method to fulfill this goal.

A background review of impurity diffusion is first given including point defects, dopants, and metals in Chapter 2. Kinetic precipitation models [19, 31, 40, 135] are discussed, fol-

lowed by the incorporation of delta-function approximation (DFA) in Chapter 3. These precipitation models are used to study the gettering mechanism for both copper and iron in Chapter 4. Furthermore, we are able to investigate the boron diffusion and activation in Chapter 5 by using the reduced moment-based kinetic precipitation model (RKPM) with DFA. The stress effects on TED and {311} evolution are also addressed by using the results from Ahn's *ab-initio* calculations [2]. In Chapter 6, using first-principles calculations and kinetic Monte Carlo simulations, we study the stress effects on C diffusion and clustering mechanisms in silicon. Finally, Chapter 7 summarizes this work and gives directions for future work.

Chapter 2

IMPURITY DIFFUSION IN SILICON

Diffusion in silicon is an elementary process step in the fabrication of today's integrated circuits. Fick's laws have formed the basis for the understanding and prediction of diffusion profiles. However, the general solutions require the diffusivity to be constant over time and space during a particular process step. In real VLSI fabrication sequences, these constraints are rarely met. Therefore, numerical solutions with modifications of Fick's laws are necessary for better understanding the physics of diffusion, and predicting resulting profiles.

Point defects can be categorized in two groups: *native point defects* and *impurity-related defects* [35]. Native point defects, such as vacancies, interstitials, and interstitialcies, exist in the pure silicon lattice, while impurity-related defects are the foreign impurities introduced into the silicon lattice. Group-III elements (B, Al, Ga, and In) and Group-V elements (P, As, and Sb) are a special class of impurities known as *dopants*.

In Chapter 2, the properties of point defects are first discussed in Section 2.1 because of their involvement in impurity diffusion (Section 2.2). Solubilities and diffusivities of relevant 3d transition metals are discussed in Section 2.3.

2.1 Properties of Native Point Defects

Point defects are limited in size to atomic dimensions. An impurity atom can be considered as a point defect. However, we often limit the definition of point defects to include only the native point defects (or intrinsic point defects), which are vacancy, interstitial, and interstitialcy. A *vacancy* (V) is defined as an empty lattice site. An *interstitial* is a silicon atom sitting in one of the interstices of the silicon lattice. Tetrahedral and hexagonal interstitials are the two possible configurations with the highest symmetry. An *interstitialcy* consists of two Si atoms in a lattice site, or any small region of silicon with more atoms than in an ideal crystal. Both *interstitials* and *interstitialcies* are commonly referred to as self-

interstitials, silicon interstitials, or, simply, interstitials (I), since they are indistinguishable at the continuum scale.

Under equilibrium conditions, point defects can be created as Frenkel pairs in the bulk or generated independently from the surface. Frenkel pairs are the results of Si atoms leaving their substitutional lattice sites and creating a pair of point defects (I and V).

$$\mathrm{I} + \mathrm{V} \Longleftrightarrow \emptyset \tag{2.1}$$

In equilibrium, the number of I and V does not have to be equal due to independent surface recombination. In the case of a surface generation process, an interstitial is created by a Si atom at the surface moving into the bulk, while a vacancy is created by a substitutional Si atom relocating to the surface.

Under non-equilibrium conditions, ion implantation damage introduces both interstitials and vacancies, where the vacancy-rich region is usually closer the surface. Oxidation at the silicon surface injects interstitials into the bulk [14, 83, 131, 139], while nitridation generates vacancies (or extracts I) [26, 81]. Dislocations can also serve as both sources and sinks of point defects.

From thermodynamics, the Gibbs Free Energy (G) tends to be a minimum,

$$G = H - TS. \tag{2.2}$$

H is enthalpy, which is lowest for the perfect crystal. Entropy, S, is a measure of disorder and T is the temperature. One can calculate the equilibrium concentrations for point defects (X) by minimizing the Gibbs Free Energy (G) [35].

$$\frac{C_{\mathrm{X}}}{C_{\mathrm{Si}}} = \theta_{\mathrm{X}} \exp\left[\frac{S_{\mathrm{X}}^{f}}{k}\right] \exp\left[-\frac{H_{\mathrm{X}}^{f}}{kT}\right] \tag{2.3}$$

C_{Si} is the number of the available lattice sites in crystal, H_{X}^{f} and S_{X}^{f} represents the formation enthalpy and entropy, and θ_{X} is the number of degrees of internal freedom for the defect on a site.

2.1.1 Point Defects in Multiple Charge States

It is well established that point defects can exist in different multiple charge states [35]. They exhibit deep energy levels within the bandgap, and the ionization depends on the

location of the Fermi level in the system. Acceptor (donor) behavior is shown when Fermi level is above (below) the deep energy level. Shockley and Last *et al.* [137] presented the point defect concentrations of the charged states to be directly related to the concentration of neutral defects as

$$\frac{C_{\mathrm{X}^-}}{C_{\mathrm{X}^0}} = \frac{\theta_{\mathrm{X}^-}}{\theta_{\mathrm{X}^0}} \exp\left(-\frac{E_{\mathrm{X}^-} - E_f}{kT}\right) \tag{2.4}$$

$$\frac{C_{\mathrm{X}^=}}{C_{\mathrm{X}^0}} = \frac{\theta_{\mathrm{X}^=}}{\theta_{\mathrm{X}^0}} \exp\left(-\frac{E_{\mathrm{X}^=} + E_{\mathrm{X}^-} - 2E_f}{kT}\right) \tag{2.5}$$

$$\frac{C_{\mathrm{X}^+}}{C_{\mathrm{X}^0}} = \frac{\theta_{\mathrm{X}^+}}{\theta_{\mathrm{X}^0}} \exp\left(-\frac{E_f - E_{\mathrm{X}^+}}{kT}\right) \tag{2.6}$$

$$\frac{C_{\mathrm{X}^{++}}}{C_{\mathrm{X}^0}} = \frac{\theta_{\mathrm{X}^{++}}}{\theta_{\mathrm{X}^0}} \exp\left(-\frac{2E_f - E_{\mathrm{X}^{++}} - E_{\mathrm{X}^+}}{kT}\right), \tag{2.7}$$

where

$$\frac{C_{\mathrm{X}^0}}{C_S} = \theta_{\mathrm{X}^0} \exp\left[\frac{S^f_{\mathrm{X}^0}}{k}\right] \exp\left[-\frac{H^f_{\mathrm{X}^0}}{kT}\right]. \tag{2.8}$$

E_{X^-}, $E_{\mathrm{X}^=}$, E_{X^+}, and $E_{\mathrm{X}^{++}}$ are the positions of deep energy levels for point defects within the silicon bandgap [126].

2.1.2 Self-Diffusion of Point Defects

The migration of point defects includes the movements of interstitials, interstitialcies, vacancies and dopant/defect pairs. Here we focus on the diffusion of point defects (X) only. For simplicity, we consider only two charged states (X^0 and X^+), but the analysis is easily generalized. Using Fick's first law, the self-diffusion of point defects, including the different charge states, can be expressed as [35]

$$J^{\mathrm{total}}_{\mathrm{X}} = -d^{\mathrm{eff}}_{\mathrm{X}} \frac{C^{\mathrm{total}}_{\mathrm{X}}}{\partial x}, \tag{2.9}$$

where

$$d^{\mathrm{eff}}_{\mathrm{X}} = d_{\mathrm{X}^0} \frac{C_{\mathrm{X}^0}}{C_{\mathrm{X}^0} + C_{\mathrm{X}^+}} + d_{\mathrm{X}^+} \frac{C_{\mathrm{X}^+}}{C_{\mathrm{X}^0} + C_{\mathrm{X}^+}}. \tag{2.10}$$

The effective diffusivity depends on the relative point defect concentrations in different charge states, which gives a Fermi level dependence. The diffusion of point defects via dopant/defect complexes will be discussed in Section 2.2.

2.2 Dopant Diffusion

Dopant diffusion is discussed commonly from either a macroscopic or a microscopic viewpoint. The macroscopic viewpoint considers the overall motion of a dopant profile and predicts the diffusion process via Fick's first law

$$F = -D_{\mathrm{A}} \frac{\partial C_{\mathrm{A}}}{\partial x}, \tag{2.11}$$

where F is the flux. D_{A} and $\partial C_{\mathrm{A}}/\partial x$ are the diffusivity and concentration gradient. D_{A} is usually extrapolated by fitting an Arrhenius equation to the experimental measurements.

$$D_{\mathrm{A}} = D_{\mathrm{A}_0} \exp\left(-\frac{E_m^{\mathrm{A}}}{kT}\right) \tag{2.12}$$

D_{A_0} is the diffusion prefactor, and E_m^{A} is the *apparent activation energy* of diffusion, also known as the migration barrier.

The microscopic viewpoint explains that diffusion is mediated by a point defect X (I or V) at the atomic level. The corresponding diffusivity under an intrinsic doping condition is given by

$$D_{\mathrm{AX}} = d_{\mathrm{AX}} \left(-\frac{C_{\mathrm{AX}}}{C_{\mathrm{A}}}\right). \tag{2.13}$$

D_{A} $(= D_{\mathrm{AI}} + D_{\mathrm{AV}})$ is often measured from experiments.

In this section, we will first discuss the diffusion mechanisms via vacancy, interstitial, and interstitialcy. The coupled diffusion is followed by considering all the possible pairing and recombination reactions over all the charge states.

2.2.1 Dopant Diffusion Mechanisms

It is believed that dopant diffusion is intimately linked to point defects (interstitials and vacancies) on the atomic scale. P and B appear to have an enhanced diffusion because of the oxidation of silicon at the surface, while Sb has a retarded diffusion [126]. This variation is postulated to be due to the deviation of point defect concentrations from the equilibrium values caused by the surface oxidation. Oxidation-induced stacking faults are non-equilibrium defect structures, which grow only under supersaturated interstitial concentration [71]. We will discuss three mechanisms of how point defects interact with dopant atoms and diffuse away: (1) vacancy mechanism; (2) interstitial mechanism; (3) interstitialcy mechanism.

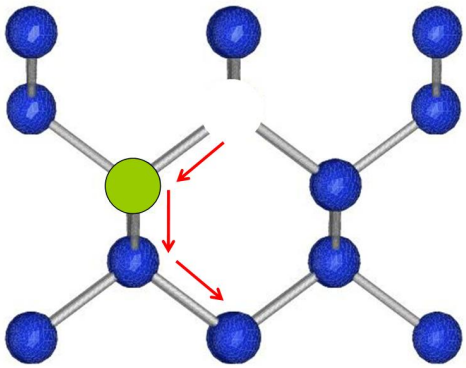

Figure 2.1: Schematic of vacancy diffusion-assisted mechanism [126]. The lightly colored atom is the dopant atom.

Vacancy diffusion mechanism

A substitutional dopant atom can migrate through the lattice by moving into an adjacent empty site, as shown in Fig. 2.1. After the exchange between the dopant atom and vacancy, the vacancy must diffuse away to at least a third-nearest neighbor from the dopant atom to complete one diffusion step in silicon [35].

Interstitial diffusion mechanism

Fig. 2.2 shows the dopant diffusion by the substitutional/interstitial interchange mechanism. A dopant atom is first displaced into an interstitial site, which can be referred to as the kick-out process [38]. This process is described by the reaction

$$\mathrm{A}_s + \mathrm{I} \Longleftrightarrow \mathrm{A}_i, \tag{2.14}$$

where an interstitial (I) kicks a dopant atom (A_s) from the lattice site into an interstitial location (A_i). Then the dopant atom migrates through the interstices as a dopant interstitial until it replaces a Si atom at a substitutional site. Alternatively, the interstitial dopant can

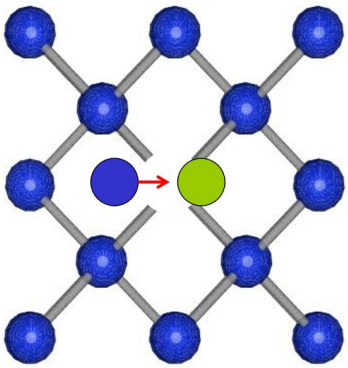

Figure 2.2: Schematic of interstitial-assisted (kick-out) diffusion mechanism [126]. A Si atom at the interstitial site first replaces the dopant atom at the lattice site. The dopant atom then diffuses through the interstices as a dopant interstitial until it kicks out another Si atom and takes up a substitutional site (kick-in).

fill a vacant site (Frank-Turnbull [37]). The following reaction describes this process as

$$\mathrm{A}_i + \mathrm{V} \Longleftrightarrow \mathrm{A}_s. \tag{2.15}$$

Interstitialcy diffusion mechanism

Fig. 2.3 shows the dopant diffusion by the substitutional/interstitialcy interchange mechanism. A dopant and silicon atom form a pair and share a lattice site [39]. This process is described as

$$\mathrm{A} + \mathrm{I} \Longleftrightarrow \mathrm{AI}. \tag{2.16}$$

The diffusing pair migrates through the lattice, until the pair breaks up leaving the dopant atom in a substitutional site and releasing the silicon interstitial. Note that the interstitial and interstitialcy mechanisms are similar in nature. Because they are mathematically equivalent, both mechanisms are often referred to as interstitial-assisted diffusion and considered

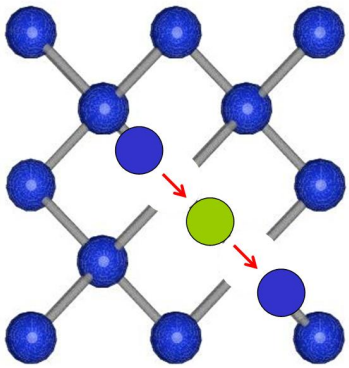

Figure 2.3: Schematic of interstitialcy-assisted diffusion mechanism [126]. The silicon interstitial and dopant atom occupy one lattice site, forming an interstitial-dopant pair, and diffuse to another lattice point.

the same throughout this work.

Dopant atoms may diffuse via either interstitial- or vacancy-assisted mechanisms by forming dopant/defect pairs. Dopant/defect pairs can also recombine with an opposite point defect leaving the dopant atom in a substitutional site. In the system, I, V, AI and AV are considered as mobile species, and the reactions between point defects, dopant atoms, and dopant/defect pairs are

$$\mathrm{I} + \mathrm{A} \iff \mathrm{AI} \tag{2.17}$$

$$\mathrm{V} + \mathrm{A} \iff \mathrm{AV} \tag{2.18}$$

$$\mathrm{I} + \mathrm{V} \iff \emptyset \tag{2.19}$$

$$\mathrm{I} + \mathrm{AV} \iff \mathrm{A} \tag{2.20}$$

$$\mathrm{V} + \mathrm{AI} \iff \mathrm{A} \tag{2.21}$$

$$\mathrm{AI} + \mathrm{AV} \iff 2\mathrm{A}, \tag{2.22}$$

where A is the dopant atom sitting at a substitutional site, I and V are point defects (interstitial and vacancy), and AI and AV are dopant/defect pairs.

In general, the reaction between A and B can be described as

$$\mathrm{A} + \mathrm{B} \Longleftrightarrow \mathrm{AB}. \tag{2.23}$$

The resulting net reaction rate is the difference between forward and reverse rates.

$$R_{\mathrm{A/B}} = k_f \left(C_{\mathrm{A}} C_{\mathrm{B}} - \frac{C_{\mathrm{AB}}}{K^{eq}_{\mathrm{AB}}} \right), \tag{2.24}$$

where C's are the respective concentrations, k_f is the forward reaction coefficient, $R_{\mathrm{A/B}}$ is the reaction rate per unit volume, and K^{eq}_{AB} represents the equilibrium constant. Under local equilibrium,

$$C_{\mathrm{AB}} = K^{eq}_{\mathrm{AB}}(T)\, C_{\mathrm{A}} C_{\mathrm{B}}. \tag{2.25}$$

Using Fick's first law, the sum of the dopant diffusion fluxes via interstitial- and vacancy-assisted mechanisms can then be expressed as

$$-J_{\mathrm{A}} = \sum_{\mathrm{X}} d_{\mathrm{AX}} \nabla C_{\mathrm{AX}}, \tag{2.26}$$

where A and X are the dopant and point defects. AX and d_{AX} are the diffusing pair and its diffusivity. The total dopant concentration is the sum of substitutional dopant ($\mathrm{C_{A_s}}$) and mobile dopant/defect pair (AI and AV) concentrations.

$$C_{\mathrm{A}} = C_{\mathrm{A_s}} + \sum_{\mathrm{X}} C_{\mathrm{AX}} \tag{2.27}$$

Taking the gradient of Eq. 2.25 on both sides,

$$\nabla C_{\mathrm{AX}} = K^{eq}_{\mathrm{AX}}(T) \left(C_{\mathrm{X}} \nabla C_{\mathrm{A_s}} + C_{\mathrm{A_s}} \nabla C_{\mathrm{X}} \right). \tag{2.28}$$

If there is no spatial variation in the point defect concentrations ($\nabla C_{\mathrm{X}} = 0$), as for an example under intrinsic and equilibrium conditions:

$$-J_{\mathrm{A}} = D_{\mathrm{A}} \nabla C_{\mathrm{A}} = \sum_{\mathrm{X}} d_{\mathrm{AX}} K^{eq}_{\mathrm{AX}} C_{\mathrm{X}} \nabla C_{\mathrm{A_s}}. \tag{2.29}$$

If the number of AX is small compared to the total A, ($C_{\mathrm{A_s}} \approx C_{\mathrm{A}}$), we can then obtain

$$D_{\mathrm{A}} = \sum_{\mathrm{X}} D_{\mathrm{AX}} = \sum_{X} d_{\mathrm{AX}} \frac{C_{\mathrm{AX}}}{C_{\mathrm{A}}}. \tag{2.30}$$

We can expand Eq. 2.30 in terms of the interstitial and vacancy concentrations as

$$D_{\mathrm{A}} = D_{\mathrm{AI}} + D_{\mathrm{AV}} = d_{\mathrm{AI}}\frac{C_{\mathrm{AI}}}{C_{\mathrm{A}}} + d_{\mathrm{AV}}\frac{C_{\mathrm{AV}}}{C_{\mathrm{A}}}, \tag{2.31}$$

where D_{AI} and D_{AV} are the contributions via interstitial and vacancy mechanisms. Note that they also include all the possible charge states for each point defect. After some mathematical manipulation,

$$\frac{D_{\mathrm{A}}}{D^*_{\mathrm{A}}} = \frac{D^*_{\mathrm{AI}}}{D^*_{\mathrm{A}}}\frac{D_{\mathrm{AI}}}{D^*_{\mathrm{AI}}} + \frac{D^*_{\mathrm{AV}}}{D^*_{\mathrm{A}}}\frac{D_{\mathrm{AV}}}{D^*_{\mathrm{AV}}} \tag{2.32}$$

$$= f_{\mathrm{I}}\frac{D_{\mathrm{AI}}}{{D_{\mathrm{AI}}}^*} + f_{\mathrm{V}}\frac{D_{\mathrm{AV}}}{D^*_{\mathrm{AV}}} \tag{2.33}$$

where * denotes the equilibrium condition. The fraction, $f_{\mathrm{I}} = D^*_{\mathrm{AI}}/D^*_{\mathrm{A}}$, indicates the proportion of diffusion via interstitial mechanism. D_{A} is the effective diffusivity of the dopant, while D^*_{A} represents the equilibrium diffusivity measured under inert conditions. By the definition, $f_{\mathrm{I}} + f_{\mathrm{V}} = 1$. Using Eqs. 2.25 and 2.30, Eq. 2.33 results in

$$\frac{D_{\mathrm{A}}}{D^*_{\mathrm{A}}} = f_{\mathrm{I}}\frac{C_{\mathrm{I}}}{C^*_{\mathrm{I}}} + f_{\mathrm{V}}\frac{C_{\mathrm{V}}}{C^*_{\mathrm{V}}}. \tag{2.34}$$

The overall dopant diffusivity is split into two components dominated by interstitial- and vacancy-assisted mechanisms. Eq. 2.34 gives the instantaneous dopant diffusivity when the point defect concentrations are perturbed from their equilibrium values. To capture the behavior of dopant diffusion, one needs to understand how point defect concentrations deviate from the equilibrium because of different process steps. However, there are no reliable ways to measure the interstitial or vacancy population directly via an experiment.

2.2.2 Dopant Coupled Diffusion

Earlier we mentioned in Section 2.1.1 that point defects can exist in different multiple charge states. Since donors and acceptors can be easily ionized, pairing between dopant/pair complexes with different charge states needs to be included. For a system containing a single acceptor species, A^-, Eqs. 2.17 to 2.22 should be modified as

$$\mathrm{A}^- + \mathrm{I}^j \Leftrightarrow (\mathrm{AI})^{-1+j}, \tag{2.35}$$

$$\mathrm{A}^- + \mathrm{V}^j \Leftrightarrow (\mathrm{AV})^{-1+j}, \tag{2.36}$$

$$\mathrm{I}^i + \mathrm{V}^j \quad \Leftrightarrow \quad (-i-j)e^-, \tag{2.37}$$

$$(\mathrm{AI})^i + \mathrm{V}^j \quad \Leftrightarrow \quad \mathrm{A}^- - (1+i+j)e^-, \tag{2.38}$$

$$(\mathrm{AV})^i + \mathrm{I}^j \quad \Leftrightarrow \quad \mathrm{A}^- - (1+i+j)e^-, \tag{2.39}$$

$$(\mathrm{AI})^i + (\mathrm{AV})^j \quad \Leftrightarrow \quad 2\mathrm{A}^- - (2+i+j)e^-, \tag{2.40}$$

where i and j represent charge states.

To describe the coupled diffusion, which is also known as the pair diffusion model [29, 35, 108, 109, 163, 164], reactions in Eqs. 2.35 to 2.40 are included. Dopant diffusion occurs through the formation of mobile pairs (dopant/point defect). The following continuity equations for five species, (I, V, A, AI, and AV), are included in this model.

$$\begin{aligned}
\frac{\partial C_{\mathrm{A}}}{\partial t} &= -R_{\mathrm{A/I}} - R_{\mathrm{A/V}} + R_{(\mathrm{AI})/\mathrm{V}} + R_{(\mathrm{AV})/\mathrm{I}} + 2R_{(\mathrm{AI})/(\mathrm{AV})} \\
\frac{\partial C_{(\mathrm{AI})}}{\partial t} &= -\nabla \cdot \vec{J}_{(\mathrm{AI})} + R_{\mathrm{A/I}} - R_{(AI)/V} - R_{(AI)/(AV)} \\
\frac{\partial C_{(\mathrm{AV})}}{\partial t} &= -\nabla \cdot \vec{J}_{(\mathrm{AV})} + R_{\mathrm{A/V}} - R_{(\mathrm{AV})/\mathrm{I}} - R_{(\mathrm{AI})/(\mathrm{AV})} \\
\frac{\partial C_{\mathrm{I}}}{\partial t} &= -\nabla \cdot \vec{J}_{\mathrm{I}} - R_{\mathrm{A/I}} - R_{\mathrm{I/V}} \\
\frac{\partial C_{\mathrm{V}}}{\partial t} &= -\nabla \cdot \vec{J}_{\mathrm{V}} - R_{\mathrm{A/I}} - R_{\mathrm{I/V}}
\end{aligned} \tag{2.41}$$

R's are the reaction rates between different species, corresponding to Eqs. 2.17 to 2.22. J's are the fluxes of mobile species, which include both diffusion and drift terms. The detailed derivations for all the reactions are given in Appendix A.

2.3 Metal Diffusion

The behavior of metal impurities depends on the properties of the respective impurity metal during different heat treatment, as well as the conditions at the sample surfaces. For a better understanding of 3d transition metal at elevated temperatures, one has to consider the following parameters [54]:

- The solubilities and diffusivities of respective impurities as a function of temperature.
- Surface conditions which determine the diffusion into and out of the silicon sample.
- The cooling rate at the end of the thermal process.
- The doping concentrations in the silicon sample which may affect the solubilities and

diffusivities of the impurities in extrinsic silicon.

In the following sections, we will first discuss the solubilities of relevant 3d metals. Atomistic diffusion mechanisms with the incorporation of point defects including all charged states will be followed. The diffusion and pairing with boron for copper and iron will be studied specifically as an illustration.

2.3.1 Metal Solid Solubility

The solid solubility is defined as the maximum concentration of an impurity that can be dissolved in silicon under equilibrium conditions at a given temperature. It is often written as function of the temperature (T) according to the following Arrhenius equation (similar to Eq. 2.3):

$$C_{ss} = C_{\mathrm{Si}} \exp\left(S_S - \frac{H_{\mathrm{M}}}{kT}\right), \qquad (T < T_{eut}) \tag{2.42}$$

where S_S and H_{M} stand for the solution entropy and enthalpy respectively, k is the Boltzmann constant, and C_{Si} is the concentration of available sites in silicon. Solubilities of the relevant 3d metals are shown in Table. 2.1. Note that Eq. 2.42 only holds for temperatures below eutectic temperature (T_{eut}). The solid solubility also depends on the surface conditions of the sample because the thermal equilibrium is adjusted by the balance of in- and out-diffusion of the impurity atoms at the sample surface.

Table 2.1: Solubilities of the 3d transition metals [54]. $C_{ss} = 5 \times 10^{22} \exp\left(S_S - H_{\mathrm{M}}/kT\right)$.

Metal	S_S	H_S	T region [°C]	C_{ss} (1100 °C)	Ref.
Ti	4.22	3.05	950-1200	2.1×10^{13}	[66]
Cr	4.7	2.79	900-1300	3.1×10^{14}	[158]
Mn	7.11	2.80	900-1200	3.2×10^{15}	[45, 158]
Fe	8.2	2.94	900-1200	2.9×10^{15}	[158]
Co	7.6	2.83	700-1100	4.0×10^{15}	[158]
Ni	3.2	1.68	500-950	5.0×10^{17}	[158]
Cu	2.4	1.49	500-800	8.0×10^{17}	[158]

2.3.2 An Atomic View of Metal Diffusion

Table. 2.2 shows the macroscopic diffusivity for some 3d metals. Before the diffusion of

Table 2.2: Diffusivities of the 3d transition metals [54]. $D = D_0 \exp\left(-E_m^{\mathrm{M}}/kT\right)$.

Metal	$D_0(\mathrm{cm}^{-2})$	E_m^{M}	T region [°C]	D (1100 °C)	Ref.
Ti	1.45×10^{-2}	1.79	900-1200	3.9×10^{-9}	[66]
Cr	1.0×10^{-2}	0.99	900-1250	2.3×10^{-6}	[53]
Mn	5.7×10^{-4}	0.6	900-1200	3.6×10^{-6}	[45]
Fe	1.3×10^{-3}	0.68	30-1200	4.1×10^{-6}	[158]
Co	4.2×10^{-3}	0.53	900-1100	4.7×10^{-5}	[47, 67]
Ni	2.0×10^{-3}	0.47	800-1300	3.8×10^{-5}	[53]
Cu	4.7×10^{-3}	0.43	400-900	1.2×10^{-4}	[53]

the metals (M) is discussed, it is necessary to describe the mechanism for making them mobile. Most of the metals considered in the gettering process either sit at substitutional lattice sites ($\mathrm{M_s}$) or interstitial sites ($\mathrm{M_i}$). Metals can diffuse through either state, but their diffusivity is generally higher by orders of magnitude in an interstitial state. This is partly due to breaking of bonds involved in the interstitial diffusion process. Some of the metals (e.g., Cu) have a much higher solubility in an interstitial form. On the other hand, some metals (e.g., Au and Pt) are more stable in a substitutional state, but diffuse rapidly once they become interstitials. In the latter case, it is necessary to know the mechanisms by which metals can become interstitials from the substitutional state. This can be explained through kick-out [38] (Eq. 2.14) or Frank-Turnbull [37] (Eq. 2.15) mechanisms, mentioned in Section 2.2.1. The reaction rate equations for Eqs. 2.14 and 2.15 are written as

$$R_{ko} = k_{ko}(C_{\mathrm{M}_i} - K_{ko}^{eq} C_{\mathrm{M}_s} C_{\mathrm{I}}) \tag{2.43}$$

$$R_{ft} = k_{ft}(C_{\mathrm{M}_i} C_{\mathrm{V}} - K_{ft}^{eq} C_{\mathrm{M}_s}) \tag{2.44}$$

where C's are the concentrations of the respective species, and K_{ko}^{eq} and K_{ft}^{eq} represent the thermal equilibrium constants. If the reaction is assumed to be diffusion limited, the forward rate coefficients, k's, can be approximated as

$$k_{ko} = 4\pi r_{ko} D_{\mathrm{M}_i} \tag{2.45}$$

$$k_{ft} = 4\pi r_{ft} (D_{\mathrm{V}} + D_{\mathrm{M}_i}) \tag{2.46}$$

where r is the effective capture radius for a certain reaction, and D's are the diffusivities.

Due to the fact that metal diffusion is assisted by point defects, I/V recombination ($R_{\mathrm{I/V}}$ in Eq. 2.19) needs to be included in the system as well. Assuming that substitutional metals are immobile, the full set of equations describing metal diffusion in the absence of pairing with dopant and precipitation can then be written as

$$\frac{\partial C_{\mathrm{M}_s}}{\partial t} = R_{ko} + R_{ft} \tag{2.47}$$

$$\frac{\partial C_{\mathrm{M}_i}}{\partial t} = -\nabla \cdot \vec{J}_{\mathrm{M}_i} - R_{ko} - R_{ft} \tag{2.48}$$

$$\frac{\partial C_{\mathrm{I}}}{\partial t} = -\nabla \cdot \vec{J}_{\mathrm{I}} + R_{ko} - R_{\mathrm{I/V}} \tag{2.49}$$

$$\frac{\partial C_{\mathrm{V}}}{\partial t} = -\nabla \cdot \vec{J}_{\mathrm{V}} - R_{ft} - R_{\mathrm{I/V}}, \tag{2.50}$$

where J's are the diffusion fluxes of mobile species including all charged states.

2.3.3 Cu

Copper not only diffuses interstitially, but also primarily sits at interstitial sites. Thus, substitutional copper can be neglected, giving a simple diffusion behavior uncoupled to point defects.

$$\frac{\partial C_{\mathrm{Cu}}}{\partial t} = \nabla \cdot (D_{\mathrm{Cu}} \nabla C_{\mathrm{Cu}}) \tag{2.51}$$

Due to the fact that metals exist in the positively charged (e.g., Cu^{+}) as well as neutral state (e.g., Cu^{0}), multiple charge states need to be included. Assuming that the electronic processes are fast,

$$C_{\mathrm{Cu}^{+}} = K_{\mathrm{Cu}^{+}} C_{\mathrm{Cu}^{0}} (p/n_i), \tag{2.52}$$

where K_{Cu^+} is equilibrium constant. The total C_{Cu} is the sum of concentrations in all charged states.

$$C_{\mathrm{Cu}} = C_{\mathrm{Cu}^0}\left[1 + K_{\mathrm{Cu}^+}(p/n_i)\right] \tag{2.53}$$

Using the same approach as in Appendix A for the dopant diffusion, we can combine the fluxes (both diffusion and drift) for all the charge states as

$$\frac{\partial C_{\mathrm{Cu}}}{\partial t} = \nabla \cdot \left\{ \left[D_{\mathrm{Cu}^0} + D_{\mathrm{Cu}^+} K_{\mathrm{Cu}^+}(p/n_i)\right] \nabla \frac{C_{\mathrm{Cu}}}{\left[1 + K_{\mathrm{Cu}^+}(p/n_i)\right]} \right\} \tag{2.54}$$

where D_{Cu^0} and D_{Cu^+} are the diffusivities for Cu^0 and Cu^+ respectively.

A positively charged copper atom (Cu^+) is likely to pair with an acceptor (B^-) in the bulk region, as described by Eq. 2.55. This pairing reaction will affect the copper diffusion and precipitation.

$$\mathrm{Cu}_i^+ + \mathrm{B}_s^- \longleftrightarrow \mathrm{CuB} \tag{2.55}$$

Under equilibrium conditions,

$$C_{\mathrm{CuB}} = K_{\mathrm{CuB}} C_{\mathrm{Cu}^+} C_{\mathrm{B}^-} \tag{2.56}$$

$$\begin{aligned} C_{\mathrm{Cu}} &= C_{\mathrm{Cu}^0} + C_{\mathrm{Cu}^+} + C_{\mathrm{CuB}} \\ &= C_{\mathrm{Cu}^0}[1 + K_{\mathrm{Cu}^+}(p/n_i)(1 + K_{\mathrm{CuB}} C_{\mathrm{B}^-})] \end{aligned} \tag{2.57}$$

where C_{CuB} is the concentration of CuB pairs, C_{Cu} is the total concentration of solute, and K_{CuB} is the thermal equilibrium pairing constant. The dissociation energy (E_{diss}) is the sum of binding energy (E_b) and the diffusion barrier height (E_d), which can be written as $E_{diss} \approx E_b + E_d$. The experimental studies of copper-acceptor dissociation energy reported by Wagner *et al.* [155] show that the dissociation energy (E_{diss}) varies with different acceptors (0.61 eV for CuB). To include the CuB pairing in a boron-doped silicon, Eq. 2.54 has to be modified as:

$$\frac{\partial C_{\mathrm{Cu}}}{\partial t} = \nabla \cdot \left\{ \left[D_{\mathrm{Cu}^0} + D_{\mathrm{Cu}^+} K_{\mathrm{Cu}^+}(p/n_i)\right] \nabla \frac{C_{\mathrm{Cu}}}{\left[1 + K_{\mathrm{Cu}^+}(p/n_i)(1 + K_{\mathrm{CuB}} C_{\mathrm{B}^-})\right]} \right\} \tag{2.58}$$

Therefore, the effective diffusivity is calculated as

$$D_{\mathrm{Cu}}^{eff} = \frac{D_{\mathrm{Cu}^0} + D_{\mathrm{Cu}^+} K_{\mathrm{Cu}^+}(p/n_i)}{1 + K_{\mathrm{Cu}^+}(p/n_i)(1 + K_{\mathrm{CuB}} C_{\mathrm{B}^-})}. \tag{2.59}$$

Thus, the intrinsic diffusivity of copper ($p = n_i$, when C_{B^-} is small) is expressed as [78]

$$\begin{aligned} D_{\mathrm{Cu}}^{int} &= \frac{D_{\mathrm{Cu}^0} + D_{\mathrm{Cu}^+} K_{\mathrm{Cu}^+}}{1 + K_{\mathrm{Cu}^+}} \\ &= (3.0 \pm 0.3) \times 10^{-4} \times \exp\left(-\frac{0.18 \pm 0.01eV}{k_B T}\right) \qquad (\mathrm{cm}^2/\mathrm{s}) \end{aligned} \tag{2.60}$$

For copper, $D_{\mathrm{Cu}} \cong D_{\mathrm{Cu}^+}$, because $C_{\mathrm{Cu}} \cong C_{\mathrm{Cu}^+}$ [36, 77].

2.3.4 Fe

It is believed that the iron atom remains at the interstitial site with two possible charge states (Fe_i^0 and Fe_i^+). The expression for Fe diffusivity was reported by Weber [158]. Due to the difficulties of separating the diffusion behavior in both neutral and positive charged iron atoms, Istratov *et al.* [79] described the "effective diffusion coefficient of iron" including two charge states by fitting the experimental data from different groups with

$$D(\mathrm{Fe}_i) = 1.0^{+0.8}_{-0.4} \times 10^{-3} \exp\left(-\frac{0.67 \pm 0.02eV}{k_B T}\right) \mathrm{cm}^2/\mathrm{s}. \tag{2.61}$$

FeB pairing was first suggested by Collins and Carlson [21] in 1957, and the evidence of this was reported by Ludwig and Woodbury [103]. The reported binding energy (E_b) for FeB ranges from 0.58 [160] to 0.65eV [89]. The dissociation energy (E_{diss}) lies between 1.25 and 1.32eV, which is larger than E_{diss} for Cu (0.61eV). This indicates that FeB is more stable than CuB.

$$\mathrm{Fe}_i^+ + \mathrm{B}_s^- \longleftrightarrow \mathrm{FeB} \tag{2.62}$$

2.4 Summary

In this chapter, we have discussed both dopant and metal diffusion behavior in silicon with the incorporation of point defects. Properties of these point defects were reviewed in terms of their charged states and diffusivities. In the following chapters, we will describe the clustering models based on these fundamental models.

Chapter 3

PRECIPITATION MODELS

Numerous models have been previously developed to study the precipitation process. Many analyses only consider the total concentration of the precipitate, and are thus only useful for qualitative understanding. In reality, the behavior of precipitates is a strong function of size, which depends on the thermal history of the sample. In order to capture the complex behavior, the *full kinetic precipitation model* (FKPM) solves discrete rate equation for each precipitate size [31, 40] The *rediscretized full kinetic precipitation model* (RFKPM) [31, 40] reduces the computing time by rediscretizing the size distribution for larger sizes coarsely. To further improve the computing efficiency, the *reduced moment-based model* (RKPM) [19] calculates the time evolution of various moments. A delta-function approximation (DFA) is applied to simplify the analysis and give a more physical meaning to expressions in RKPM [135]. We will discuss these precipitation models in this chapter, and use them to describe the precipitation behavior of impurities and point defects in Chapters 4 and 5. This work follows the analysis from several previous efforts. Clejan *et al.* [19] introduced the reduced moment-based model of extended defects and applied it to dopant activation kinetics. Gencer *et al.* [43] used RKPM to describe the evolutions of {311} defects and dislocation loops. The RKPM with DFA is developed in conjunction with Chen-Luen Shih [135] to study the TED effect due to the presence of {311} defects and the gettering process for iron.

3.1 Full Kinetic Precipitation Model (FKPM)

3.1.1 The Driving Force of Precipitation

Precipitation is driven by the fact that above the solubility the formation of a separate phase reduces the total free energy of the system. The free energy change upon precipitate

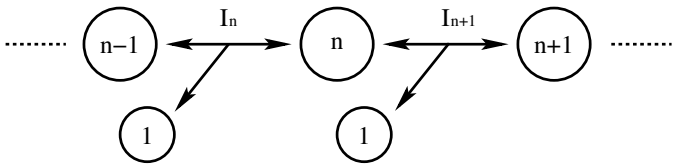

Figure 3.1: A schematic shows how precipitates grow or shrink by absorbing or emitting solute atoms [31].

formation can be written as

$$\triangle G_n = -nkT\ln\frac{C}{C_{ss}} + \triangle G_n^{exc} \tag{3.1}$$

where C and C_{ss} are the solute concentration and the effective solid solubility of the impurities associated with the formation of very large aggregates which can also be considered as the equilibrium concentration of impurities in the presence of an arbitrarily large solute-rich phase. ΔG_n^{exc} is the excess energy associated with a precipitate of finite size n, which depends on the geometry of a specific precipitate and includes interface and strain energies.

3.1.2 The Evolution of Size Distribution

The precipitation process proceeds by adding a solute atom to existing precipitates as shown in Fig. 3.1, generating a size $n+1$ precipitate from a size n precipitate. The precipitate size n can also dissolve by releasing a solute atom. The time evolution of precipitate density is described as

$$\begin{cases} \dfrac{df_1}{dt} = -2I_2 - \displaystyle\sum_{n=3} I_n \\ \dfrac{df_n}{dt} = I_n - I_{n+1} \qquad n \geq 2, \end{cases} \tag{3.2}$$

where f_n is the concentration of aggregates of size n, and I_n is the net flux from size $n-1$ to n. Note that in Eq. 3.2 an additional term must be calculated to keep track of solute atoms ($f_1 = C$), since they are involved in the growth of precipitates of all sizes. I_n can be written as

$$\begin{aligned} I_n &= g_{n-1}f_{n-1} - d_n f_n \\ &= D^{eff}\lambda_{n-1}(Cf_{n-1} - C_n^* f_n), \end{aligned} \tag{3.3}$$

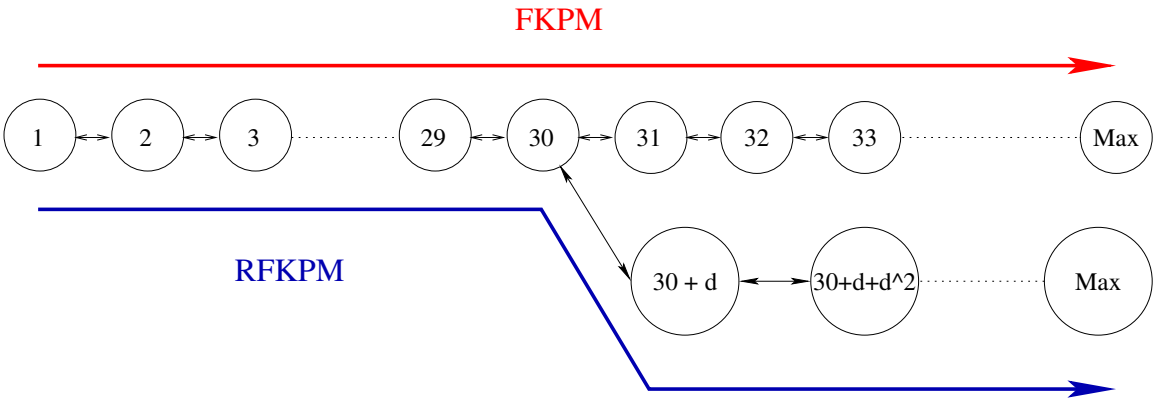

Figure 3.2: A schematic of rediscretization. Here we rediscretized the precipitates in size space after size 30, and d $>$ 1 is chosen to increase the interval between larger sizes.

where g_{n-1} and d_n are the growth and dissolution rate coefficients for precipitate size $n-1$ and n, D^{eff} is the diffusivity of impurities, λ_n is the kinetic growth factor, which can be determined from the reaction and diffusion rates at the interface of the precipitates. However, diffusion-limited growth is often assumed in modeling, as suggested by Ham *et al.* [58]. The detailed derivation of growth rate for different precipitate geometries (spherical, disc-shaped, and {311} defects) is included in Appendix B. C_n^* is the local equilibrium constant, which is defined such that there is no energy difference with the transition from size $n-1$ to size n ($\Delta G_{n-1} = \Delta G_n$ in Eq. 3.1). It can also be considered as the solute concentration that would be in equilibrium with a size n precipitate.

$$C_n^* = C_{ss} \exp\left(-\frac{\Delta G_n^{exc} - \Delta G_{n-1}^{exc}}{kT}\right) \tag{3.4}$$

3.2 Rediscretized Full Kinetic Precipitation Model (RFKPM)

FKPM produces accurate results but it requires a very heavy calculation. Many equations are needed to describe the system when the size of precipitates becomes very large. To reduce the number of equations and increase the time efficiency, the system can be assumed to be nearly continuous for large precipitate sizes and then the size distribution is rediscretized more coarsely with a linear function (as shown in Fig. 3.2). Thus, each point represents a range of sizes rather than just a single size. We replace n with $n[i]$, where $f_{n[i]}$ represents

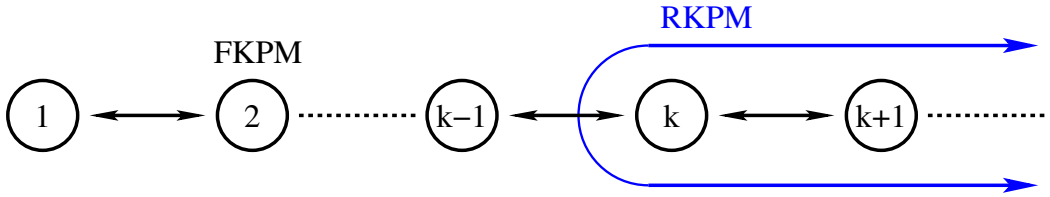

Figure 3.3: A schematic shows the concept of RKPM. The FKPM is used for small clusters, while RKPM describes the behavior of precipitation from size k.

the concentrations between sizes $(n[i-1]+n[i])/2$ and $(n[i]+n[i+1])/2$. The Fokker Planck equation (Eq. 3.5) [20, 27] describes the discrete system with a continuous equation as

$$\frac{\partial f}{\partial t} = \frac{\partial}{\partial x}[A(x)f(x,t)] + \frac{\partial^2}{\partial x^2}[B(x)f(x,t)], \tag{3.5}$$

where $A(x) = (g_n - d_n)$ and $B(x) = \frac{1}{2}(g_n + d_n)$. Eq. 3.5 is then rediscretized as

$$I_{n[i]} = \frac{1}{2}[\frac{(g_{n[i]} + d_{n[i]})f_{n[i]} - (g_{n[i+1]} + d_{n[i+1]})f_{n[i+1]}}{n[i+1] - n[i]} + (g_{n[i]} - d_{n[i]})f_{n[i]} + (g_{n[i+1]} - d_{n[i+1]})f_{n[i+1]}]. \tag{3.6}$$

Through this method, FKPM and RFKPM are applied to small and large sizes respectively. The discrete behavior for small size can be well captured, while the total number of rate equations and time for calculation are reduced. Note that Eq. 3.6 reduces to Eq. 3.3 if $n[i+1] = n[i] + 1$.

3.3 Reduced Moment-Based Kinetic Precipitation Model (RKPM)

Clejan *et al.* [19] introduced the reduced moment-based model (RKPM) to enhance the computational efficiency beyond that possible with RFKPM. This type of approach, which is commonly used for carrier and fluid transport, states that one can go from a Boltzmann equation to simpler hydrodynamic equations by computing moments and introducing a closure assumption [72]. Instead of calculating all the rate equations (Eq. 3.2) over a size space, the RKPM keeps track of the lowest moments of the distribution of larger precipitates. In Fig. 3.3, discrete equations are still applied on small clusters ($n < k$). These moments

are defined as

$$m_i = \sum_{n=k}^{\max} n^i f_n \qquad i = 0, 1, ... \tag{3.7}$$

Note k is the size where RKPM is started as shown in Fig. 3.3. The rate equations of these moments can then be written as

$$\begin{aligned} \frac{\partial m_i}{\partial t} &= k^i I_k + \sum_{n=k}^{\max} [(n+1)^i - n^i] I_{n+1} \\ &= k^i D^{eff} \lambda_{k-1} \left(C f_{k-1} - m_0 C_k^* \hat{f}_k \right) + D^{eff} m_0 (C\gamma_i^+ - C_{ss}\gamma_i^-), \end{aligned} \tag{3.8}$$

where

$$\begin{aligned} \gamma_i^+ &= \sum_{n=k}^{\max} [(n+1)^i - n^i] \lambda_n \hat{f}_n \\ \gamma_i^- &= \sum_{n=k}^{\max} [n^i - (n-1)^i] \lambda_n \hat{C^*_{n+1}} \hat{f_{n+1}}, \qquad i > 0 \end{aligned} \tag{3.9}$$

$\hat{f}_n$ is the normalized size distribution ($\hat{f}_n = f_n/m_0$, which is always smaller than 1), and $\hat{C}_n^* = C_n^*/C_{ss}$. The number of moments that need to be considered depends on the complexity of the system. In this work, the first two moments (m_0 and m_1) are considered, therefore, $\hat{f}_k$, γ_1^+, and γ_1^- have to be determined.

$$\begin{aligned} \gamma_1^+ &= \sum_{n=k}^{\max} \lambda_n \hat{f}_n \\ \gamma_1^- &= \sum_{n=k}^{\max} \lambda_n \hat{C^*_{n+1}} \hat{f_{n+1}}. \end{aligned} \tag{3.10}$$

The zero-*th* order moment of the distribution, m_0, is the concentration of all precipitates and the first order moment, m_1, represents the total concentration of atoms in those precipitates. Thus, $\hat{m}_1 = m_1/m_0$ is simply the average size of the precipitate. The γ terms can be generated from either the FKPM or the RFKPM, and described mathematically as function of average size $\hat{m}_1$ with Arrhenius dependence. The γ's can also be calculated analytically by assuming the distribution function $\hat{f}_n$ to be parameterized non-linear equations [43].

In RKPM, the system consists of only a few rate equations (Eq. 3.3) for small precipitates, which depend on k, and the time evolution of lowest moments (Eq. 3.7), described

by the γ's. This approach sacrifices the detailed size distribution of clusters, including only information about the solute concentration, the average size, and the total number of atoms within precipitates.

3.4 RKPM with the Delta-Function Approximation (DFA)

In the previous work [19, 31, 40], FKPM and RKPM have been used to describe the precipitation process. A significant problem with RKPM is the complexity of the expression for the γ's. Instead of using an analytical approach [43] by assuming the distribution function $\hat{f}_n$ to be given by a non-linear equation, a delta function approximation (DFA) for size distribution can be used to simplify the model implementation [135].

$$\hat{f}_n = \delta(\hat{m}_1 - n) \tag{3.11}$$

In DFA, the values of both summation terms (γ_1^+ and γ_1^-) are assumed to be equal to the values for a single defect with size equal to the average size in the system ($\hat{m}_1$). This not only simplifies the mathematical procedures for calculating γ_1^- and γ_1^+ in an analytical method but also equips them with more physical meaning. Therefore, if the first two moments are considered (m_0 and m_1), Eqs. 3.10 can be rewritten as

$$\gamma_1^+ = \lambda_{\hat{m}_1} \tag{3.12}$$

$$\gamma_1^- = \lambda_{\hat{m}_1} C^*_{\hat{m}_1+1} \tag{3.13}$$

γ_1^+ is simply the kinetic growth factor associated with average size of precipitates (m_1/m_0). γ_1^- is the product of the kinetic growth factor and local equilibrium constant, which are functions of the average size of precipitates (m_1/m_0) as well. γ_1^- is often an Arrhenius function due the temperature dependence of the equilibrium constant. Note that $\hat{f}_k$ can not be derived from the DFA method and has to be described mathematically as a function of average size, $\hat{m}_1$, and temperature.

3.5 Comparison of Precipitation Models for Vacancy Clustering

The FKPM for vacancy clustering was first introduced by Gencer *et al.* [40]. Demonstration of converting the rediscretized full kinetic precipitation model (RFKPM) to the

reduced moment-based kinetic precipitation model (RKPM) with delta-function approximation (DFA) for vacancy clustering is shown in this section. The reactions in the vacancy clustering model include the recombination between point-defects, the growth of vacancy clusters, and the dissolution of vacancy clusters by consuming an interstitial.

$$\mathrm{I} + \mathrm{V} \iff \emptyset \tag{3.14}$$

$$\mathrm{V}_{n-1} + \mathrm{V} \iff \mathrm{V}_n \tag{3.15}$$

$$\mathrm{V}_n + \mathrm{I} \iff \mathrm{V}_{n-1} \tag{3.16}$$

The flux rate equation can be written from Eq. 3.3 as

$$R_{\mathrm{IV}} = 4\pi a_0 (D_{\mathrm{I}} + D_{\mathrm{V}})(C_{\mathrm{I}} C_{\mathrm{V}} - C_{\mathrm{I}}^* C_{\mathrm{V}}^*), \tag{3.17}$$

$$R_n = D_{\mathrm{V}} \lambda_{n-1} (C_{\mathrm{V}} f_{n-1} - C_n^* f_n), \tag{3.18}$$

$$R_n^{\mathrm{IV}} = D_{\mathrm{I}} \lambda_n (C_{\mathrm{I}} f_n - C_n^{\mathrm{IV}*} f_{n-1}), \tag{3.19}$$

where D and C^* are the diffusivities and equilibrium constants for free interstitials and vacancies. a_0 and λ_n are the silicon lattice constant and the kinetic factor for a precipitate with size n, given as

$$\lambda_n = 4\pi a_0 n^{2/3}, \tag{3.20}$$

where a spherical geometry of voids (vacancy precipitates) is assumed. C_n^* is the equilibrium constant and defined as

$$C_n^* = C_{\mathrm{Si}} \exp\left(-\frac{E_B(n)}{kT}\right), \tag{3.21}$$

where C_{Si} is the atomic density for silicon, and $E_B(n)$ is the binding energies reported by Bongiorno *et al.* [10] and Jaraiz *et al.* [82] for adding an nth V to a $n-1$ size void. The first two moments of RKPM can be calculated via Eq. 3.7.

$$\begin{aligned} m_0 &= \sum_{n=36}^{\max} f_n \\ m_1 &= \sum_{n=36}^{\max} n f_n, \end{aligned} \tag{3.22}$$

where $k = 36$ in our vacancy clustering model. For $k < 35$, we use FKPM to describe the vacancy clustering with Eq. 3.2. The time evolution of m_0 and m_1 can be derived as

$$\frac{\partial m_0}{\partial t} = D_{\mathrm{V}}\lambda_{k-1}[C_{\mathrm{V}}f_{k-1} - m_0 C^*_{k-1}\hat{f}_k] - \lambda^{\mathrm{V}}_k D_{\mathrm{I}} m^{\mathrm{V}}_0 \left(C_{\mathrm{I}}\hat{f}_k\right) \quad (3.23)$$

$$\frac{\partial m_1}{\partial t} = kR_k + D_V m_0(\gamma^+_1 C_{\mathrm{V}} - C_{ss}\gamma^-_1) - kR^{\mathrm{IV}}_k - D_{\mathrm{I}} m^{\mathrm{V}}_0 \left(\lambda^{\mathrm{V}}_{\hat{m}^{\mathrm{V}}_1} C_{\mathrm{I}}\right). \quad (3.24)$$

Note that Eqs. 3.23 and 3.24 include both reactions in Eqs. 3.15 and 3.16.

γ^+_1, γ^-_1, and $\hat{f}_k$ were calculated via Eqs. 3.10 as points and shown in Figs. 3.4, 3.5, and 3.6. These points were generated under different conditions, such as initial vacancy concentration ($1\times10^{16}, 1\times10^{17}, 1\times10^{18}$, and $1\times10^{19}\mathrm{cm}^{-3}$), temperature (500, 700, 800, and 900°C), and time. DFA method was applied for γ^+_1 and γ^-_1 to fit these points. In Fig. 3.4, γ^+_1 is a function of kinetic factor, λ_n, and independent of temperature. The slope of the fitting curve is 2/3, which can be derived from the the kinetic factor in Eq. 3.20, ($\lambda_n \propto n^{2/3}$). In Fig. 3.5, note that γ^-_1 is an Arrhenius function due to the temperature dependence of $C^*_{\hat{m}_1+1}$ term in Eq. 3.13. The DFA method accurately described the γ's as shown in Fig. 3.4 and 3.5. An Arrhenius dependent function (Eq. 3.25) was fitted for $\hat{f}_k$ in Fig. 3.6, because the DFA method can not be used in this situation. In Fig. 3.6, results from RFKPM give an obvious deviation between average size 10^2 and 10^4 due to the different initial vacancy concentration. Although Eq. 3.25 can only fit well at larger size, we will show later that this does not substantially affect the overall behavior of the model.

$$\hat{f}_k(\hat{m}_1) = 10^{22}\hat{m}_1^{-8} + 4\times10^5\hat{m}_1^{-4} + 7\hat{m}_1^{-0.9}\exp\left(\frac{-0.75}{kT}\right) \quad (3.25)$$

Note that $\hat{f}_k \to 1$ when $\hat{m}_1 \to k$. The general form of $\hat{f}_k$ can be referred to Eq. 5.6.

An initial vacancy concentration of $1\times10^{17}\mathrm{cm}^{-3}$ was run at 900°C for the time as specified. While both models share the discrete behavior for vacancy clustering from size 2 to 35, the RKPM describes the clustering nature for larger size ($n \geq 35$) with moments (m_0 and m_1). Thus, the RKPM substantially reduces the number of precipitation rate equations (Eq. 3.3) and improves the computing efficiency. C_{V} first drops in Fig. 3.7[a] because of the formation of smaller vacancy clusters, which explains the increase of m_0 and m_1 in Fig. 3.7[b]. While C_{V} continues to decrease, m_0 starts to drop and m_1 remains nearly constant. This indicates the growth of larger vacancy clusters and the dissolution of smaller

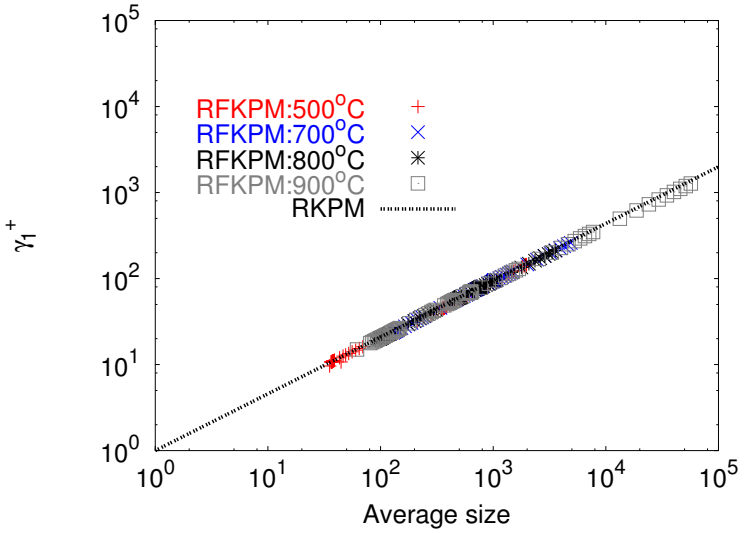

Figure 3.4: γ_1^+ vs. the average size for vacancy cluster. Points are generated from the RFKPM using Eqs. 3.9 under different conditions. Lines are the functions using DFA method (Eq. 3.12). The slope of the fitting curve is 2/3.

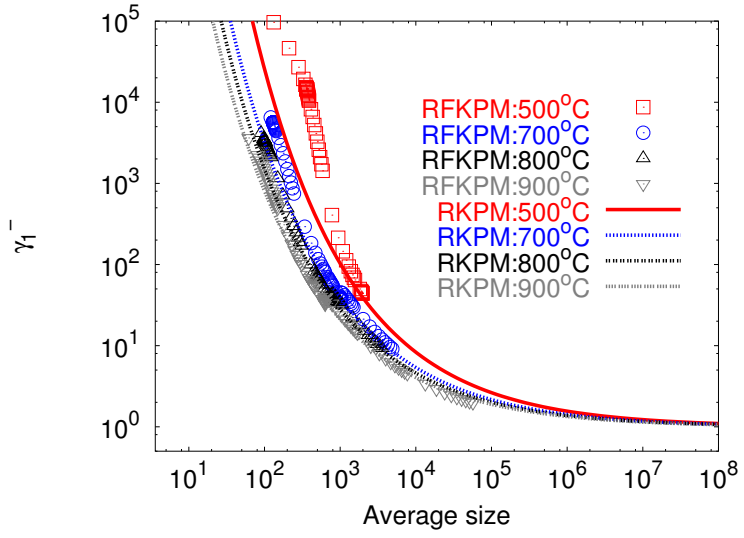

Figure 3.5: γ_1^- vs. the average size for vacancy cluster. Points are generated from the RFKPM using Eqs. 3.9 under different conditions. Lines are the functions using DFA method (Eq. 3.13). γ_1^- is an Arrhenius function because of the temperature dependence of C_n^*.

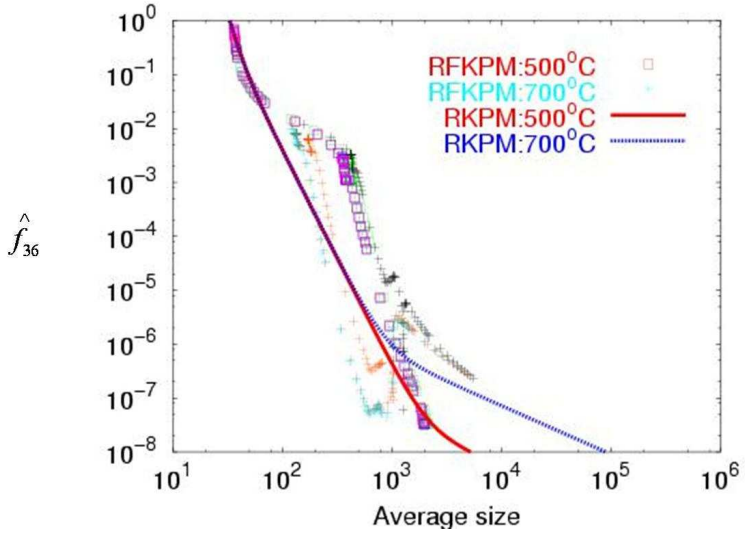

[a]

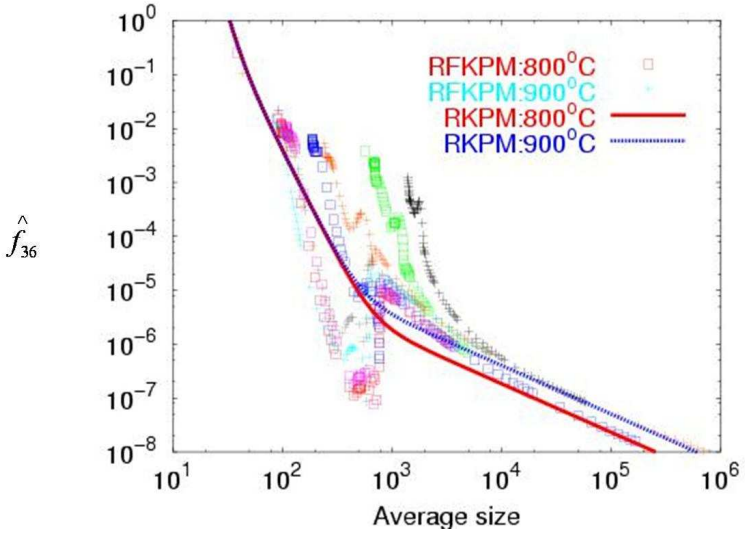

[b]

Figure 3.6: $\hat{f}_k$ ($k = 36$) vs. the average size for vacancy cluster at different temperatures: [a] 500 and 700°C; [b] 800 and 900°C. Points are generated from RFKPM using Eqs. 3.9 under different conditions. Lines are the fitting functions with an Arrhenius dependence for larger sizes (last term in Eq. 3.25).

clusters (Ostwald ripening). The simulation results from both RFKPM and RKPM-DFA are compared and shown in Fig. 3.7. As can be seen, RKPM-DFA accurately describes the time evolution of m_0, m_1 and free vacancy concentration (C_V).

3.6 Summary

We have first discussed the FKPM [31, 40] as used to capture the behavior of the precipitate size distribution, which depends on the thermal history of the sample, but it is computationally intensive. RFKPM takes advantage of a gradual change in behavior for large precipitate sizes to more coarsely rediscretize the size distribution. The RKPM [19] calculates the time evolution of the precipitation process more efficiently by only considering evolution of the lowest moments of the distribution. The RKPM with the delta-function approximation (DFA) [135] simplifies the mathematical procedures for calculating γ's and equips them with more physical meaning. Other than vacancy clustering, the example shown in Section 3.5, the RKPM-DFA can also be used for metal precipitation and interstitial clustering to study the gettering process, transient enhanced diffusion (TED), and boron activation more efficiently (see Sections 4.2, 5.1, and 5.2).

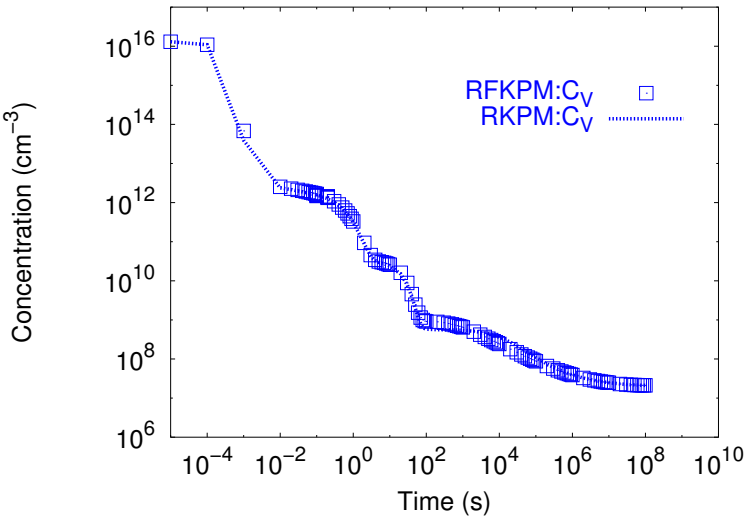

[a]

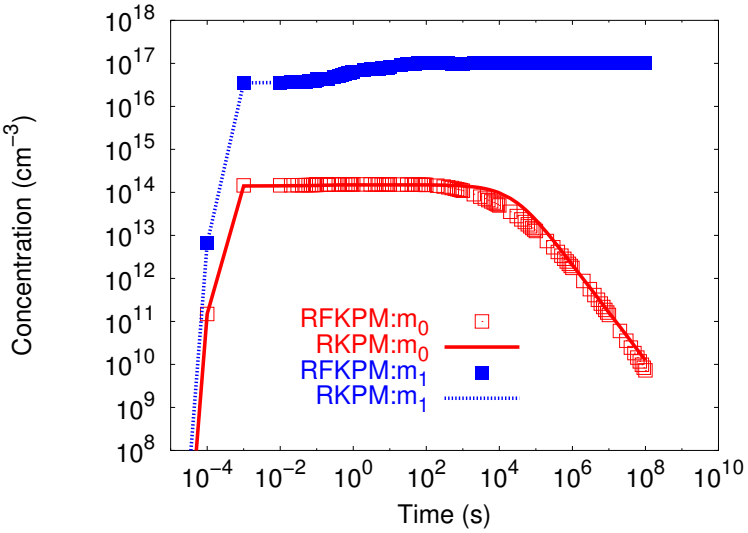

[b]

Figure 3.7: The comparison of time evolutions for vacancy concentration [a], m_0, and m_1 [b] between the rediscretized kinetic precipitation model (RFKPM) and the reduced moment-based precipitation model with the delta-function approximation (RKPM-DFA).

Chapter 4

GETTERING

It is challenging to remove unwanted contaminants such as metals (e.g., Cu, Fe, Ni, etc) to levels where they no longer affect device performance. Three levels of contamination control are used in current IC technology: clean factories, wafer cleaning, and gettering [126]. One can reduce the particles by working in clean rooms. Wafer cleaning requires the removal of particles, films, and any other contaminations on the wafer surface before each fabricational process step. Gettering is a technique that collects impurities to regions where they do minimal harm. The advantages of this technology are that devices often occupy the top layer of the wafer, and most of the contaminants concerned are highly mobile. To maintain high yield in the case of process variations and accidental contamination, gettering is necessary in today's device manufacturing.

In silicon, dissolved transition metals often are electrically active and exhibit deep energy levels, which act as donor or acceptor states. They may affect the doping concentration if the impurity concentration approaches the carrier concentration. However, a possible change in doping concentration is limited to very lightly doped silicon wafers, because unwanted impurity concentrations in processed silicon wafers rarely exceed 10^{13}cm^{-3}. A more serious issue is that metallic impurities introduce generation-recombination centers within the silicon band gap, which provide deep energy states. A severe deterioration in electrical properties can arise due to the generation/recombination of free carriers from dissolved impurities and their complexes. Impurity metals also have the tendency to precipitate at the silicon-silicon dioxide interface, which lowers gate-oxide breakdown voltages [65].

The indirect recombination is termed as Shockley-Read-Hall recombination (SRH) [138]. The net SRH recombination rate is written as:

$$U = \frac{pn - n_i^2}{\tau_p \left[n + n_i \exp \frac{E_t - E_i}{kT} \right] + \tau_n \left[p + n_i \exp \frac{E_i - E_t}{kT} \right]}, \tag{4.1}$$

where E_t and E_i are the deep energy trapping level and intrinsic Fermi level respectively, and τ is the minority-carrier recombination lifetime.

$$\begin{aligned} \tau_n &= \frac{1}{v_{thn}\sigma_n N_t} \\ \tau_p &= \frac{1}{v_{thp}\sigma_p N_t} \end{aligned} \tag{4.2}$$

v_{thn} and σ_n are the thermal velocity and capture cross-section of electrons. Subscripts n and p stand for electrons and holes respectively. N_t is the density of trapping sites. The capture cross-sections for different transition metals can differ by several orders of magnitude. Therefore, the tolerable impurity concentrations depend on the chemical nature of the respective impurities.

Impurity concentration also affects the generation leakage current [100]. The emission rates for electrons and holes are the inverse of carrier lifetimes (Eq. 4.2). Thus the leakage current is proportional to the impurity concentration and also depends on the capture cross-sections of transition metals. In fact, the system is more complicated because transition metals often exhibit more than a single deep energy level (trapping level).

There are three key steps in the gettering process [73]: (i) mobilization of metal atoms from localized and stable precipitate sites; (ii) diffusion of metal atoms to gettering sites; and (iii) capture of metal atoms at gettering sites away from the device region. These three steps are shown in Fig. 4.1. For effective gettering, the energy barrier for the release of impurity atoms from the original sites should be low, while the entrapped impurities should not be released easily. The impurity diffusion length should be longer than the distance between the impurity's original site and the gettering site.

Gettering mechanisms can be categorized into three groups: (1) relaxation gettering; (2) segregation gettering; and (3) phosphorus diffusion gettering [80]. In relaxation gettering, heterogeneous precipitation sites are formed intentionally in the region away from the device/surface region. An impurity supersaturation during a cool down from high temperature is required. Mobile and supersaturated impurity atoms diffuse and precipitate at the heterogeneous precipitation sites. Segregation gettering is driven by a gradient or a discontinuity of the impurity solubility. The region of higher solubility acts as a sink for impurities due to lower electrochemical potential. No supersaturation is required, therefore, lower im-

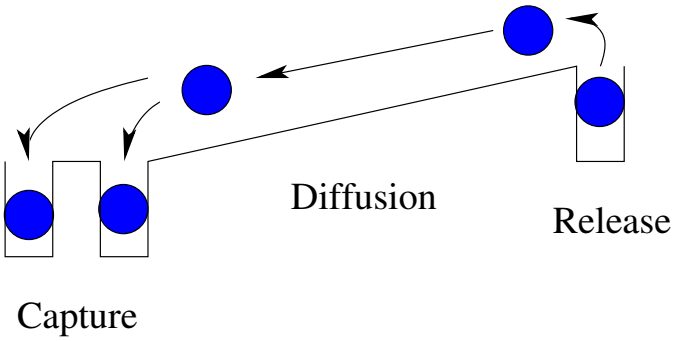

Figure 4.1: A simple schematic of 3 steps for gettering process [73].

purity concentration in the device region can be achieved. The segregation effect can result from differences in phases, materials, and doping levels. Strain also can have an impact on the local solubility of impurities [74, 112]. In phosphorus diffusion gettering, a heavily phosphorus doped layer provides several mechanisms for gettering: solubility enhancement by Fermi level effects, by an increase of the substitutional fraction of impurities, and by ion pairing; gettering to dislocations and SiP particles generated by phosphorus diffusion, and silicon interstitial injection-assist gettering [80].

The gettering techniques are classified into two groups, (see Fig. 4.2): *extrinsic gettering* (EG) and *intrinsic gettering* (IG) [85]. EG is generated by external means via mechanical damage [6, 114, 127], chemical [5, 69, 121], substrate doping (p/p^+ structure) [4, 9, 142], deposition of a metal thin film [113, 149] or a polysilicon layer [122], or ion implantation [9, 11, 90], which leads to the creation of defects or gettering sites for segregation or precipitate nucleation, *etc.* IG involves the localization of unwanted impurities at extended defects (e.g., silicon-dioxide precipitates.) formed in the bulk region of the wafer during thermal pretreatment [3, 46, 63, 70, 114].

In this chapter, we specifically investigate the gettering behavior for copper and iron. By utilizing the precipitation models from Chapter 3, simulation results are compared to the experimental data reported from different groups.

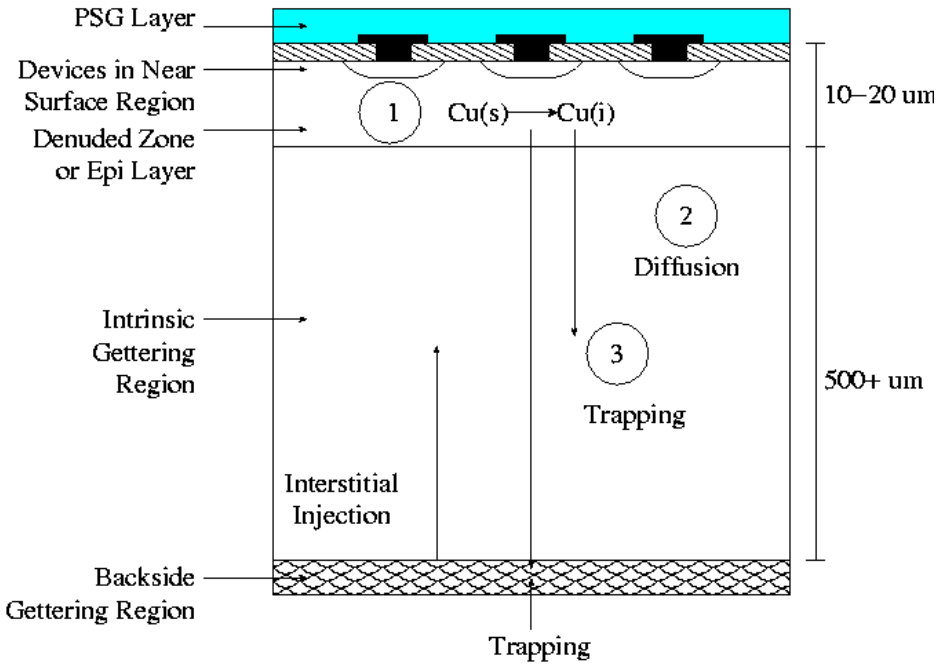

Figure 4.2: A schematic represents *intrinsic* and *extrinsic gettering* via the three-step gettering process: release, diffusion, and trapping [162].

4.1 Cu Gettering

Among 3d transition metals, Cu has the high solubility and diffusivity in silicon [158]. It can be easily introduced to the thermal process of silicon device fabrication, as Cu interconnect has become widespread. Several gettering techniques for Cu have been studied, such as intrinsic gettering, phosphorus-diffusion gettering, Si surface and Si/SiO_2 gettering, ion implantation gettering, chemical gettering, backside damage gettering and Al-backside gettering [64].

Previous work [55] is summarized in Section 4.1.1 and emphasized Cu diffusion and precipitation processes in the bulk silicon. In Section 4.1.2, we will focus on the mechanism of Cu out-diffusion, which has a strong dependence on the wafer surface condition. In Section 4.1.3, Cu precipitation at the wafer surface is studied by using FKPM from Chapter 3. Shabani *et al.* [132] and McCarthy *et al.* [104] reported that the wet wafer surface treatment has a significant impact on Cu out-diffusion and the surface precipitation. Ohkubo *et*

al. [120] suggested that Cu precipitates and organic molecules lower the surface potential and enhances the out-diffusion process. We proposed a possible explanation for this unusual behavior of Cu out-diffusion. In section 4.1.4, the simulation results are compared to the experimental data.

4.1.1 Cu Diffusion and Precipitation in Bulk Si (Previous Work)

We investigated copper precipitation models that provide the foundation for simulating copper diffusion and precipitation processes in silicon [55]. Three major mechanisms were considered for copper redistribution in silicon: pairing, diffusion, and precipitation. Positively charged copper (Cu^+) [57] pairs with acceptors (e.g., B^-) in bulk regions [155]. Copper diffuses interstitially with rapid redistribution at room temperature. Precipitation kinetics involves nucleation and growth. We captured this behavior by considering the evolution of precipitate size density (FKPM). Two important factors regarding the free energy in Eq. 3.1 must be considered: charge and strain. While positive-charged (Cu^+) copper is dominant, copper precipitates must be nearly neutral, due to Coulomb repulsion. A huge volume change is involved in copper precipitation process; $V_{Cu_3Si} \approx 2.3 V_{Si}$. The formation of three-dimensional (3D) precipitates must incorporate vacancies and/or eject interstitials. However, at at low temperature, self-diffusion is very slow. Thus, the formation of 3D precipitates is possible only near point defect sinks/sources. Since homogeneous nucleation cannot satisfy free volume at low temperatures, stress is minimized via formation of flat disc-shaped precipitates. The details of these models can be found in Guo *et al.* [55].

These models were verified by comparison to experimental measurements from Flink *et al.* [36, 77] in Figs. 4.3, and demonstrated the effectiveness for modeling copper behavior in silicon. In these experiments, Flink *et al.* [36, 77] evaluated Cu precipitation behavior under three boron concentrations ($C_B = 4 \times 10^{14}$, 4×10^{15}, and $2 \times 10^{16} cm^{-3}$) with various copper contamination levels. Concentrations of mobile copper and precipitated copper were measured with transient ion drift (TID) and X-ray fluorescence (XRF) in silicon after a high temperature in-diffusion and quench. Initially, copper was in-diffused at selected high temperatures for sufficient time for the solubility level to be achieved. Next, samples

were quenched in silicone oil at a rate of approximately 1000 K/s. The concentration of electrically-active copper was then measured with transient ion drift (TID) after 30 minutes at room temperature, and the bulk concentration of precipitated copper was measured with X-ray fluorescence (XRF). These measurements were performed after sufficient storage time at room temperature to let interstitial copper complete its preferred reaction path: either to diffuse out to the surface or to precipitate in the bulk [36, 77].

Fig. 4.3(a) shows the comparison between experimental data and simulation results for remaining interstitial copper concentration versus the initial copper concentration. The simulation results agree very well with experimental data, and predict the peak value for different C_{B}. For initial copper concentration less than the boron concentration, almost no precipitation occurs even though the concentration is well above room temperature solubility. The main reason for this phenomenon is dependence of solubility, and thus nucleation barrier on Fermi level. Also, due to that fact the Fermi level is pinned at the interface, it causes a built-in electric field, repelling Cu^{+} near the periphery of the precipitate more significantly in strongly p-type material ($C_{\mathrm{B}} = 2 \times 10^{16}\mathrm{cm}^{-3}$). For higher initial copper concentration, the copper precipitation process continues dropping the interstitial copper well below the boron concentration since critical nuclei already exist. Fig. 4.3(b) shows the comparison between experimental data and simulation results for precipitated copper concentration versus initial copper concentration. Again the model does an excellent job of capturing behavior. For high dopant concentration ($C_{\mathrm{B}} = 2 \times 10^{16}\mathrm{cm}^{-3}$), solute tends to out-diffuse instead of precipitating in the bulk, due to increased nucleation barrier in p-type material.

This previous work addressed the modeling of copper precipitation in silicon. The nucleation barrier depends strongly on the supersaturation and thus the solubility, which leads to strong Fermi level effects due to dominant positive charge state of interstitial copper. Once the nucleation barrier is overcome, precipitate will keep growing as long as the solute concentration is above the solubility. We have demonstrated that models can predict the behavior of the copper precipitation for low thermal budget process, where the precipitates are plate-like, by comparing the simulation results to experimental findings reported by Flink *et al.* [36, 77].

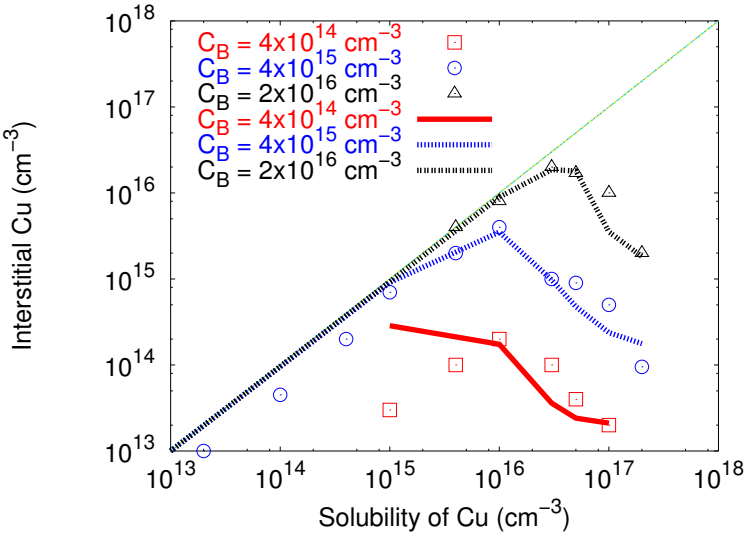

[a]

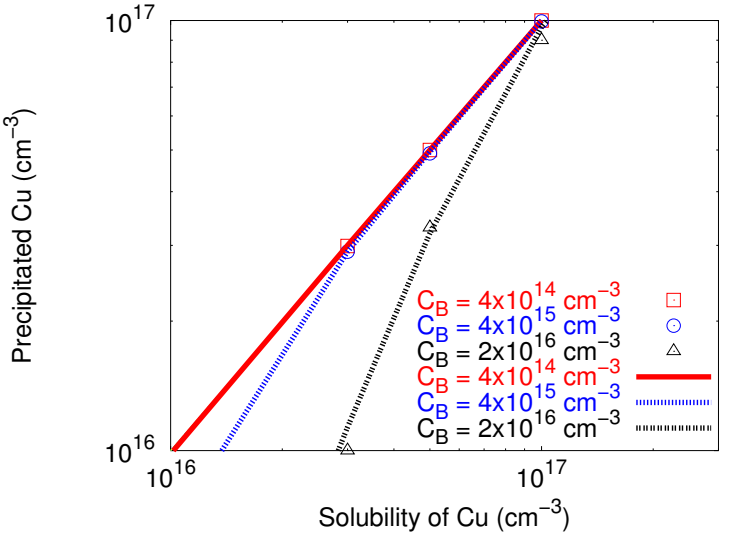

[b]

Figure 4.3: [a] Interstitial copper concentration as measured with TID 30 minutes after quench at room temperature vs. the solubility concentration of copper at in-diffusion temperature in three samples with different dopant concentrations. [b] Precipitated copper concentration measured with XRF vs. the solubility concentration of copper at in-diffusion temperature. Points are the experimental data and lines are simulation results.

4.1.2 Cu Out-Diffusion

As mentioned in Section 2.3.3, free copper diffuses interstitially and remains primarily in positive charge state (Cu^+). Also, Cu^+ is likely to pair with acceptors (B^-) in the bulk region, as described by Eq. 2.55.

The transport of Cu is driven by two mechanisms:

(1) the diffusion of Cu atoms due to the concentration gradient in silicon.

$$J_{diff} = -D_{\mathrm{Cu}}^{eff} \frac{\partial C_{\mathrm{Cu}}}{\partial x} \tag{4.3}$$

(2) the drift due to the presence of an electric field.

$$J_{drift} = q\mu_n C_{\mathrm{Cu}} \mathcal{E} = D_{\mathrm{Cu}}^{eff} C_{\mathrm{Cu}} \frac{\partial}{\partial x} \left[\ln \left(\frac{n}{n_i} \right) \right] \tag{4.4}$$

The electric field, $\mathcal{E}$, is derived from Poisson's equation and the mass action equation. The detailed derivation is located in Appendix. C. Combining Eqs. 4.3 and 4.4, the continuity equation for Cu can then be expressed as

$$\frac{\partial C_{\mathrm{Cu}}}{\partial t} = (J_{diff} + J_{drift}) = D_{\mathrm{Cu}}^{eff} \frac{\partial}{\partial x} \left\{ \frac{\partial C_{\mathrm{Cu}}}{\partial x} + C_{\mathrm{Cu}} \frac{\partial}{\partial x} \left[\ln \left(\frac{n}{n_i} \right) \right] \right\} \tag{4.5}$$

In a simple analysis, the boundary condition at the surface, Eq. 4.6, is assumed to be that the outward flux is proportional to the surface concentration of Cu with a surface reaction velocity (S). As discussed in Section 4.1.4, S has a strong dependence on the surface condition, and may vary when Cu atoms diffuse to the surface and precipitate.

$$-J(0,t) = -\left(J_{diff} + J_{drift}\right) = \mathrm{S} C_{\mathrm{Cu}}(0,t) \tag{4.6}$$

We also assumed that the Fermi level is pinned near mid-gap at the surface, which acts as a potential barrier for Cu^+ out-diffusion. In Fig. 4.4, the energy-band diagram shows the downward band bending due to the fact that the Fermi level is pinned near mid-gap at the surface in a p-type material. This resulting surface field lowers the Cu^+ concentration near the surface, which may effectively lower the surface reaction velocity (S).

To illustrate the importance of the drift mechanism and the energy-band bending, we compared the simulation results with and without the drift mechanism in Fig. 4.5. The resulting potential barrier builds an electrical field and prevents Cu^+ from out-diffusion to

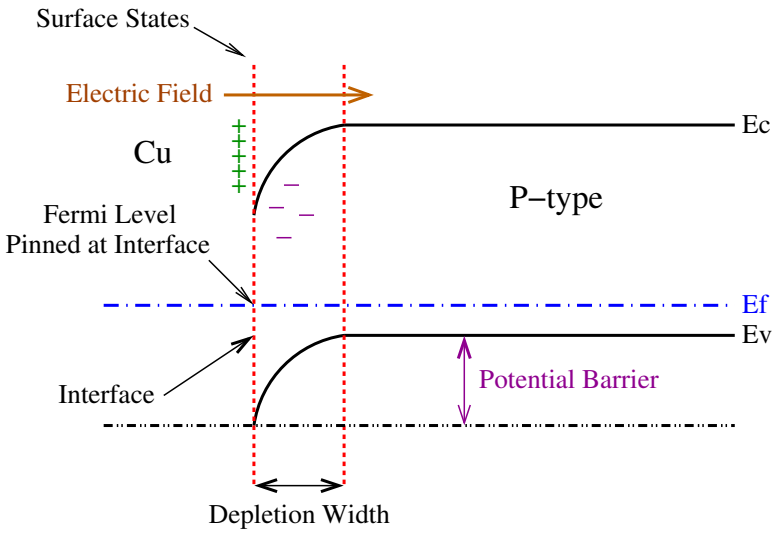

Figure 4.4: The energy-band diagram near the surface in a p-type material. Surface/interface states result in Fermi level pinning near the mid-gap. This causes the energy band to bend downwards and forms an electric field, which retards Cu^+ out-diffusion to the surface.

the surface. Therefore, Cu out-diffusion is much slower if the drift mechanism and Fermi level pinning are included.

4.1.3 Cu Precipitation at Wafer Surface

To accurately model precipitation kinetics, it is necessary to include the effect of charge exchange as the positively-charged Cu reacts to form neutral silicide. In the simplest precipitation model, which is only useful for qualitative understanding, the precipitation rate is proportional to the difference between free Cu concentration and Cu solubility. In contrast, the full kinetic precipitation model (FKPM) [31] (see Section 3.1) describes the evolution of the precipitate size distribution to account for thermal history effects. Precipitation is driven by the fact that above solubility formation of a solute-rich phase reduces the total energy of the system. The surface precipitation analysis in this work is similar to that used in our previous work on bulk Cu precipitation [55], with the difference that precipitates are assumed to be hemispherical rather than disc-shaped because the free volume is available at surface. Before surface precipitation can proceed, nuclei need to be formed. A free Cu

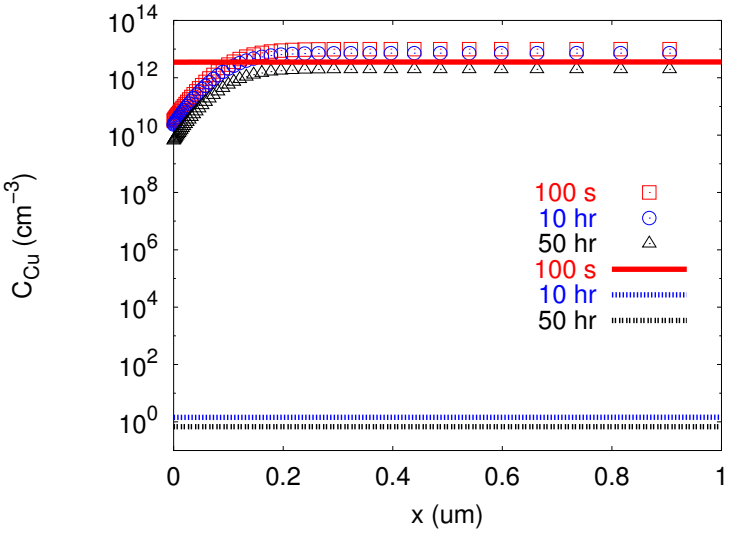

Figure 4.5: The comparison of Cu out-diffusion with and without the drift mechanism. Points are the depth profile of Cu concentration including both the diffusion and drift terms in Eq. 4.5, while lines only include the diffusion mechanism. The simulations are run at 60°C with the initial conditions of $C_{\mathrm{B}} = 1.5 \times 10^{16}$ and $C_{\mathrm{Cu}} = 1 \times 10^{13}\mathrm{cm}^{-3}$.

atom can segregate to an available surface site and act as a starting point for the surface precipitation. Cu precipitates at the surface of wafers then grow or shrink by absorbing or emitting Cu^{+} atoms. Fig. 4.6 illustrates the schematic of the surface segregation and precipitation. The evolution of precipitate density can be described as

$$\begin{cases} \dfrac{\partial C_{\mathrm{Cu}}}{\partial t} = -I_{seg} - \displaystyle\sum_{m=2} I_m \\ \dfrac{\partial f_m}{\partial t} = I_m - I_{m+1} \qquad\qquad m \geq 2 \end{cases} \tag{4.7}$$

where f_m is the precipitate density of size m, and I_{seg} accounts for the segregation of free Cu to an empty surface site. I_m is the flux from size $m-1$ to m in precipitate size space. I_m is given by the difference between the growth and dissolution rates:

$$I_m = D_{\mathrm{Cu}} \lambda_{m-1} \left\{ C_{\mathrm{Cu}} f_{m-1} - f_m C_m^* \right\}, \qquad m \geq 2 \tag{4.8}$$

where λ_m is the kinetic growth factor for precipitate size m, which can be determined from the interface reaction rate and geometry of the precipitates [30]. C_m^* is the local equilibrium constant (similar to Eq. 3.4), which is defined such that there is no energy difference with

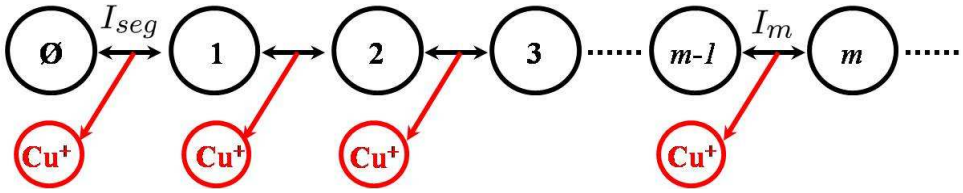

Figure 4.6: A schematic shows how Cu precipitates grow or shrink at the wafer surface by absorbing or emitting free Cu atoms. To form a nucleus, a free Cu atom is segregated to an empty site $\emptyset$.

the transition from size $m-1$ to m, and this constant can be expressed as

$$\begin{aligned} C_m^* &= C_{ss} \exp\left(-\frac{\Delta G_m^{exc} - \Delta G_{m-1}^{exc}}{kT}\right) \\ &= C_{ss}^i \left(\frac{n}{n_i}\right)^{-1} \exp\left[\frac{Am^{2/3} - A(m-1)^{2/3}}{kT}\right], \end{aligned} \tag{4.9}$$

where C_{ss}^i is the solubility of copper in intrinsic silicon, and A is proportional to the surface/strain energy per unit area. Note that the local equilibrium constant, C_m^*, is a function of the electron density, which depends on the position of Fermi level. The factor $(n/n_i)^{-1}$ accounts for electron incorporation required for positively charge copper (Cu^+) to form neutral precipitates. Assuming the total volume of the hemispherical-shaped precipitates is equal to the product of the number m of Cu atoms and its unit volume ($m\Omega = \frac{2}{3}\pi R_m^3$), we get

$$R_m = \left(\frac{3m\Omega}{2\pi}\right)^{1/3}, \tag{4.10}$$

where Ω is the volume density. ΔG_m^{exc} is a function of the surface area of size m precipitate ($2\pi R_m^2$), which is proportional to $m^{2/3}$.

4.1.4 Comparison to Experimental Data

In Ohkubo *et al.*'s experiment [120], the samples were boron-doped (10 Ωcm), single side polished, and 200mm Czochralski silicon wafers. These Si wafers were immersed in deionized water containing Cu, followed by 900°C annealing for one hour to drive Cu contamination

into the wafers. Fig. 4.7 [top] shows the experimental procedure for the annealing conditions and measurements. Out-diffused Cu ($C_{1\text{st}}$) was measured by total reflection X-ray fluorescence (TXRF) after the first bake, in either a quartz box or a plastic box, at 60°C for varying time up to 48 hours. Then surface cleaning was performed with a solution to remove the surface Cu precipitates. TXRF measurements ($C_{2\text{nd}}$) were repeated again after second bake at 80°C for 24 hours in a plastic box to out-diffuse the rest of the Cu. A surface precipitation ratio (C_s/C_0) (see Fig. 4.7 [bottom]) was defined as the ratio of surface precipitated Cu after the first step ($C_{1\text{st}}$) to the initial total Cu concentration in silicon bulk ($C_0 \approx C_{1\text{st}} + C_{2\text{nd}}$). Fig. 4.7 [bottom] also shows the enhancement of Cu out-diffusion caused by organics. In this experiment, organic molecules were released from plastic box and absorbed by the contaminated wafers. In Fig. 4.8, electrostatic potential measurements were performed by the Kelvin probe method for different surface Cu concentrations (ΔV up to 100 mV) and different levels of organic contamination on the Si surface (ΔV up to 50 mV) [120].

In Fig. 4.7 [bottom], simulation results with a simple approximation using fixed surface velocities S (Eq. 4.6) are shown with lines. Note that these surface velocities are several orders smaller than the diffusion-limited rate D/a (∼5 cm/s). This suggests that the effect of Fermi level pinning at the surface may need to be included. In Section 4.1.2, Fig. 4.4 illustrates that the Fermi level at the surface is pinned near the mid-gap in a p-type wafer because of the presence of surface states. The electrical field generated by energy band-bending slows the Cu out-diffusion process. In Fig. 4.9, surface velocities required to match experiments are substantially increased because the Fermi level pinning at the surface is included. Moreover, measurements from Ohkubo *et al.* [120] indicate that both existing Cu precipitates and organics on the surface shift the surface Fermi level, which lower the diffusion barrier and enhance Cu out-diffusion. This phenomenon is described as

$$E_F^{surf} = E_F^{\text{Cu}_3\text{Si}} + q\Delta V, \tag{4.11}$$

where $E_F^{\text{Cu}_3\text{Si}}$ is the surface Fermi level for high surface coverage of Cu silicide, and the electrostatic potential shift (ΔV) depends on the amount of Cu precipitates and organics absorbed from the plastic box. In Fig. 4.10, we show fitting functions used to describe the

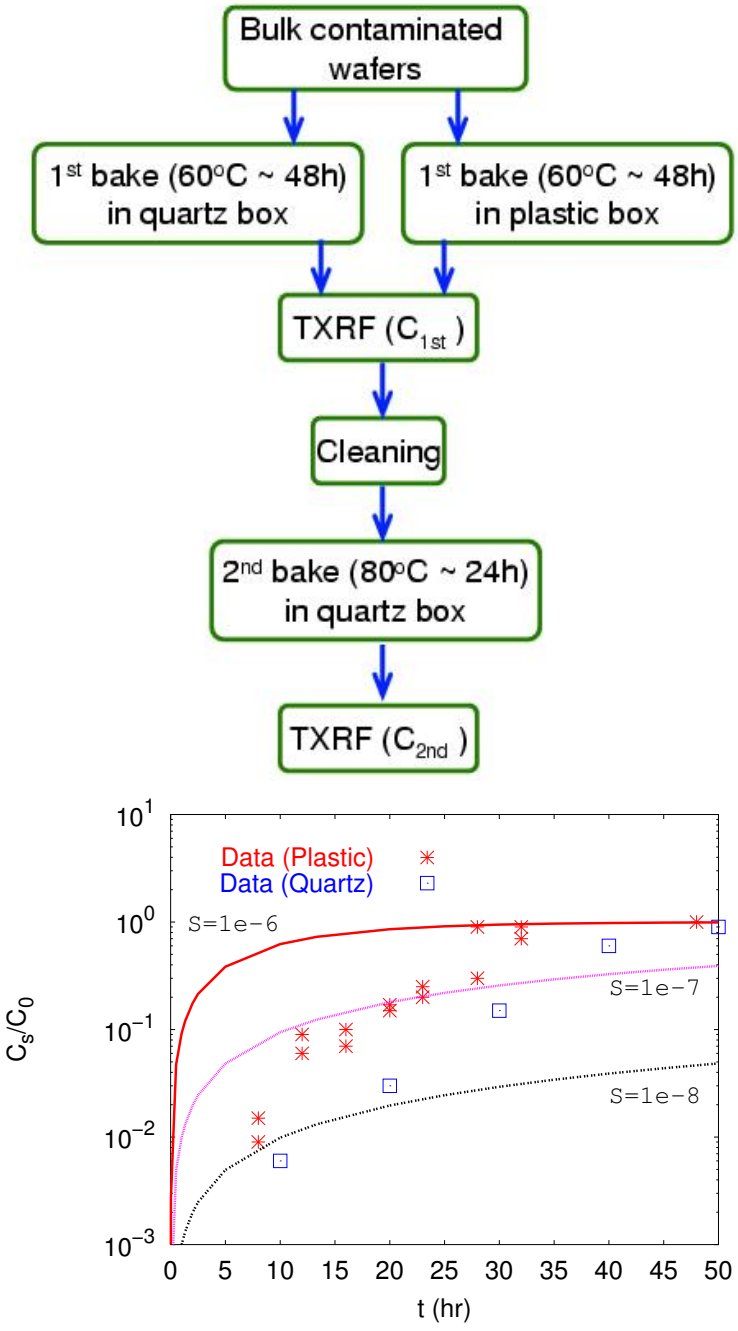

Figure 4.7: [top] Experimental flow from Ohkubo *et al.* [120]; [bottom] resulting surface precipitation ratio vs. the baking time at 60°C [120]. Points are the experimental data and lines are the simulation results with a simple approximation using various fixed surface velocities S (cm/s). Note poor match of this simple model to the data. Cu atoms out-diffuse to surface of the Si wafer and start to precipitate as a function of the baking time. Out-diffusion of Cu is substantially faster when the first bake is done with samples in a plastic box, which results in organic contamination on surface.

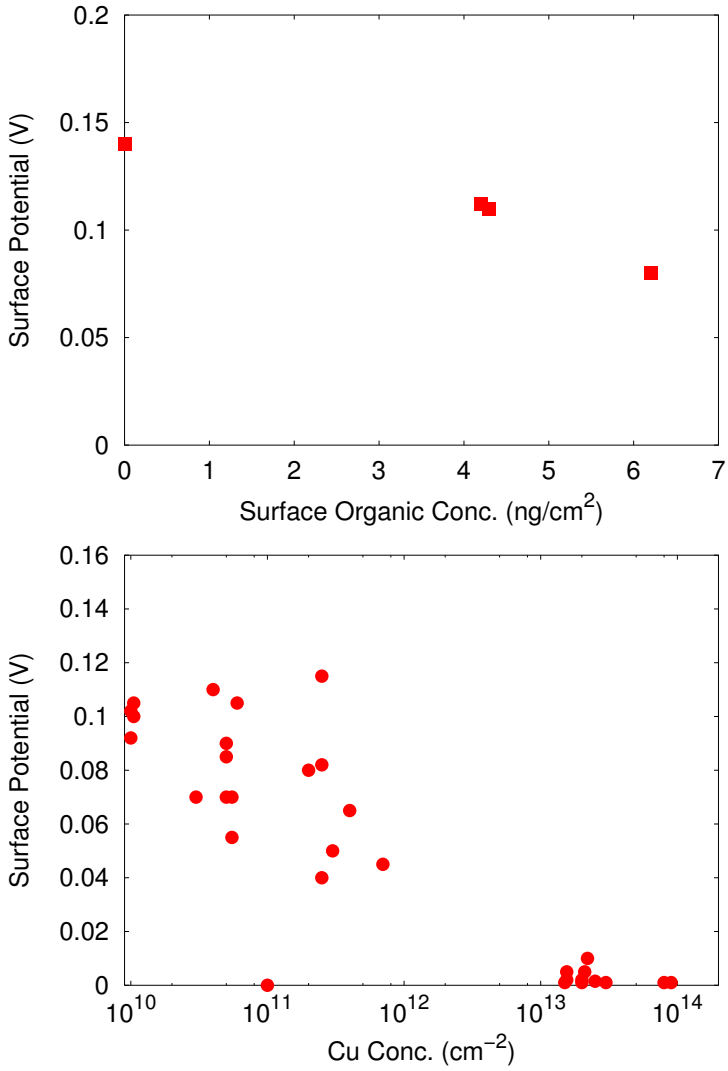

Figure 4.8: Surface electrostatic potential measurements from Ohkubo *et al.* [120]. [top] Surface potential vs. surface organic concentration for clean wafers baked in a plastic box at 60°C for 0-24 hours. Surface potential drops approximately 50mV because of the absorption of organics on surface. [bottom] Surface potential vs. surface Cu concentration after wafers were stored at room temperature in a plastic box for one month. The presence of precipitated Cu at the surface lowers the surface potential by up to 100mV.

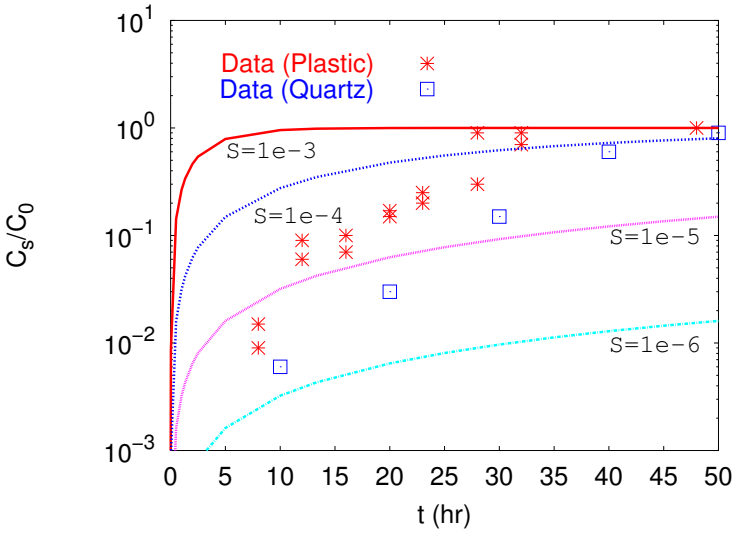

Figure 4.9: A comparison of experimental data (points) from Ohkubo *et al.* [120] and simulation results. In these simulations, both diffusion and drift mechanisms are included. Note the increase of surface velocity (S) compared to Fig. 4.7 [bottom] when Fermi level pinning is included.

experimental measurements of ΔV, which depend on the concentrations of Cu precipitates and absorbed organics. Because of the Fermi level dependence on the local equilibrium constant (C_m^*) in Eq. 4.9, the position of Fermi level strongly affects the surface precipitation behavior.

Ohkubo *et al.* [120] assumed a simple precipitation model at the surface, but this model required non-constant surface reaction velocity, which was chosen as an empirical function of baking time.

$$\mathrm{S} = \exp(\alpha + \beta t), \tag{4.12}$$

where α and β are the fitting parameters. This approximation suggested that the surface reaction velocity was a function of time, rather than the surface condition. It is only useful for qualitative understanding, because important factors, such as the pinned Fermi level and electrostatic potential changes, were not taken into account.

In this work, the evolution of precipitate size distribution at the surface (FKPM) was applied to describe the surface precipitation process, such that precipitation behavior de-

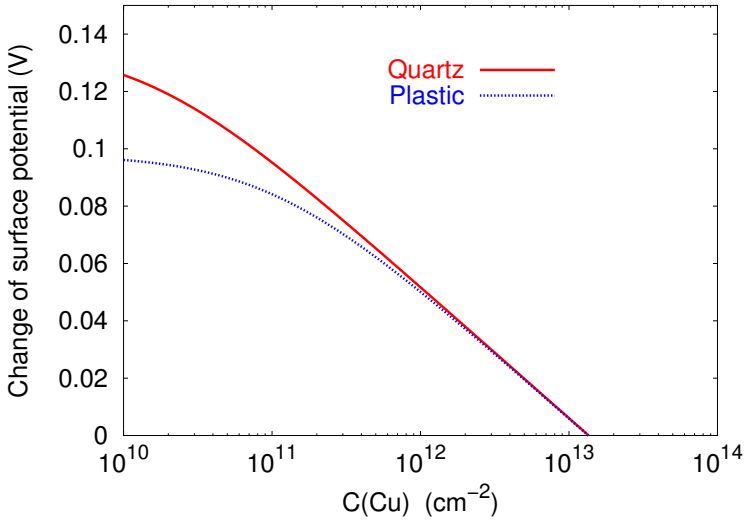

Figure 4.10: Surface potential change vs. surface Cu concentration: fitting functions were applied to describe the change of surface potential because of the presence of existing Cu precipitates and organics from the plastic box. These plots can be compared to the data shown in Fig. 4.8.

pends on the thermal history of the sample and is a strong function of the precipitate size and shape. The position of the surface Fermi level was determined by the surface conditions, including the amount of precipitated Cu and organics. Cu diffusion and CuB pairing were included with a Fermi level dependence. An excellent agreement in the comparison between the experimental data and simulation results are shown in Fig. 4.11. During the first bake in either quartz or plastic boxes, Cu out-diffuses to the surface nonlinearly because Cu precipitation at the surface lowers the pinned Fermi level and enhances the Cu out-diffusion process. Additionally, in the case in which the organics were absorbed at the surface, Cu out-diffusion was enhanced because of the fact that organics shift the surface Fermi level and thus lower the energy barrier for Cu out-diffusion.

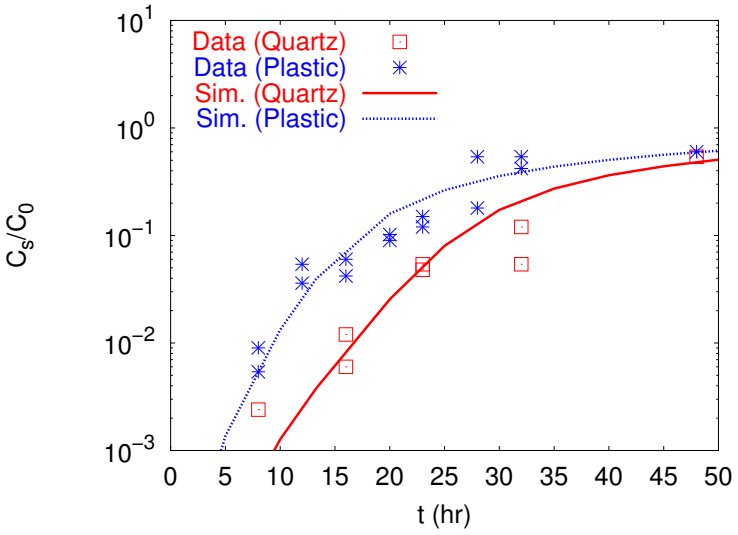

Figure 4.11: A comparison of experimental data (points) from Ohkubo *et al.* [120] and simulation results (lines). Compared to Figs. 4.7 and 4.9 in which no single S value captures experimental behavior.

4.2 Fe Gettering

Kaiser *et al.* [70] and Mets *et al.* [114] were the first to establish that silicon-oxide precipitates are sinks for metal impurities. Gilles *et al.* [46], Hieslmair *et al.* [63], and Aoki *et al.* [3] confirmed that silicon-oxide precipitates are sinks for iron gettering and proved that internal gettering is a relaxation-type gettering. The use of p/p^+ wafers provides another method for gettering iron out of the epitaxial layer and into substrate, where the enhanced solubility of iron in the heavily doped substrate is the driving force [4, 142].

Techniques that form gettering sites very close to the device region are known as proximity gettering techniques. One of the proximity gettering techniques is by ion implantation, started by the work of Buck *et al.* [11]. Iron gettering via implantation of MeV B [9] or Si [90] ions has been shown to reduce Fe concentrations to below 10^{10}cm^{-3}. Ion implantation creates two damage regions: an interstitial-rich region near ion projection range, R_p, and a near surface ($R_p/2$) vacancy-rich region. Kononchuk *et al.* [91] suggested that R_p defects provided gettering sites for relaxation of supersaturated Fe during cooling and

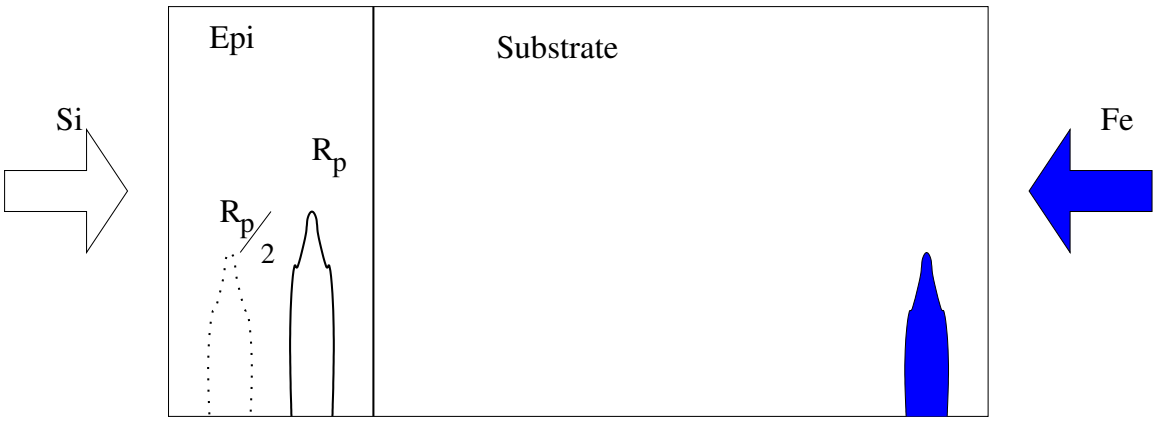

Figure 4.12: A schematic of experimental procedure. Implantation of 100keV Fe ions was performed after 2.3MeV Si ion implantation. R_p and $R_p/2$ are the projected range for interstitials and vacancies [92].

is limited by diffusion of point defects from the bulk. Other 3d metals, such as Cu, can also be captured by MeV implantation defects [86, 90]. To isolate the *intrinsic gettering* via oxygen, Koveshnikov *et al.* [92] introduced MeV Si defects into both Czochralski (Cz) substrates and epitaxial silicon doped with boron. Boron doped epitaxial Si wafers with 4.5 μm thick epilayer and 20 Ωcm for both epilayer and substrate were used. Implantation of 2.3MeV Si ions was performed into the epilayer with the dose of 5×10^{14} or 1×10^{15}cm^{-2}. The wafers were subsequently implanted with 100keV Fe ions with a dose of 1×10^{13}cm^{-2} from the back side, as shown in Fig. 4.12. The samples were annealed in the furnace for 1 h at 900°C to allow interstitials coalesce into dislocation loops and to diffuse Fe through the wafer. After samples were slowly cooled down, iron distribution shown in Fig. 4.15 was measured by secondary ion mass spectrometry (SIMS) and deep level transient spectroscopy (DLTS).

In this section, we will focus on Fe gettering via implantation of MeV Si ions into epitaxial silicon. Precipitation models introduced in Chapter 3 are used to describe growth of the MeV Si implant defects in both damage regions. The mechanism of Fe decoration on interstitial and vacancy clusters is first introduced, following by a comparison between the experimental data and simulation results.

4.2.1 Mechanism for Fe Gettering via Ion Implantation

We have mentioned earlier that gettering requires 3 steps: (1) release of metal atoms; (2) diffusion to gettering sites; (3) capture of metal atoms, as shown in Fig. 4.1 [92]. Annealing enables Fe atoms to mobilize from the wafer backside and redistribute through the substrate and the silicon epilayer. Fe atoms were captured at the voids and dislocation loops in the silicon epilayer during the slow cooling. The formation of vacancy clusters is described by the reduced moment-based precipitation model (RKPM) with the delta-function approximation (DFA) discussed in Chapter 3.

Analytical kinetic precipitation model (AKPM) from Gencer [40] was adopted for the formation of dislocation loops. Gencer assumed that the formation of I clusters in smaller sizes is energetically favorable over {311} defects, while dislocation loops are more stable above a critical size ($n_{\text{crit}} = 1500$ in this model). The transfer rate from {311} defects to dislocation loops can therefore be expressed as

$$\frac{D_{\text{I}}}{b^2}\left[f_n^{311} - f_n^{loop}\exp\left(-\frac{\Delta G_n^{311} - \Delta G_n^{loop}}{kT}\right)\right], \tag{4.13}$$

where b and D_{I} are the capture distance and diffusivity for the interstitial. f_n and ΔG_n are the concentration and free energy at size n, where the superscripts (311 and *loop*) stand for different species. The reduced moment-based model (RKPM) were then used to describe the time evolution of moments.

Fig. 4.14 demonstrates the segregation process of Fe atoms to vacancy clusters or dislocation loops. An Fe atom lands on an empty site at the surface of a void or dislocation loop and is stabilized due to the relaxation. The forward reaction is proportional to the product of concentrations of iron and empty sites on the defect's surface, while the reverse reaction is proportional to the concentration of sites that are occupied. Therefore, the decoration rate for voids can be written as

$$Rate_{decor}^{void}(n) = k_{inf}^{void}(n)\left\{C_{\text{Fe}} * \left[C_{site}^{void}(n) - C_{full}^{void}(n)\right] - \frac{C_{full}^{void}(n)}{K_{eq}^{void}}\right\}, \tag{4.14}$$

where K_{eq}^{void} is an equilibrium constant with an Arrhenius dependence.

$$K_{eq}^{void} = \frac{1}{C_{\text{Si}}}\exp\left(\frac{-E_B^{void}}{kT}\right) \tag{4.15}$$

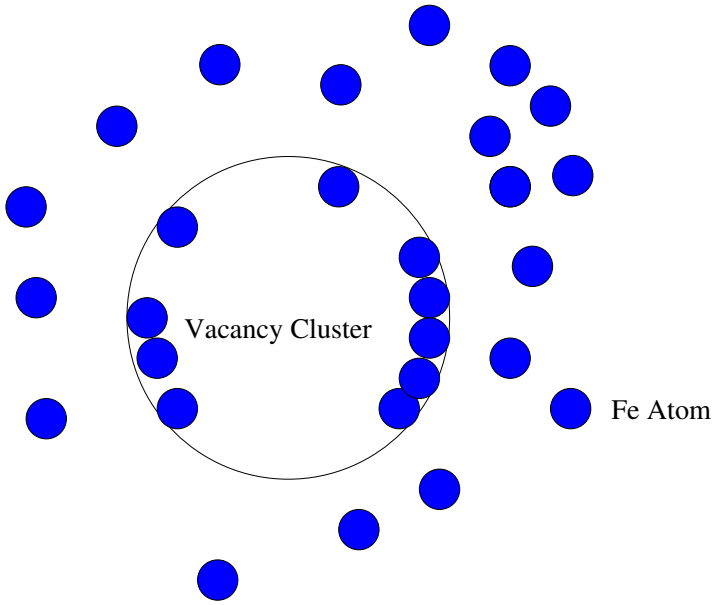

Figure 4.13: A schematic of Fe atoms captured by a vacancy cluster.

$$k_{inf}^{void}(n) = 4\pi r_{void}(n) D_{\mathrm{Fe}}^{eff}, \tag{4.16}$$

$$r_{void}(n) = \left(\frac{3n}{4\pi C_{\mathrm{Si}}}\right)^{1/3}, \tag{4.17}$$

$k_{inf}^{void}(n)$ is the kinetic factor which depends on Fe diffusivity [158] and void's size. n and r_{void} are the size and radius of a cluster. In Eq. 4.14, C_{full} is the density of the site occupied by a Fe atom. $C_{site}(n)$ is the concentration of sites available for Fe atoms to sit on and can be expressed as

$$\begin{aligned} C_{site}^{void}(n) &= f_n^{void} * N_{site} * A_{void}(n) \\ &= f_n^{void} * N_{site} * \left[4\pi r_{void}^2(n)\right], \end{aligned} \tag{4.18}$$

where N_{site} is the site density per area ($\approx 7 \times 10^{14}\mathrm{cm}^{-2}$), and f_n^{void} is the concentration of the void with size n.

For the Fe decoration of dislocation loops, a similar analysis is used. However, a different kinetic factor $k_{inf}^{loop}(n)$ (Eq.4.15) and $C_{site}^{loop}(n)$ (Eq. 4.18) need to be used due to the fact that vacancy clusters and dislocation loops have difference geometries. Also, the equilibrium constant (K_{eq}) in Eq. 4.15 should have a different Arrhenius dependence (E_B^{loop}).

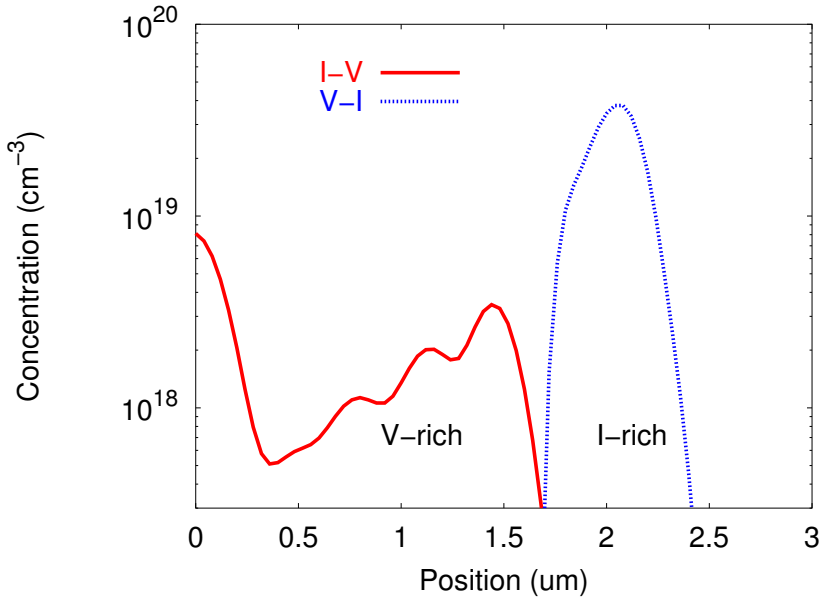

Figure 4.14: A SRIM simulation [169] of net I and V profiles resulting from implantation of 2.3MeV silicon ions with the dose of $1 \times 10^{15}\text{cm}^{-2}$ into a silicon epilayer. The projected ranges for net excess I and V are $R_p/2 \approx 1\mu$m and $R_p \approx 2\mu$m.

4.2.2 Comparison to Experimental Data

Fig. 4.14 shows the initial profiles for point defects generated by SRIM [169] with 2.3MeV Si ion implantation at the dose of 10^{15}cm^{-2}. $R_p/2 \approx 1\mu$m and $R_p \approx 2\mu$m are the projected ranges for net excess vacancy and interstitial respectively. Interstitial- and vacancy-rich regions form dislocation loops and vacancy clusters to provide the gettering sites for the relaxation of supersaturated Fe. Fig. 4.15 shows a good agreement between the experimental data and simulation results. The capture of Fe atoms near $R_p/2$ is due to the presence of vacancy clusters, which provide the open volume for Fe precipitation. A reduction of the gettering capacity in the $R_p/2$ region due to the different doses of Si ion implantation (5×10^{14} and $1 \times 10^{15}\text{cm}^{-2}$) can be seen from Fig. 4.15. Fig. 4.16 shows the locations of dislocation loops and vacancy clusters. After 900°C annealing for 1h, the concentration of vacancy clusters is much higher with a higher dose of Si ion implantation. The concentration of vacancy clusters reduces because of the interstitial flux from dislocation loops, and the

vacancy flux toward the wafer surface. As a result, vacancy clusters disappear earlier in the case of lower Si^+ ion implantation dose, while the concentrations of dislocation loops remain constant due to the energetic stability.

4.3 Summary

We have individually discussed the gettering models for both copper and iron. Rediscretized fully kinetic precipitation model (RFKPM) was used to account for copper precipitation in the bulk silicon. The Cu out-diffusion process shows a strong dependence of the surface condition, where the surface states and Fermi level vary with the presence of copper precipitates and organic molecules at the surface. Based on the measurement of electrostatic potentials under different Cu precipitate and organic molecule concentrations, we were able to explain and characterize the unusual Cu out-diffusion behavior reported by Ohkubo *et al.* [120].

Iron gettering via ion implantation has been shown to be highly effective. This technique can introduce gettering sites just a few μm away from the device region, allows a low thermal-budget process, and can also be used for SOI wafers. We have used reduced moment-based kinetic precipitation models (RKPM) for both interstitials and vacancies to study the evolution of gettering sites, vacancy clusters and dislocation loops. The capture of iron atoms by gettering was described and characterized by the experimental data from Koveshnikov *et al.* [92].

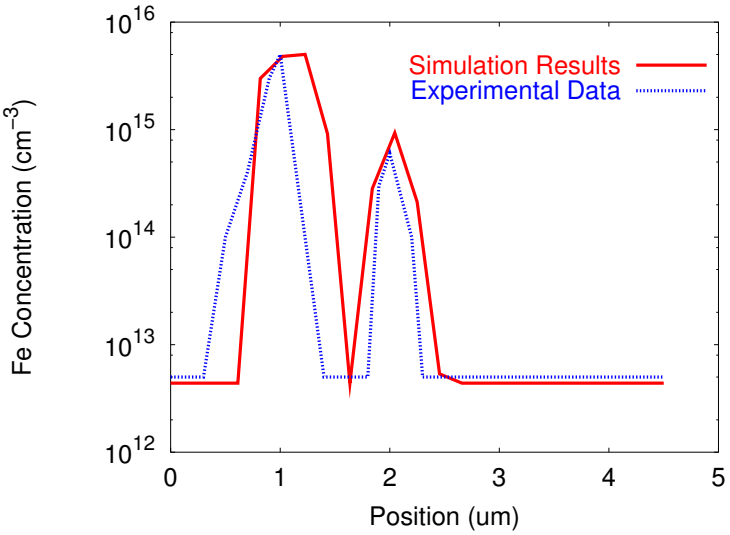

[a]

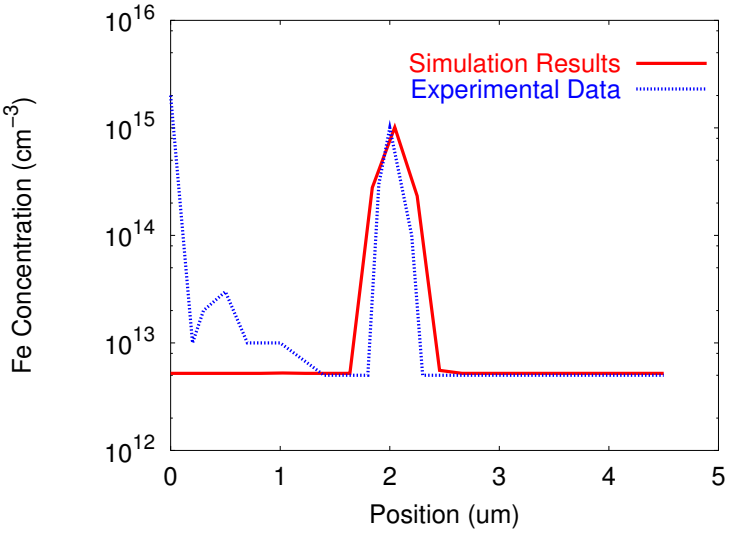

[b]

Figure 4.15: Comparisons of simulation results and experimental data. Iron in epi-Si was measured by SIMS after annealing at 900°C for 1 h followed by slow cooling [92]. Before annealing, 2.3MeV Si ion implantation was done to a dose of 10^{15} [a] and 5×10^{14}cm^{-2} [b].

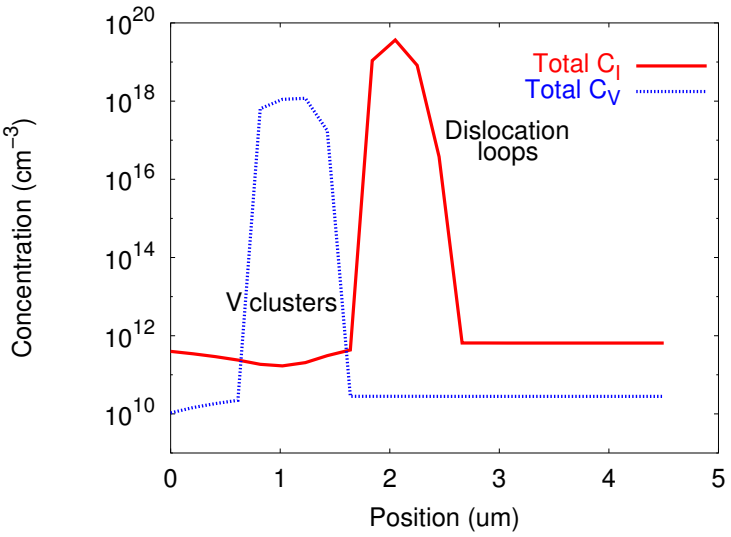

[a]

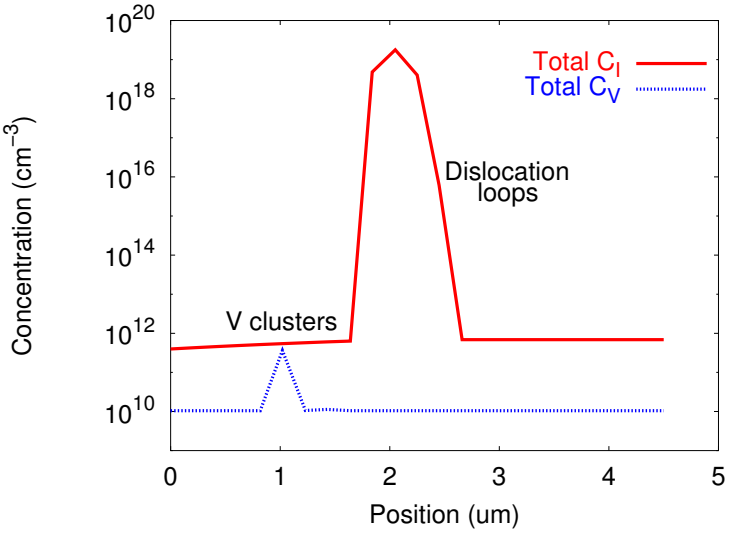

[b]

Figure 4.16: Point defect distribution with 2.3MeV Si ion implantation at dose of 10^{15} [a] and 5×10^{14}cm^{-2} [b], followed by 900°C annealing for 1 h. Total C_I and C_V represent the sum of total point defect concentration in the clusters and free point defect concentration respectively. The concentration of vacancy clusters in (b) is much lower, while the concentrations of dislocation loops remain approximately equal in both cases.

Chapter 5

USJ FORMATION

Ion implantation is the dominant doping method in today's IC manufacturing. It provides tremendous flexibility in terms of the doping species, dose and physical location of dopants. In this method, dopant ions are accelerated to hundreds or thousands of electronvolts and create a cascade of damages in the silicon lattice. The implanted ions lose energy through elastic nuclear collisions and inelastic interaction with electrons before coming to rest. The projected range, R_p, depends on the energy and type of ion used for the implantation, with higher energy and lighter ions having a deeper range. The standard deviation, $\pm\Delta R_p$, of the projected range depends on the number of random stopping events within the ion's traveling range. Heavy ions with a smaller projected range have a more narrow distribution than light ones. Due to the collisions between the silicon atoms and implanted dopant ions, Frenkel pairs (I+V) are generated. The displaced Si atoms can also collide with other Si atoms in other lattice sites and create more point defects. A vacancy-rich region forms near surface, while an interstitial-rich region is present deeper into the silicon wafer. Most of the dopants do not sit at substitutional sites after implantation, and therefore, they are not electrically active. The final junction requires careful annealing to repair the damage from the ion implantation and to activate the dopants.

During annealing to activate the dopants, diffusion also occurs, which makes it difficult to form shallow junctions. Enhanced dopant diffusion following ion implantation was first observed by Hofker *et al.* [68]. A burst of diffusion is observed, much faster than for a similar annealing condition when no implant damage is present. This phenomena is referred to transient-enhanced diffusion (TED). Fig. 5.1 illustrates TED of a B profile implanted into float-zone (FZ) crystalline silicon [146]. After 35 min annealing at 800°C, the tail of B profile has diffused more over 700$\mathring{A}$, where the equilibrium diffusion length is only ∼25$\mathring{A}$ for the same annealing condition. It is believed that the supersaturation of excess interstitials

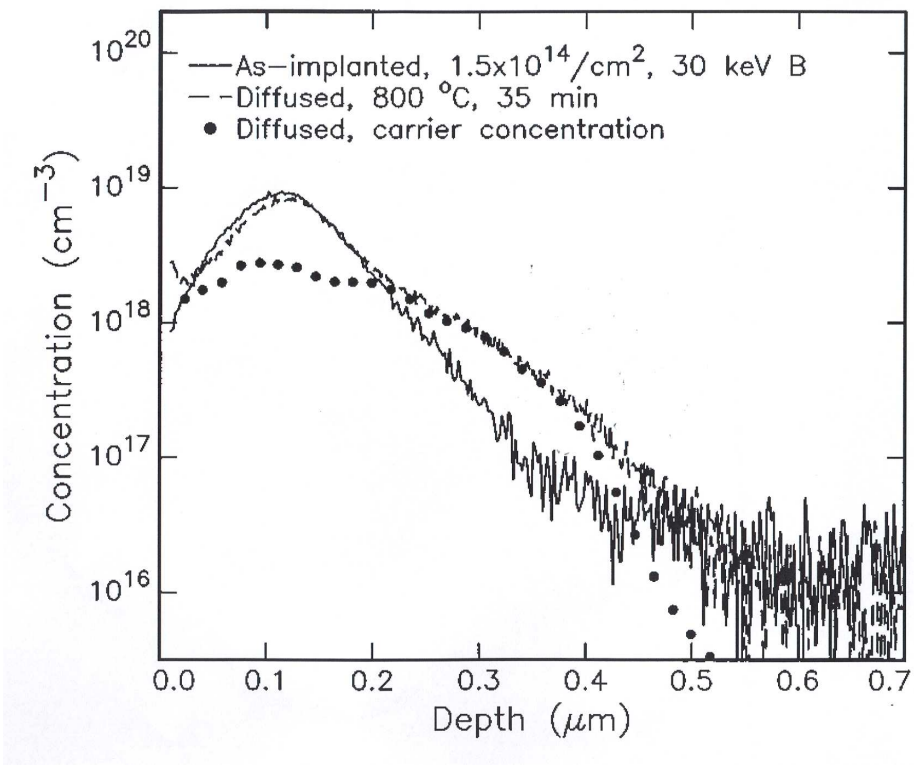

Figure 5.1: SIMS (lines) and SRP (solid circles) profiles of implanted boron in FZ silicon (30keV, 1.5×10^{14} cm^{-2}) before and after damage annealing at 800°C for 35 min. The peak of the profile is immobile and shows relatively low electrical activation. Data is from Stolk *et al.* [146].

is the source of TED. Stolk *et al.* [144] suggested that TED occurs by the emission of silicon self-interstitials from {311} clusters (also called rod-like defects) during the annealing of ion implanted silicon. Eaglesham [32] and Stolk *et al.* [146] observed the presence and evolution of {311} defects (Figs. 5.2 and 5.3) during annealing.

Another feature in Fig. 5.1 is that the peak portion of B profile above 1×10^{18} cm^{-3} is immobile and not electrically activated. Cowern *et al.* [22, 23, 24, 25] suggested that excess interstitials react with B atoms and form boron interstitial clusters (BICs) when a high concentration of B is present. BICs reduce the number of electrically active (and mobile) boron atoms, which degrade the conductivity of ultra shallow junctions (USJ). In the past, boron marker-layer structures have been widely used to study the mechanisms of

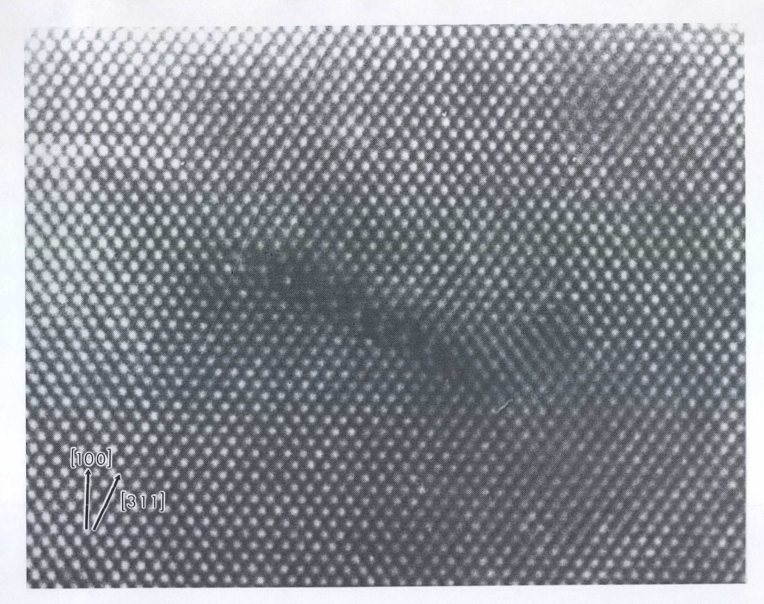

Figure 5.2: Cross-section high resolution electron microscopy showing {311} habit plane and typical contrast of {311} defects from Stolk *et al.* [146].

formation and ripening of boron-interstitial clusters (BICs) and their influence on transient enhanced diffusion (TED) [33, 105, 106, 107, 124, 125, 140, 145, 146]. In these experiments, implantation damage acts as a localized source of the interstitial on well-separated dopant-profiles. This provides insight about TED due to the supersaturation of interstitials and the formation of immobile BICs.

Several methods have been used to suppress the TED effect. Preamorphization can be done prior to dopant implantation to achieve a reduction in TED [156], but the Si a/c interface increases the junction leakage [16]. C co-implantation can be used to reduce the TED of B [22], which is due to the fact that C provides a sink for excess interstitials during annealing [76].

In this chapter, we will first study the transient enhanced diffusion with the incorporation of interstitial clusters and {311} defects. We will then focus on the mechanisms of dopant activation for a comprehensive understanding of the formation of USJ.

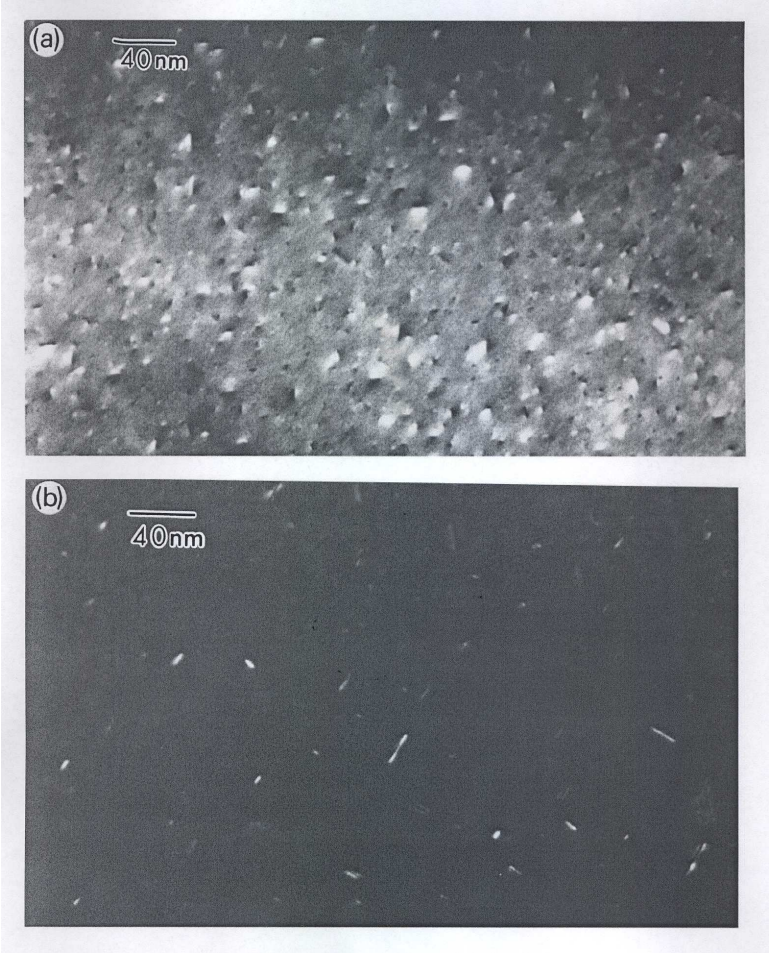

Figure 5.3: Stolk *et al.* [146] reported the plan-view $< 220 >$ dark-field image of FZ silicon implanted with $5 \times 10^{13}\text{cm}^{-2}$, 40keV Si after RTA at 815°C for (a) 5s and (b) 30s. The density of {311} defects drops substantially from 5s to 30s, while the average length of these defects increases roughly from 5 to 20 nm.

5.1 TED and {311} Evolution

It is well established that TED arises from the excess silicon interstitials generated after ion implantation. The enhanced dopant diffusivity, D_A^{enh}, is given by [35]

$$D_A^{enh} = D_A^* \frac{C_\mathrm{I}}{C_\mathrm{I}^*}, \tag{5.1}$$

where D_A^* and C_I^* are the dopant diffusivity and interstitial concentration under equilibrium. The interstitial supersaturation therefore enhances the dopant diffusivity via Eq. 5.1. TED is believed to be correlated with {311} defects in silicon, and has been attributed to the excess point defects introduced by ion implantation [144]. The atomic structure of {311} defects has been characterized experimentally by high resolution transmission electron microscopy (HRTEM) [146], shown in Figs. 5.2. Rod-like {311} defects are formed by the agglomeration of self-interstitials into planar defects which are elongated primarily along <100> directions (interstitial chain) and lie in {311} planes. Although TED has less impact under rapid thermal annealing conditions, it remains a severe constraint due to the down-scaling of the device dimension. Suppressing TED therefore becomes an important technological challenge.

In addition to {311} defects, Zhang *et al.* [165] suggested the existence of small compact interstitial clusters (IC's), and observation from Benton *et al.* [8] confirmed the presence of small IC's by DLTS. Therefore, to be able to accurately predict TED, we should model the evolution of small interstitial clusters as well as {311} defects.

Stress/strain has been incorporated into the process of today's VLSI technology to enhance carrier mobility [130, 159]. It has a substantial impact on transient enhanced diffusion (TED) and dopant activation in ultra-shallow junctions. In conjunction with Chen-Luen Shih [135], we have applied the RKPM-DFA to the analysis of the dynamic behavior of {311} defects followed by a comparison to experimental data. Together with the *ab-initio* calculation from Chihak Ahn [2], we study stress effects on point defect clustering.

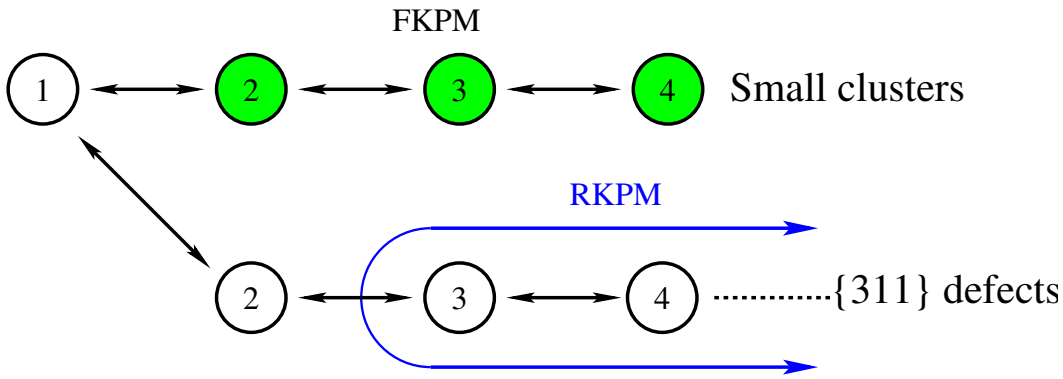

Figure 5.4: A schematic shows the concept of RKPM for I clustering. FKPM is used for small interstitial clusters, while RKPM describes the behavior of {311} precipitation from size k=3.

5.1.1 RKPM-DFA for {311} and Vacancy Clustering

The evolution of {311} defects plays an important role in transient enhance diffusion (TED). The excess vacancies either recombine with interstitials in the bulk, diffuse the the surface, or cluster as voids in the vacancy-rich region. In this section, we use the reduced moment-based kinetic precipitation model (RKPM) with delta-function approximation (DFA), introduced in Chapter 3, to describe the clustering mechanisms for both interstitials and vacancies. Kim *et al.* [87] reported lower formation energy for small IC's up to size 4 compared to {311} defects. In this work, these small clusters are described by the full kinetic precipitation model (FKPM) using Eqs. 3.2 and 3.3, while RKPM-DFA is used for the {311} defects to enhance the computing efficiency. A schematic for the formation of small interstitial clusters and {311} defects is shown in Fig. 5.4.

The RKPM-DFA is applied on both {311} and vacancy clustering, where k is chosen as 3 and 36 respectively. Following the approach from Section 3.4, the time evolution of the first two moments for both {311} defects and vacancy clusters, ($m_0^{\mathrm{I}}, m_1^{\mathrm{I}}, m_0^{\mathrm{V}}$, and m_1^{V}), can then be derived as

$$\frac{\partial m_0^{\mathrm{I}}}{\partial t} = I_3^{\mathrm{I}} = D_{\mathrm{I}}\lambda_2^{\mathrm{I}}\left[C_{\mathrm{I}}f_2^{\mathrm{I}} - m_0^{\mathrm{I}}C_2^{*\mathrm{I}}\hat{f}_3^{\mathrm{I}}\right], \tag{5.2}$$

$$\frac{\partial m_1^{\mathrm{I}}}{\partial t} = 3I_3^{\mathrm{I}} + D_{\mathrm{I}}m_0^{\mathrm{I}}\lambda_{\hat{m}_1^{\mathrm{I}}}^{\mathrm{I}}\left(C_{\mathrm{I}} - C_{ss}^{\mathrm{I}}C_{\hat{m}_1^{\mathrm{I}}+1}^{*}\right), \tag{5.3}$$

$$\frac{\partial m_0^{\mathrm{V}}}{\partial t} = I_{36}^{\mathrm{V}} = D_{\mathrm{V}}\lambda_{35}^{\mathrm{V}}\left[C_{\mathrm{V}}f_{35}^{\mathrm{V}} - C_{35}^{*\mathrm{V}}\hat{f}_{36}^{\mathrm{V}}\right], \tag{5.4}$$

$$\frac{\partial m_1^{\mathrm{V}}}{\partial t} = 36I_{36}^{\mathrm{V}} + D_{\mathrm{V}}m_0^{\mathrm{V}}\lambda_{\hat{m}_1^{\mathrm{V}}}^{\mathrm{V}}\left(C_{\mathrm{V}} - C_{ss}^{\mathrm{V}}C_{\hat{m}_1^{\mathrm{V}}+1}^{*}\right), \tag{5.5}$$

where $\hat{m}_1$ is the average size of precipitates, f_n is the concentration of precipitates with size n, and C_n^* is the solute concentration that would be in equilibrium with a size n precipitate. D_{I} and D_{V} are the diffusivities for point defects. The kinetic growth factor, λ_n, depends on the size and geometry of precipitates. Often the system is assumed to be diffusion-limited, and λ_n is defined as A_n/R_n, where A_n and R_n are the surface area and effective radius for a size n precipitate. The detailed derivation of λ_n for $\{311\}$ defects is given in Appendix B. $\hat{f}_3^{\mathrm{I}}$ (Eq. 5.6) and $\hat{f}_{36}^{\mathrm{V}}$ (Eq. 3.25) were described mathematically as functions of average size. Fig. 5.5 demonstrates how Eq. 5.6 matches the simulation results from the FKPM under different conditions.

$$\hat{f}_k^{\mathrm{I}}(\hat{m}_1^{\mathrm{I}}) = \left[1 - \left(\frac{\hat{m}_1^{\mathrm{I}} - k}{k+1}\right)\right]^3 \cdot [1-\xi] + \xi \cdot \left(\frac{k}{\hat{m}_1^{\mathrm{I}}}\right)^{2.5}, \tag{5.6}$$

where $k = 3$ and $\xi = 0.84\exp\left(-\frac{0.115}{kT}\right)$ in our model. The first part of Eq. 5.6 describes the asymptotic behavior for small clusters ($\hat{f}_k \to 1$ as $\hat{m}_1 \to k$), and ξ gives the Arrhenius dependence for $\hat{f}_k^{\mathrm{I}} = \hat{f}_3^{\mathrm{I}}$.

5.1.2 Recombination of Point Defects with {311} and Vacancy Clusters

The recombination of excess point defects is taken into account, because a free interstitial is very likely to occupy a vacancy site. An interstitial cluster can also recombine with a vacancy and vice versa.

$$\mathrm{I} + \mathrm{V} \iff \emptyset \tag{5.7}$$

$$\mathrm{I}_{n+1} + \mathrm{V} \iff \mathrm{I}_n \tag{5.8}$$

$$\mathrm{V}_{n+1} + \mathrm{I} \iff \mathrm{V}_n \tag{5.9}$$

The reactions rates for the recombination can be written as

$$R_{\mathrm{I/V}} = 4\pi a_0(D_{\mathrm{I}} + D_{\mathrm{V}})(C_{\mathrm{I}}C_{\mathrm{V}} - C_{\mathrm{I}}^*C_{\mathrm{V}}^*), \tag{5.10}$$

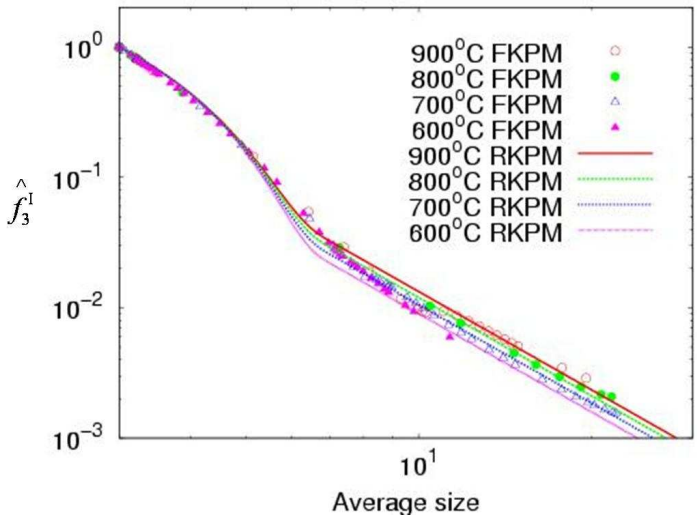

Figure 5.5: $\hat{f}_3^{\mathrm{I}}$ vs. the average size for {311} defects at different temperatures: 600, 700, 800 and 900°C. Points are generated from RFKPM under different conditions. Lines are the fitting functions with an Arrhenius dependence for larger sizes (Eq. 5.6).

$$R_{\mathrm{I}_{n+1}/\mathrm{V}} = 4\pi\lambda_{n+1}^{\mathrm{I}} D_{\mathrm{V}} \left(C_{\mathrm{V}} f_{n+1}^{\mathrm{I}} - \frac{f_n^{\mathrm{I}}}{K_{\mathrm{I}_{n+1}/\mathrm{V}}} \right), \tag{5.11}$$

$$R_{\mathrm{V}_{n+1}/\mathrm{I}} = 4\pi\lambda_{n+1}^{\mathrm{V}} D_{\mathrm{I}} \left(C_{\mathrm{I}} f_{n+1}^{\mathrm{V}} - \frac{f_n^{\mathrm{V}}}{K_{\mathrm{V}_{n+1}/\mathrm{I}}} \right), \tag{5.12}$$

where C_{I}^* and C_{V}^* are the equilibrium concentrations of interstitials and vacancies, a_0 is the silicon lattice space, and $K_{\mathrm{V}_{n+1}/\mathrm{I}}$ and $K_{\mathrm{I}_{n+1}/\mathrm{V}}$ are the equilibrium constants. Since the reverse reactions in Eqs. 5.8 and 5.9 are very unlikely to proceed due to high activation barrier, we assumed that the 2^{nd} terms in Eqs. 5.11 and 5.12 could be omitted for simplification.

$$R_{\mathrm{I}_{n+1}/\mathrm{V}} = 4\pi\lambda_{n+1}^{\mathrm{I}} D_{\mathrm{V}} \left(C_{\mathrm{V}} f_{n+1}^{\mathrm{I}} \right) \tag{5.13}$$

$$R_{\mathrm{V}_{n+1}/\mathrm{I}} = 4\pi\lambda_{n+1}^{\mathrm{V}} D_{\mathrm{I}} \left(C_{\mathrm{I}} f_{n+1}^{\mathrm{V}} \right) \tag{5.14}$$

Combining both the precipitation and recombination of {311} defects and vacancy clusters (Eqs. 5.2 to 5.5 and Eqs. 5.13 to 5.14), the time evolution of the first two moments for both {311} defects and vacancy clusters, ($m_0^{\mathrm{I}}, m_1^{\mathrm{I}}, m_0^{\mathrm{V}}$, and m_1^{V}), can then be expressed as

$$\frac{\partial m_0^{\mathrm{I}}}{\partial t} = \lambda_2^{\mathrm{I}} D_{\mathrm{I}} \left[C_{\mathrm{I}} f_2^{\mathrm{I}} - m_0^{\mathrm{I}} C_2^{*\mathrm{I}} \hat{f}_3^{\mathrm{I}} \right] - \lambda_3^{\mathrm{I}} D_{\mathrm{V}} m_0^{\mathrm{I}} \left(C_{\mathrm{V}} \hat{f}_3^{\mathrm{I}} \right) \tag{5.15}$$

$$\frac{\partial m_1^{\mathrm{I}}}{\partial t} = 3I_3^{\mathrm{I}} + \lambda^{\mathrm{I}}_{\hat{m}_1^{\mathrm{I}}} D_{\mathrm{I}} m_0^{\mathrm{I}} \left(C_{\mathrm{I}} - C^{\mathrm{I}}_{ss} C^{*}_{\hat{m}_1^{\mathrm{I}}+1} \right) - 3R_{\mathrm{I}_3/\mathrm{V}} - \lambda^{\mathrm{I}}_{\hat{m}_1^{\mathrm{I}}} D_{\mathrm{V}} m_0^{\mathrm{I}} C_{\mathrm{V}} \tag{5.16}$$

$$\frac{\partial m_0^{\mathrm{V}}}{\partial t} = \lambda^{\mathrm{V}}_{35} D_{\mathrm{V}} \left[C_{\mathrm{V}} f^{\mathrm{V}}_{35} - m_0^{\mathrm{V}} C^{*\mathrm{V}}_{35} \hat{f}^{\mathrm{V}}_{36} \right] - \lambda^{\mathrm{V}}_{36} D_{\mathrm{I}} m_0^{\mathrm{V}} \left(C_{\mathrm{I}} \hat{f}^{\mathrm{V}}_{36} \right) \tag{5.17}$$

$$\frac{\partial m_1^{\mathrm{V}}}{\partial t} = 36I_{36}^{\mathrm{V}} + \lambda^{\mathrm{V}}_{\hat{m}_1^{\mathrm{V}}} D_{\mathrm{V}} m_0^{\mathrm{V}} \left(C_{\mathrm{V}} - C^{\mathrm{V}}_{ss} C^{*}_{\hat{m}_1^{\mathrm{V}}+1} \right) - 36R_{\mathrm{V}_{36}/\mathrm{I}} - \lambda^{\mathrm{V}}_{\hat{m}_1^{\mathrm{V}}} D_{\mathrm{I}} m_0^{\mathrm{V}} C_{\mathrm{I}}. \tag{5.18}$$

The time evolution of small I ($n < 3$) and V ($n < 36$) clusters are described with the FKPM using Eqs. 3.2 and 3.3. We also keep track of the concentrations of point defects through each reaction. This set of equations fully describes the system for transient enhanced diffusion (TED).

5.1.3 Comparison to Experimental Data

The simulation results from both FKPM and RKPM-DFA are compared to the experimental data from Cowern *et al.* [24] (Fig. 5.7[a]). Cowern *et al.* performed 25keV Si ion implantation with a dose of $2\times10^{13}\mathrm{cm}^{-2}$, and then tracked diffusion of a buried boron epitaxy layer. Interstitial supersaturation can be obtained, assuming that boron diffuses via interstitials.

The initial profiles for point defects after ion implantation were first generated via SRIM [169] and shown in Fig. 5.6. The total interstitial and vacancy profiles overlap with each other, but the net concentration profiles show a distinction between interstitial-rich and vacancy-rich regions. In Fig. 5.7[a], it is shown that the time evolution of interstitial supersaturation is well characterized by both FKPM and RKPM. At 600°C, TED lasts about five orders of magnitude longer than at 800°C. Note that two regions of supersaturation under each temperature have a steeper slope. This can be explained by the existence of small clusters and {311} defects. As shown in Fig. 5.8, the dissolution of small clusters causes a sudden decrease of supersaturation first, while the dissolution of {311} defects gives the later drop. The comparison of the average {311} size is shown in Fig. 5.7 [b]. RKPM-DFA again shows the ability to enhance the computing efficiency, while the accuracy from FKPM is still maintained.

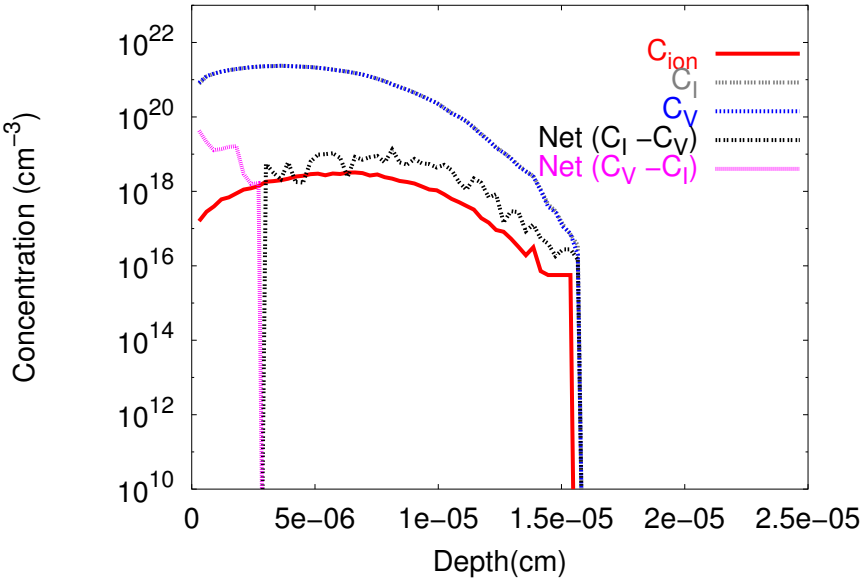

Figure 5.6: The initial profiles of Si ions and point defects generated by SRIM [169] at 25keV with a dose of 2×10^{13}cm^{-2} Si ions. The vacancy-rich region is closer to the surface while the interstitial-rich region is deeper into the epitaxy layer.

5.1.4 Stress Effects on {311} Formation

In today's VLSI technology, the incorporation of stress/strain is one of the trends in nanoscale device technology, due to the fact that strain can enhance carrier mobility [130, 159]. Stress/strain also has a large impact on transient enhanced diffusion (TED) and dopant activation in ultra-shallow junctions. It changes the small cluster binding energies, effective solubility for {311} defects, diffusivities (D_{I} and D_{V}), and the equilibrium point-defect concentration (C_{I}^{*} and C_{V}^{*}). Chihak Ahn [2] used the density functional theory (DFT) code VASP [94] with ultrasoft Vanderbilt type pseudopotentials [93, 153] for the calculations. All calculations were performed in general gradient approximation (GGA) with a 64 silicon atom supercell and a 2^3 Monkhorst-Pack **k**-point sampling. The energy cut-off was 250eV. The change in energy due to strain is

$$\Delta E_f(\vec{\sigma}) = -\Omega_0 \Delta\vec{\epsilon}\cdot\vec{\sigma}, \tag{5.19}$$

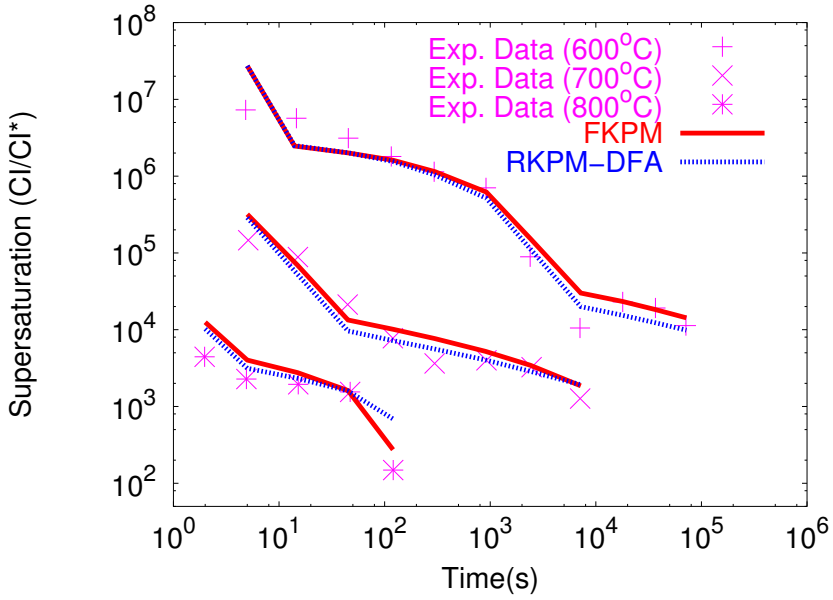

[a]

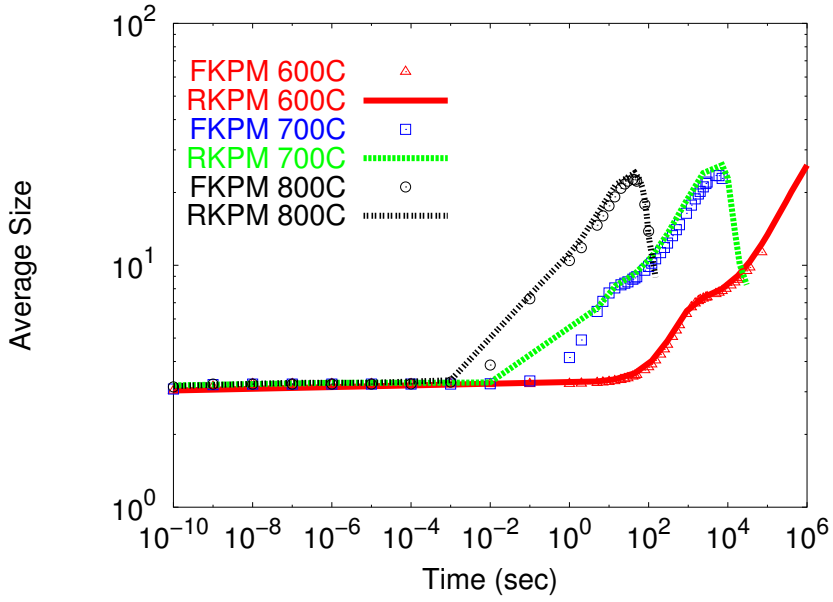

[b]

Figure 5.7: [a] Interstitial supersaturation as a function of annealing time and temperature. Symbols represent the experimental data reported by Cowern *et al.* [24] and lines are the simulation results from discrete and moment-based models using the delta function approximation. [b] The comparison of the time evolution of {311} average size ($\hat{m}_1$) between FKPM and RKPM-DFA at different temperatures.

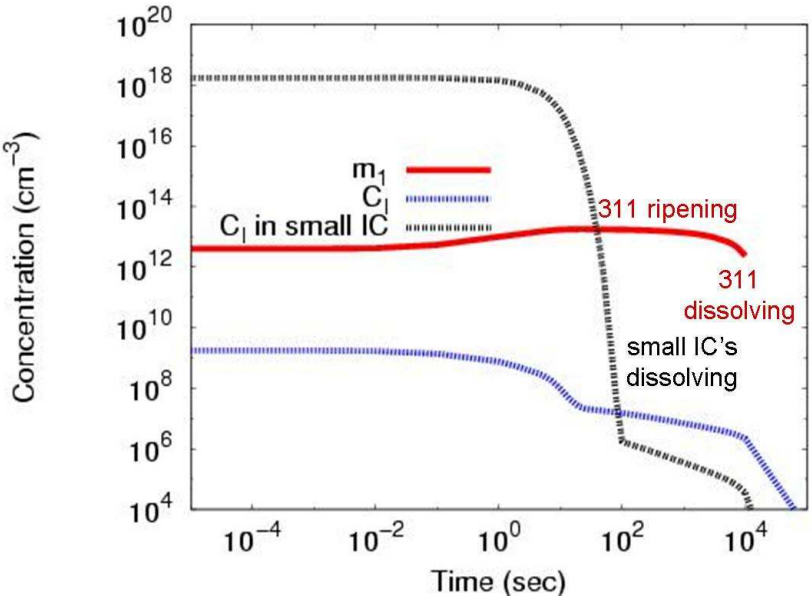

Figure 5.8: The time evolutions of m_1, free interstitial, and total interstitials in small IC's at 700°C. After ion implantation, excess interstitials form small IC's and {311} defects during the beginning of annealing. Small clusters then dissolve, follow by the ripening and then dissolution of {311} defects.

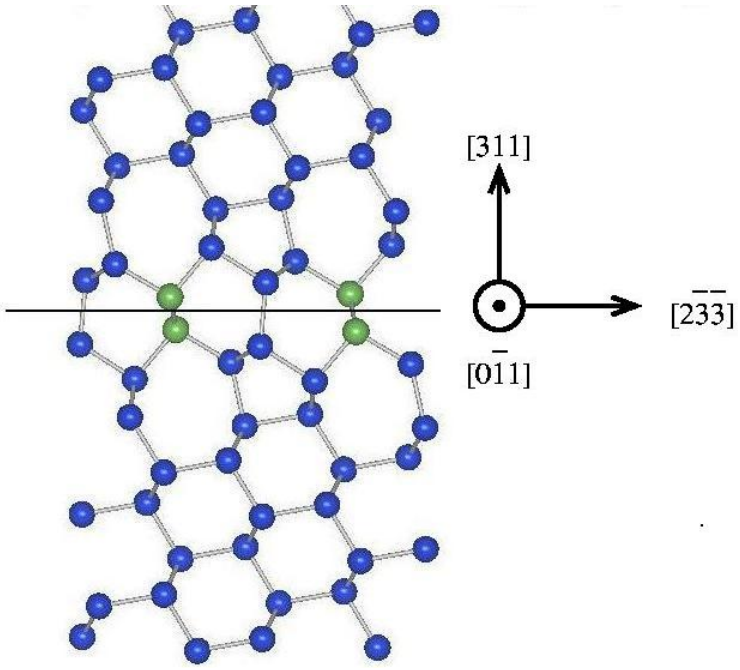

Figure 5.9: The {311} structure used for *ab-initio* calculation [88].

where Ω_0 is the atomic volume, and $\vec{\sigma}$ is the applied stress tensor. Induced strain ($\Delta\vec{\epsilon}$) is the amount of lattice change because of relaxation after introducing the defect. The calculated induced strain ($\Delta\vec{\epsilon}$) for interstitial clusters is shown in Tables 5.1. The reader interested in the detailed method using Hooke's law to extrapolate the induced strains is referred to the work of Diebel [28].

For the two most important structures, isolated interstitial and {311} defects, asymmetric induced strains were taken into account in the calculations. The possible {311} plane configuration reported by Kim *et al.* [88] was adopted and is shown in Fig. 5.9. The induced strains for I_3 and I_4 were derived from hydrostatic calculations. Given the strain/stress state, the energy change for interstitial cluster growth reaction

$$I_{n-1} + I \Leftrightarrow I_n \tag{5.20}$$

can be written as

$$\Delta E_n(\vec{\sigma}) = -\Omega_0 \sum \left[n \cdot \Delta\vec{\epsilon}_{I_n} - (n-1) \cdot \Delta\vec{\epsilon}_{I_{n-1}} - \Delta\vec{\epsilon}_I \right] \cdot \vec{\sigma}. \tag{5.21}$$

Table 5.1: Induced strains for interstitial clusters. For two key structures (I_{split} and I_{311}), asymmetry was fully accounted for. Single number indicates all diagonal components of the vector have same value.

	I_{split}	I_2	I_3	I_4
$\Delta\epsilon$ (eV)	[0.26, 0.26, 0.047]	0.16	0.36	0.36

	I_{311}
$\Delta\epsilon$ (eV)	$\begin{bmatrix} 0.29 & 0.086 & 0.084 \\ 0.086 & 0.29 & 0.084 \\ 0.084 & 0.084 & 0.57 \end{bmatrix}$

The local equilibrium constant (Eq. 3.4) with the transition of precipitate size from $n-1$ to n under stress can then be modified to

$$C_n^*(\vec{\sigma}) = C_n^*(0) \exp\left[\frac{\Delta E_n(\vec{\sigma})}{kT}\right], \tag{5.22}$$

where $C_n^*(0)$ is the equilibrium constant under a stress-free condition. The modification of I diffusivity under stress can be calculated as [28]

$$\frac{D_I(\vec{\sigma})}{D_I(0)} = \exp\left[\frac{\Omega_0(\Delta\vec{\epsilon}_T - \Delta\vec{\epsilon}_I)\cdot\vec{\sigma}}{kT}\right], \tag{5.23}$$

where $\Delta\vec{\epsilon}_T$ and $\Delta\vec{\epsilon}_I$ are the induced strains for I transition state and I_{split}.

We have used parameters under both tensile and compressive strain conditions to simulate the corresponding behaviors. Both interstitials and interstitial clusters reduce their energy under tensile stress condition. However, I clusters (I_3, I_4 , and I_{311}) have a even stronger stress dependence due to the larger induced strains. Thus, compressive stress favors the formation of free interstitials relative to small IC's and {311} defects. Figs. 5.10 [a], [b], and [c] show the predictions for I cluster evolution under $\epsilon = 1\%$ biaxial strain compared to stress free conditions. Tensile stress favors both small I clusters and {311} formation, giving a longer but less intense TED period, while compressive stress has the opposite effect (higher I supersaturation but for shorter TED time). Also, the formation and dissolution of {311} defects take place earlier under compressive stress.

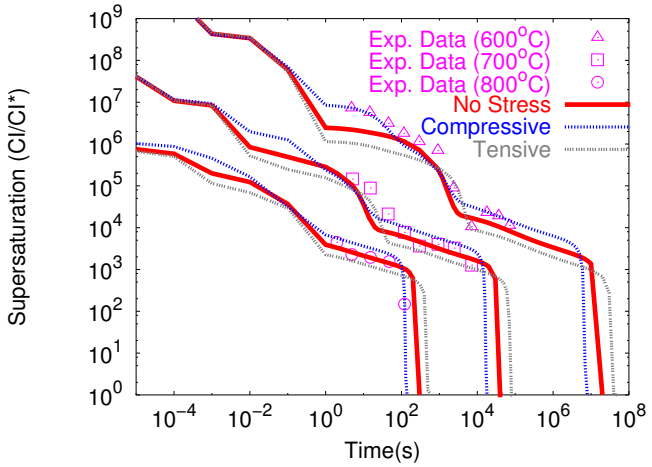

[a]

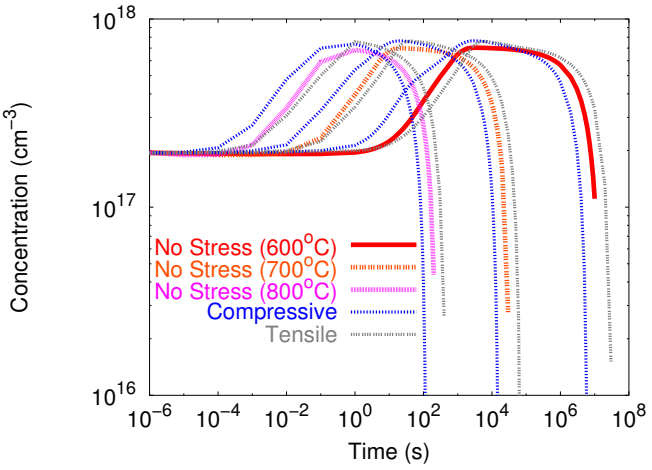

[b]

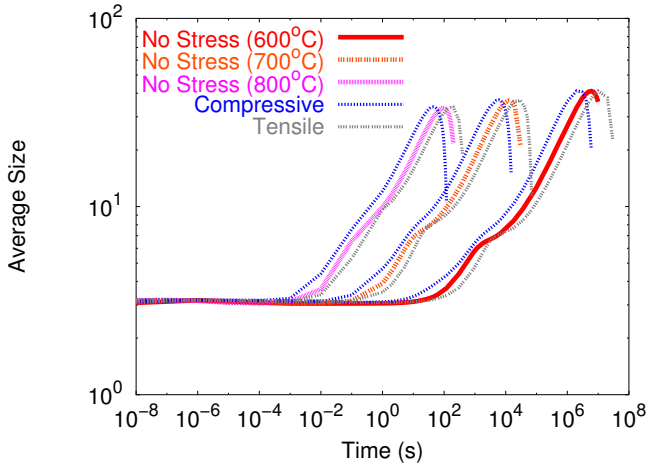

[c]

Figure 5.10: Simulation results of {311} defect evolution under $\epsilon = 1\%$ biaxial strain compares to stress-free condition. (a) Interstitial supersaturation; (b) interstitial concentration in I clusters; (c) {311} defect average size. Supersaturation lasts longer under tensile stress, while I supersaturation is larger for compressive stress.

5.2 Boron Activation/Deactivation

Ion implantation and high temperature annealing are currently the most common process steps for ultra-shallow-junction (USJ) formation. Dopant TED and deactivation due to clustering remain as the critical issues when Si device dimensions continue down-scaling below 50nm [146]. In Section 5.1, we have discussed the TED effects due to interstitial supersaturation, and we will focus on the formation of BICs and the dopant activation/deactivation in this section.

Eaglesham *et al.* [33] and Stolk *et al.* [145, 146] observed that significant fractions of implanted B are immobile and inactive during thermal annealing; this phenomenon occurs when the B concentration is above $1 \times 10^{18} \mathrm{cm}^{-3}$, as shown in Fig. 5.1. Cowern *et al.* [23, 24] assumed that the formation of immobile boron-interstitial clusters is due to the participation of excess interstitials. BICs must contain only a few boron atoms due to the fact that no indication of BICs was found from high-resolution transmission-electronic-microscopy analysis by Stolk *et al.* [145] and Zhang *et al.* [165]. In the experiments by Pelaz *et al.* [124, 125], boron marker-layer structures with 40keV Si ion implantation were annealed at 790°C for 10 min. Resulting SIMS profiles are shown in Fig. 5.11. All the peaks of boron profiles experienced TED, while only the ones within the damaged region (or near the surface) remained sharp. This indicates that boron atoms within the damaged region are immobile due to the formation of BICs. The model they used to match data states that immobile precursors, BI_2, were first formed during the earlier stage of annealing, and acted as nucleation centers for the formation of B_3I or B_4I [124, 125].

Haynes *et al.* [59] and Lilak *et al.* [99] concluded that there is a significant decrease of interstitials in {311} defects with an increase of B concentration and suggested the formation of BICs, which reduces the free interstitials available for B diffusion and the formation of {311} defects. Lilak *et al.* [99] concluded that B_3I or B_4I complexes are responsible for the majority of BICs. Mannino *et al.* [105] studied the formation, evolution and stability of BICs by comparing diffusion data from boron-marked layers with and without a BIC defect band near the surface of wafers. Mannino *et al.* [107] further investigated the effects of different damaging implant doses on boron activation via measurement of chemical (SIMS)

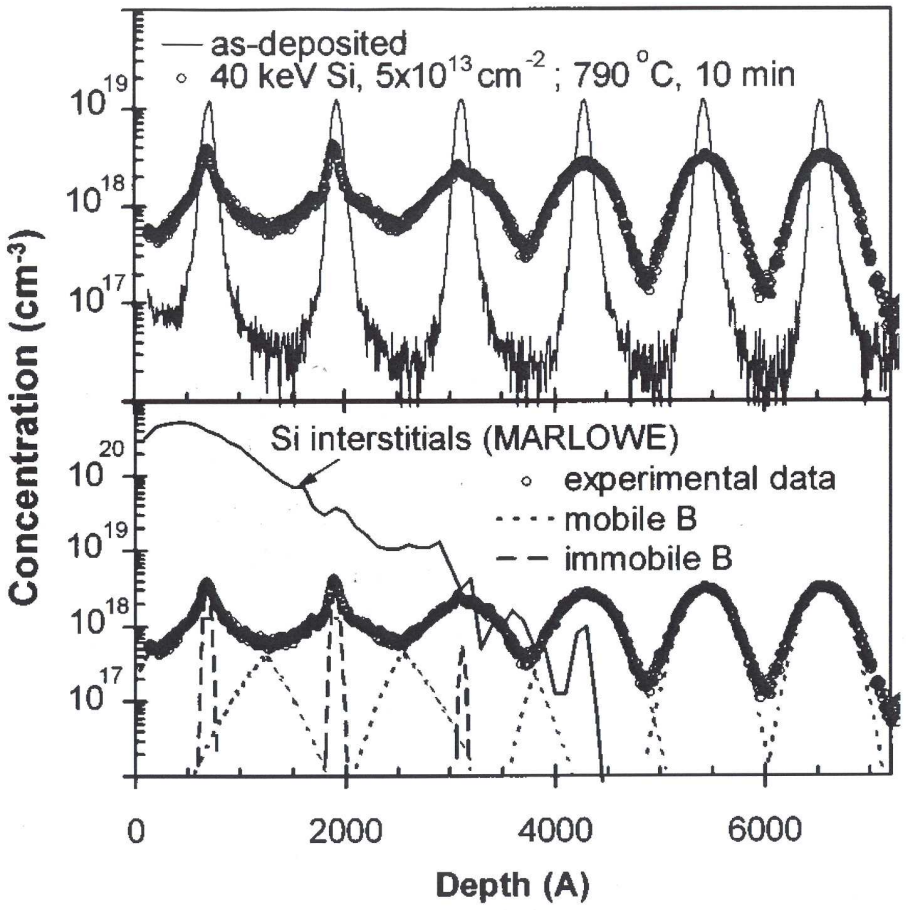

Figure 5.11: (a) SIMS profiles in B-doped MBE silicon layer after 40keV Si implantation with a dose of 5×10^{13} cm^{-2} and 10 min annealing at 790°C. (b) Deconvolution of the doping markers into Gaussian diffusion profiles and an immobile fraction in the near-surface spikes, along with the MARLOWE calculation of the initial distribution after implantation. Less B peak broadening in the damaged region indicates the formation of immobile BICs. Data is from Pelaz *et al.* [125].

and electrically active doping concentration (SRP). Comparing SRP to SIMS profiles reveals that higher implant doses result in lower boron activation. Mannino *et al.* [105] also concluded that BICs are more stable than small interstitial clusters and {311} defects. Solmi *et al.* [140] further confirmed that BICs act as a sink for interstitials in the early stage of annealing, substantially reducing TED. Therefore, BICs provide a moderate Si-interstitial supersaturation even when interstitial clusters and {311} defects are dissolved.

Several studies using *ab-initio* calculation have been conducted to complement the experimental work and determine the structure and formation energies of B_nI_m [98, 102, 161, 166, 168]. Zhu *et al.* [166, 168] calculated the diffusion and activation energies for boron-interstitial pair including charge-states. Liu *et al.* [102] and Windl *et al.* [161] later reported the structures and formation energies for BICs, and concluded that B_3I is a key cluster while $B_{12}I_7$ is the most stable cluster. Recent work from Lenosky *et al.* [98] suggested that neutral B_3I is a stable nucleus that can grow to larger clusters.

Summarizing from the literature reviews, the mechanisms of boron activation/deactivation involve TED and the formation of BICs. TED is driven by interstitial supersaturation due to the presence of small interstitial clusters and {311} defects. Boron atoms interact with point-defects to form clusters which appear to be electrically inactive. To form ultra-shallow-junctions, TED has to be carefully controlled, while boron atoms need to be electrically active. Post annealing is required to activate boron atoms after ion implantation. During this process, interstitials agglomerate into either small interstitial clusters, {311} defects, or BICs. Under high boron concentration and interstitial supersaturation, BI_2 is first formed in the early stage of annealing and grows into larger BICs. The formation of BICs lowers the boron apparent solubility and slows the formation of {311} defects, which reduces TED effects. Higher interstitial supersaturation results in lower boron activation. BICs are immobile and appear to be more stable than small interstitial clusters and {311} defects.

In the following sections, we will study the boron interstitial clustering model, and compare the simulation results from this model to experimental data reported by Mokhberi *et al.* [116]. This work is developed in conjunction with Chen-Luen Shih *et al.* [135].

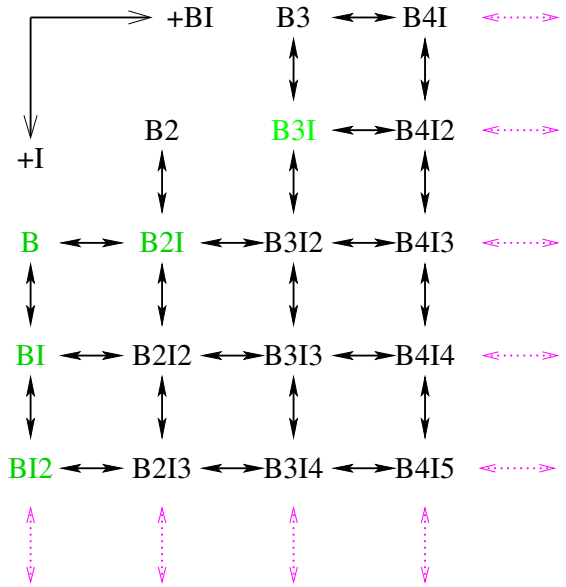

Figure 5.12: Schematic of BIC formation [102]. BICs are formed via the addition of mobile species, such as I and BI. The green BICs are the forms to be considered in the later work.

5.2.1 Boron Interstitial Clustering Model

To study the formation of BICs, the evolution of point-defects (I and V) is included. Point-defects can either cluster or recombine as shown in the reactions below.

$$\mathrm{I}_n + \mathrm{I} \iff \mathrm{I}_{n+1} \tag{5.24}$$

$$\mathrm{V}_n + \mathrm{V} \iff \mathrm{V}_{n+1} \tag{5.25}$$

$$\mathrm{I}_n + \mathrm{V} \iff \mathrm{I}_{n-1} \tag{5.26}$$

$$\mathrm{V}_n + \mathrm{I} \iff \mathrm{V}_{n-1} \tag{5.27}$$

The reduced moment-based models (RKPM) with the delta-function approximation (RKPM-DFA) of vacancy and interstitial clusters were discussed in Chapter 3 and Section 5.1. Fig. 5.12 shows the schematic of BIC formation. BICs can grow via the attachment of I or BI, which are mobile. These reactions can be expressed as:

$$\mathrm{B}_n\mathrm{I}_m + \mathrm{I} \iff \mathrm{B}_n\mathrm{I}_{m+1} \tag{5.28}$$

$$\mathrm{B}_n\mathrm{I}_m + \mathrm{BI} \iff \mathrm{B}_{n+1}\mathrm{I}_{m+1}, \tag{5.29}$$

where n and m are the numbers of boron and interstitial atoms in the cluster. Similar to the analysis from Chapter 3, the rate equations for Eqs. 5.28 and 5.29 can be written as:

$$R_{\mathrm{B}_n\mathrm{I}_m/\mathrm{I}} = 4\pi a_0 D_{\mathrm{I}} \left(C_{\mathrm{B}_n\mathrm{I}_m} C_{\mathrm{I}} - \frac{C_{\mathrm{B}_n\mathrm{I}_{m+1}}}{K_{\mathrm{B}_n\mathrm{I}_m/\mathrm{I}}} \right) \tag{5.30}$$

$$R_{\mathrm{B}_n\mathrm{I}_m/\mathrm{BI}} = 4\pi a_0 D_{\mathrm{BI}} \left(C_{\mathrm{B}_n\mathrm{I}_m} C_{\mathrm{BI}} - \frac{C_{\mathrm{B}_{n+1}\mathrm{I}_{m+1}}}{K_{\mathrm{B}_n\mathrm{I}_m/\mathrm{BI}}} \right) \tag{5.31}$$

where a_0 is the capture radius for the reaction, the K's stand for equilibrium constants, and D and C are the diffusivity and concentration, respectively.

This work is following the analysis from Chakravarthi *et al.* [18] and Meyer *et al.* [115]. Chakravarthi *et al.* [18] first adopted the results from *ab-initio* calculations and concluded: (1) all small clusters rapidly reach equilibrium with free boron and interstitial concentrations; (2) BI_2 is the dominant cluster during the early stage of annealing; (3) $\mathrm{B}_3\mathrm{I}$ becomes the dominant cluster at longer times and needs to be solved numerically. Chakravarthi *et al.* [18] further extend the modeling by including the charge states of clusters based on the charged defect calculations from Lenosky [97], where $(\mathrm{BI}_2)^+$, $(\mathrm{B}_2\mathrm{I})^0$, and $(\mathrm{B}_3\mathrm{I})^-$ are the dominant charged clusters. Meyer *et al.* [115] only considered $(\mathrm{BI}_2)^+$, $(\mathrm{B}_2\mathrm{I})^0$, and $(\mathrm{B}_3\mathrm{I})$, where $(\mathrm{B}_3\mathrm{I})$ is neutral compared to the one from Chakravarthi *et al.* [18]. Later work from Lenosky *et al.* [98] suggested that $(\mathrm{B}_3\mathrm{I})$ is neutral when present in heavily doped p-type material. *Ab-initio* calculations from Henkelman *et al.* [62] further proposed that $(\mathrm{B}_3\mathrm{I}_2)^{\mathrm{Linear}}$ and $(\mathrm{B}_3\mathrm{I}_2)^{\mathrm{Trigonal}}$ are the two intermediate species for the transformation between $\mathrm{B}_2\mathrm{I}$ + BI and $\mathrm{B}_3\mathrm{I}$ + I. These two intermediate states have similar energies but are separated by a substitutional barrier. Meyer *et al.* [115] expressed the proposed mechanism as:

$$(\mathrm{B}_2\mathrm{I})^0 + (\mathrm{BI})^0 \underset{k_1^r}{\overset{k_1^f}{\Longleftrightarrow}} (\mathrm{B}_3\mathrm{I}_2)^{\mathrm{Linear}} \underset{k_2^r}{\overset{k_2^f}{\Longleftrightarrow}} (\mathrm{B}_3\mathrm{I}_2)^{\mathrm{Trigonal}} \underset{k_3^r}{\overset{k_3^f}{\Longleftrightarrow}} (\mathrm{B}_3\mathrm{I})^0 + \mathrm{I}^0. \tag{5.32}$$

The resulting net formation rate was written as:

$$R_{(\mathrm{BI})^0/(\mathrm{B}_2\mathrm{I})^0} = k_1^f \gamma \left[C_{(\mathrm{B}_2\mathrm{I})^0} C_{(\mathrm{BI})^0} - \frac{C_{(\mathrm{B}_3\mathrm{I})^0} C_{\mathrm{I}^0}}{K} \right], \tag{5.33}$$

where

$$\gamma = \left[\frac{k_2^f k_3^f}{k_1^r k_2^r + (k_1^r + k_2^f) k_3^f} \right] = \frac{1}{1 + A \exp\left(\frac{E_a}{kT} \right)} \tag{5.34}$$

is the probability of $(B_3I_2)^{\text{Linear}}$ dissociating to (B_3I) + I, rather than (B_2I) + BI for a p-type material.

The formation energies for $(BI_2)^+$, $(B_2I)^0$, and (B_3I) were from Windl *et al.* [161]. The reaction rates were defined in terms of $C_{(BI)^-}$ and C_{B^-} for the convenience of integrating rate equations with different charge states. We will describe the clustering mechanisms for $(BI)^-$, $(BI_2)^+$, $(B_2I)^0$, and $(B_3I)^0$ in the following work.

Mobile interstitials interact with boron atoms and form BI. The reactions and rate equations are written as

$$B^- + I^0 \iff (BI)^- \tag{5.35}$$

$$B^- + I^+ \iff (BI)^0 \tag{5.36}$$

$$R_{(BI)^-} = 4\pi a_0 D_{I^-}\left(C_{B^-}C_{I^0} - \frac{C_{(BI)^-}}{K_{B^-/I^0}}\right) \tag{5.37}$$

$$R_{(BI)^0} = 4\pi a_0 D_{I^0}\left(C_{B^-}C_{I^+} - \frac{C_{(BI)^0}}{K_{B^-/I^+}}\right), \tag{5.38}$$

where K's are the equilibrium constants.

The detailed derivations for $(BI_2)^+$, $(B_2I)^0$, and $(B_3I)^0$ can be found in Appendix D. We will only briefly discuss the reactions and the final results of rate equations. $(B_2I)^0$ can be formed by the reaction between the substitutional boron (B^-) and the mobile species, $(BI)^-$ or $(BI)^0$.

$$(BI)^- + B^- \iff (B_2I)^0 + 2e^-, \tag{5.39}$$

$$(BI)^0 + B^- \iff (B_2I)^0 + e^-. \tag{5.40}$$

The sum of corresponding reaction rates for reactions 5.39 and 5.40 are

$$R_{(B_2I)^0} = 4\pi a_0 K^{eq}_{(BI)^-}\left[1 + \frac{D^+_B\left(\frac{p}{n_i}\right)}{D^0_B}\right]\left[\frac{C_{(BI)^-}C_{B^-}}{K^{eq}_{(BI)^-}} - \frac{C_{(B_2I)^0}\left(\frac{n}{n_i}\right)^2}{K^{eq}_{(B_2I)^0}}\right]. \tag{5.41}$$

$(B_2I)^0$ can be converted into $(B_3I)^0$ via the addition of mobile $(BI)^-$ and $(BI)^0$. The reactions are as follows:

$$(BI)^- + (B_2I)^0 \iff (B_3I)^0 + I^0 + e^-, \tag{5.42}$$

$$(BI)^0 + (B_2I)^0 \iff (B_3I)^0 + I^0. \tag{5.43}$$

The sum of corresponding reaction rates for reactions 5.42 and 5.43 are:

$$R_{(B_3I)^0} = \gamma 4\pi a_0 \frac{1}{C^*_{I^0}} \left[D^0_B + D^+_B \left(\frac{p}{n_i} \right) \right] \left[\frac{C_{(BI)^-} C_{(B_2I)^0}}{K^{eq}_{(BI)^-}} - \frac{K^{eq}_{(B_2I)^0} C_{(B_3I)^0} C_{I^0}}{K^{eq}_{(B_3I)^0} \left(\frac{p}{n_i} \right)} \right] \tag{5.44}$$

where γ is the probability factor for B_3I, defined in Eq. 5.34.

Formation of $(BI_2)^+$ involves more reaction processes because the primary reactants are mobile species I and BI. In each of them, there are two different charged states associated with it. They are I^0, I^+, $(BI)^0$ and $(BI)^-$. Hence, the reactions considered are

$$(BI)^0 + I^+ \iff (BI_2)^+ \tag{5.45}$$

$$(BI)^0 + I^0 \iff (BI_2)^+ + e^- \tag{5.46}$$

$$(BI)^- + I^+ \iff (BI_2)^+ + e^- \tag{5.47}$$

$$(BI)^- + I^0 \iff (BI_2)^+ + 2e^-. \tag{5.48}$$

The corresponding reaction rates for reactions 5.45, 5.46, 5.47, and 5.48 are

$$\begin{aligned} R_{(B_2I)^+} &= 4\pi a_0 \left(d_{(BI)^-} + d_{I^0} \right) K^{eq}{}_{(BI)^-} \left[1 + K_{I^+} \left(\frac{p}{n_i} \right) \right] \cdot \\ &\quad \left[1 + \frac{D^+_B \left(\frac{p}{n_i} \right)}{D^0_B} \right] \left[\frac{C_{(BI)^-} C_{I^0}}{K^{eq}_{(BI)^-}} - \frac{C_{(BI_2)^+} \left(\frac{n}{n_i} \right)^2}{K^{eq}_{(BI_2)^+}} \right]. \end{aligned} \tag{5.49}$$

5.2.2 Comparison to Experimental Data

Mokhberi *et al.* [116] reported the experimental data of boron activation from Hall measurement. In these experiments, boron with a dose of $2 \times 10^{14} \text{cm}^{-2}$ was implanted at 40keV. The samples were then either furnace annealed for 30 minutes or rapid thermal annealed for 1, 10, and 300 seconds at temperatures ranging from 500° to 1000°C. Another thermal anneal at 450°C for 30 minutes was performed in order to form Al contacts for Hall measurement. Using the BICs model discussed in Section 5.2.1 and the RKPM-DFA for the {311} defects from Section 5.1, we compared our simulation results the experimental data from Mokhberi *et al.* [116] in Fig. 5.13. A good agreement has been reached after two periods of thermal annealing. In the 600 to 700°C regime, the active dose decreases with

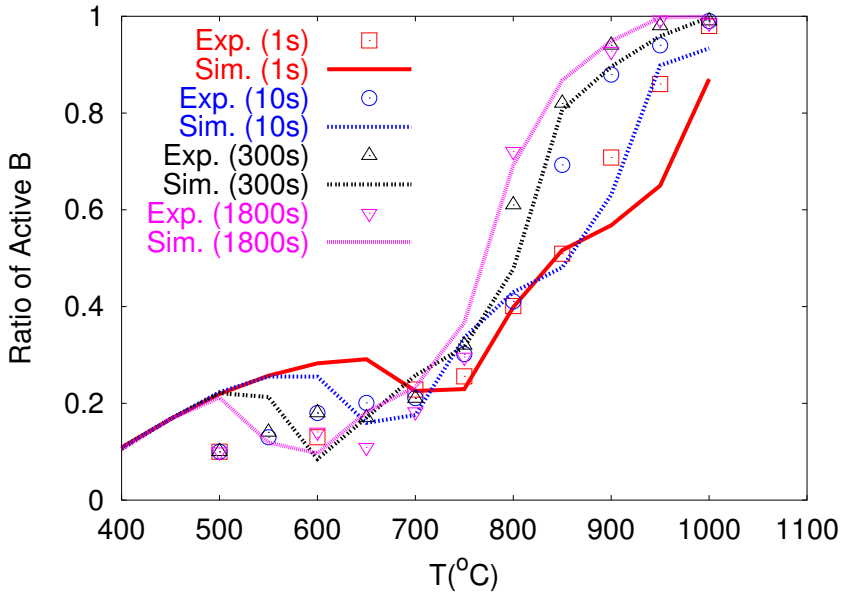

Figure 5.13: A comparison of boron activation between the experimental data (points) [116] and the simulation results (lines) at various temperature for 1, 10 , 300, and 1800 seconds. Note that second furnace annealing is performed for the purpose of good Al contacts.

time, which is referred as *the reverse annealing regime*. The active dose then increases with time at temperature above 750°C. Figs. 5.14 [a]-[d] were generated to further understand the kinetics of different BICs at different times. The dominant species is B_2I in the low temperature regime, while B_3I clusters are stable in the higher temperature regime. The high boron activation at temperatures above 900 °C is due to the dissolution of B_3I clusters. Fig. 5.15 shows the schematic of the three regions during annealing with the B activation curve after 30 minutes of furnace annealing.

This BIC model along with the point-defect clustering model accurately captures the kinetics of boron activation/deactivation for a wide range of times and temperatures. High B activation can be achieved by the higher annealing temperature and longer annealing time.

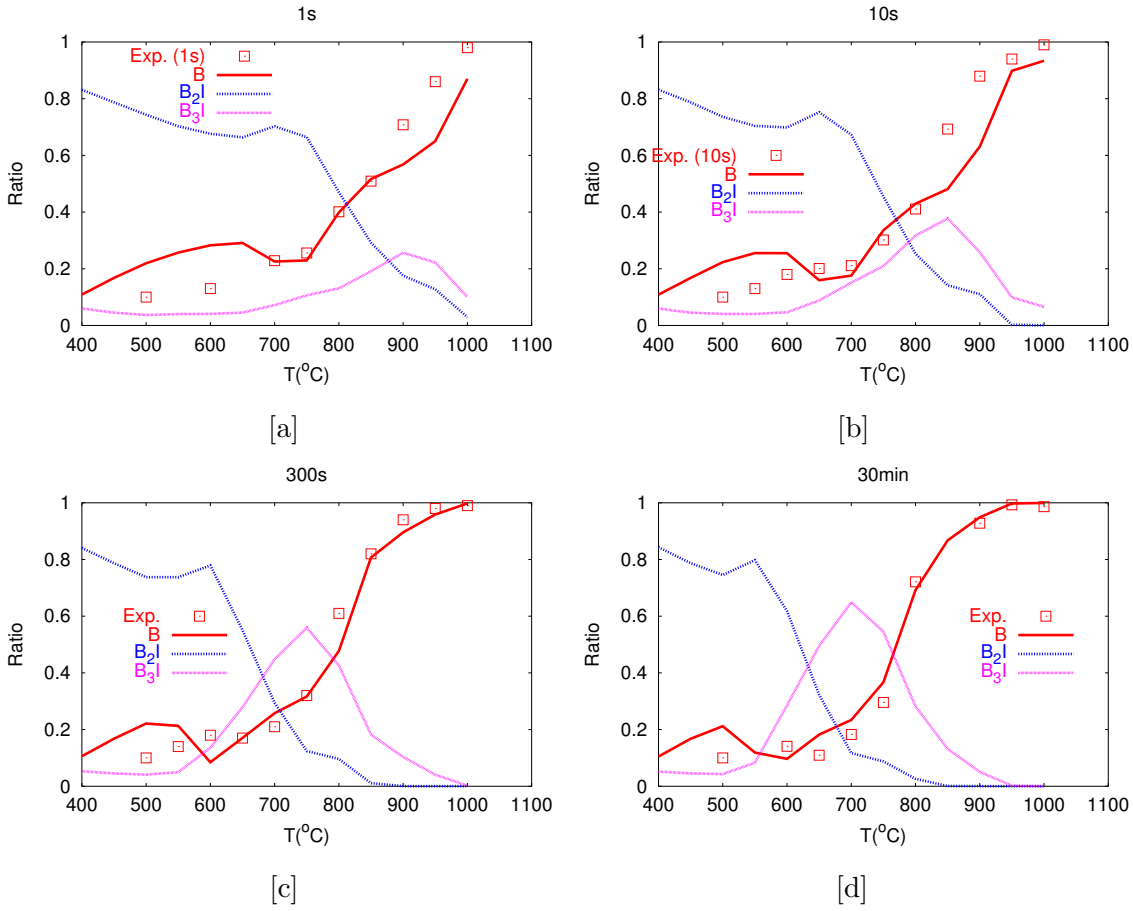

Figure 5.14: Simulation results for the ratios of B, B_2I, and B_3I versus annealing temperature at different time periods. B_2I is the dominant BIC at lower temperatures, and B_3I is the stable BIC at the mid-level temperatures. The dissolution of B_3I at temperatures above 900°C provides the source of higher boron activation.

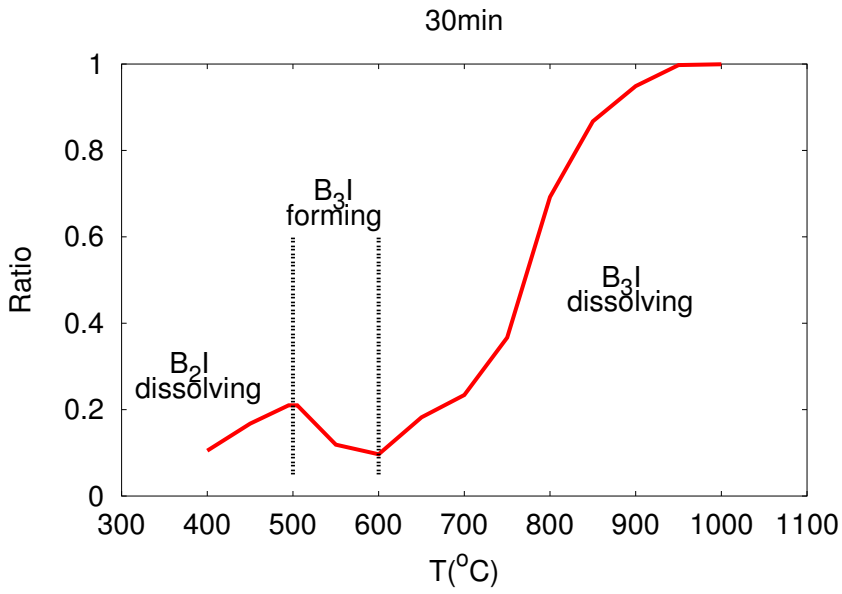

Figure 5.15: A schematic of the three regions occurring during boron activation. The curve in the plot represents the B activation after 30 minutes of furnace annealing. At temperatures below 500°C, the dominant species B_2I is dissolving, thus increasing the active fraction of boron. At moderate temperatures between 500 and 600°C, B_3I clusters are stable and forming, while B_2I is still dissolving, which explains the valley shape for boron activation. At temperatures above 600°C, the B_3I clusters dissolve, which increases the active fraction as a function of temperature. Note that the boundaries of the regions depend on the annealing time.

5.3 Summary

We were able to describe the transient enhanced diffusion (TED) and activation/deactivation for B through the formation of {311} defects, vacancy clusters and BICs using an alternative moment-based model (RKPM-DFA), which possesses excellent computational efficiency and does not require table lookups. This model has been successfully calibrated to give good agreement with the annealing of {311} defects following ion implantation. We also used *ab-initio* calculations to study stress effects on point defect clustering. By including results from first principle calculations into the kinetic precipitation model, predictions show that stress effects play an important role in point defect clustering and dopant activation.

Chapter 6

C DIFFUSION/CLUSTERING MODELS

Carbon co-implantation can reduce or eliminate B transient enhanced diffusion (TED) [119], and several experiments have shown that C provides a highly efficient sink for excess interstitials during annealing [117, 123, 143]. Napolitani *et al.* [117] found no detrimental effects on B electrical activation with the incorporation of C, when a C-rich silicon layer was placed between the damaged region and the implanted B profile. These results have a significant impact on the formation of USJ in the development of CMOS technology. As strain engineering, which can enhance free carrier mobility, is becoming more widely used in current CMOS technology, the behavior of dopant diffusion and activation under stressed conditions requires a thorough understanding. In the 90nm technology node [150], SiGe was successfully introduced to replace the material in source and drain regions of the P-MOSFET, which generates a compressive stress in the channel region and enhances hole mobility. With a similar approach, SiC alloy has the potential to replace S/D material for the N-MOSFET to generate a tensile stress in the channel region and enhance electron mobility. However, this approach requires a more detailed understanding of C diffusion, clustering, and precipitation.

In this chapter, we present our *ab-initio* calculations for different carbon complex configurations and confirm the diffusion path of carbon interstitial with the findings from Capaz *et al.* [12]. Using "kinetic lattice Monte Carlo" (KLMC) simulations, we predict the impact of stress on carbon diffusion. We also investigated the formation of small carbon/interstitial clusters and silicon-carbide precipitates. Based on the understanding gained from the analysis described above, continuum models were implemented and characterized with reported data from the literature.

6.1 C Diffusion

Carbon is most stable as a substitutional impurity (C_s) in the neutral charge state. However, carbon interstitials (CI) can be generated through kick-out or Frank-Turnbull mechanisms [34, 141, 157].

$$C_s + I \Longleftrightarrow CI \qquad \text{(KO)} \tag{6.1}$$

$$CI + V \Longleftrightarrow C_s \qquad \text{(FT)} \tag{6.2}$$

Experimental results [141, 157] and a theoretical study [12] suggested the $\langle 100 \rangle$ split

Table 6.1: Formation energies of various CI complexes relative to substitutional C and bulk Si.

	split $\langle 100 \rangle$	split $\langle 110 \rangle$	hex	tet
E_f (eV)	1.97	2.96	3.11	4.22

carbon interstitial as the ground-state of CI configuration. Our DFT calculations of formation energies of carbon interstitials in different configurations confirmed the $\langle 100 \rangle$ split as the most stable CI structure (see Table 6.1).

$$E_f^{\mathrm{CI}} = E_{\mathrm{Si_{64}C}} - E_{\mathrm{Si_{63}C}} - \frac{1}{64} E_{\mathrm{Si_{64}}} \tag{6.3}$$

In this configuration, the C and Si atoms share a single lattice site displaced along a $\langle 100 \rangle$ direction. For all the VASP calculations in this chapter, a 64-atom supercell with an energy cutoff of 340 eV and a 2^3 Monkhorst $\vec{k}$-point sampling method with generalized gradient approximation (GGA) were used.

Capaz *et al.* [12] identified the migration path for an interstitial carbon with an energy barrier of 0.51 eV in silicon by first principle calculations. Using a 65-atom supercell, Zhu [167] confirmed that the intermediate configuration is 0.5 eV higher in energy than the C interstitial ($\langle 100 \rangle$ split). The nudged elastic band (NEB) method [60, 61, 84] was used in our calculations to find the migration path for a carbon interstitial. Fig. 6.1 shows the migration path with an energy barrier (E_m) of 0.53 eV, which is comparable to the results

from both Capaz *et al.* [12] (0.51 eV) and Zhu [167] (0.5 eV). The initial state is [100] split, while the final state at the neighbor has the [001] split orientation. For C_s to diffuse, the CI ($\langle 100 \rangle$ split) first needs to be formed and overcome the transition barrier (E_m) by passing through a transition state (CI_{trans}). The structure of this transition state is shown in Fig. 6.1 (middle of top row). In this migration process, the Si atom remains in its original lattice site while the C atom moves to the neighbor site with a different orientation. Thus, the CI diffusion does not affect Si self-diffusion. Note that a CI reorientation is also completed after each migration step.

Eq. 5.19 shows the general form of the formation energy change related to a stress state. The existence of induced strains is due to the difference in equilibrium lattice constant from the pure Si system. Table 6.2 lists the induced strains for various carbon complexes. The induced strain for a substitutional carbon ($\Delta\epsilon^{C_s}$) can be easily extracted from the energy vs. hydrostatic strain plot (see Fig. 6.2) because of its high symmetry, while the induced strain for other complexes also requires an analysis of energy vs. uniaxial and/or biaxial strain (detailed analyses can be referred to Diebel [28]). The system with a C_s reduces the lattice constant by 0.41 % in comparison to Si, while the system with a CI_{split} shows the opposite behavior (a 0.14 % increase in lattice constant). This indicates that the C_s equilibrium concentration ($C^*_{C_s}$) increases in the presence of compressive strain, whereas the CI_{split} equilibrium concentration ($C^*_{CI_{split}}$) decreases. Tensile strain will have the reverse effect: increasing $C^*_{CI_{split}}$ and decreasing $C^*_{C_s}$.

Based on the harmonic transition state theory (hTST) [49], the transition rate can be

Table 6.2: Induced strains for carbon complexes.

	C_s	$CI_{split}\langle 100 \rangle$	CI_{trans}	$C_2I\langle 100 \rangle$
$\Delta\vec{\epsilon}$	-0.41	(-0.23, -0.23, 0.90)	(0.30, -0.46, 0.30)	(-0.49, -0.49, 0.64)

written as

$$\Gamma_i(\vec{\epsilon}) = \Gamma_0 \exp\left[-\frac{E^i_m(\vec{\epsilon})}{kT}\right] = \Gamma_0 \exp\left[-\frac{E^i_m(0) + \Delta E^i_m(\vec{\epsilon})}{kT}\right], \tag{6.4}$$

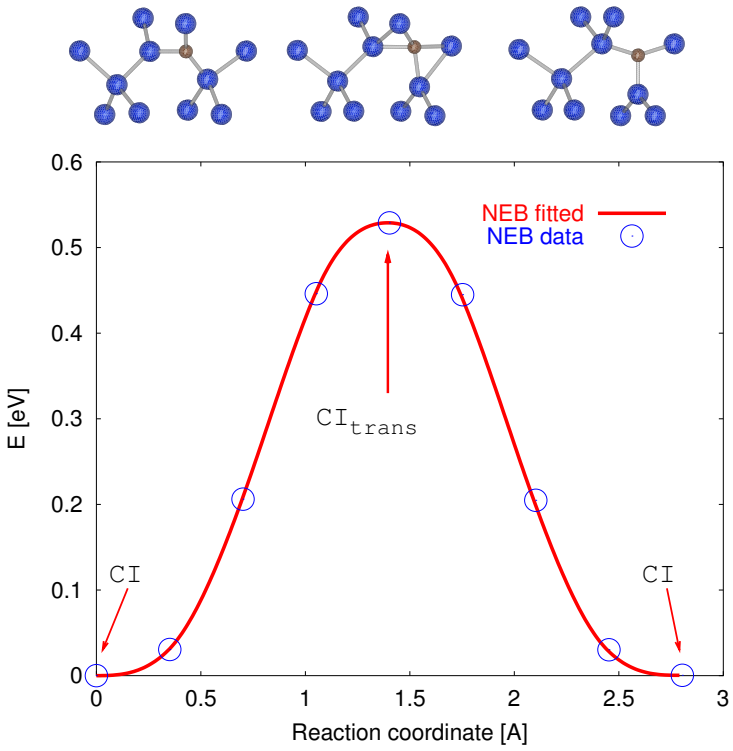

Figure 6.1: $CI_{split}[100] \rightarrow CI_{trans} \rightarrow CI_{split}[001]$ transition calculated using the NEB method [84, 60, 61] in unstrained silicon (GGA Si equilibrium lattice parameter $b_0 = 5.4566$ Å). The structure for the transition state is shown in the middle of the top row. Blue and brown atoms are silicon and carbon respectively. The migration barrier (≈ 0.53 eV), the difference of formation energies between CI_{trans} and CI_{split} ($E_f^{CI_{trans}} - E_f^{CI_{split}}$), is shown in the bottom figure. Notice that the migration barrier depends on the strain condition.

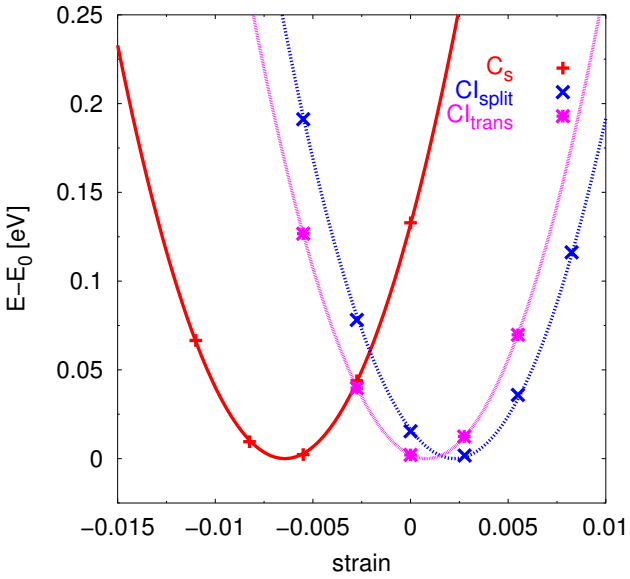

Figure 6.2: Energy vs. hydrostatic strain. The reference energy E_0 is defined as the minimum energy as function of unit cell size at a given configuration. The graph shows the behavior of C_s, $\langle 100 \rangle$ split CI, and CI_{trans} under hydrostatic strain. Strains are reported in reference to the GGA Si equilibrium lattice parameter of 5.4566 Å.

where Γ_0 is the attempt frequency, and i represents the different possible hopping directions. Here we include the stress effect under a given strain condition ($\vec{\epsilon}$), where $E_m^i(\vec{\epsilon})$ represents the migration barrier under a given strain state. $\Delta E_m^i(0)$ is the migration barrier under stress free conditions, and $\Delta E_m^i(\vec{\epsilon})$ (Eq. 6.5) is the change in the migration barrier for a given hopping direction under a given strain condition.

$$\Delta E_m^i(\vec{\epsilon}) \quad = \quad \left[\Delta E_f^{\text{tran}}(\vec{\epsilon}) - \Delta E_f^{\text{CI}}(\vec{\epsilon})\right] \tag{6.5}$$

In the KLMC simulation, a lattice is used to define system states in a crystalline solid. Eq. 6.4 describes the transition rate for a CI ($\langle 100 \rangle$ split) to migrate from one lattice site to the next. For a given orientation and position of CI, only 4 neighboring sites are accessible via the low transition barrier (see Fig. 6.3). The hopping probabilities, $p_i(\vec{\epsilon})$, in the presence of stress in different directions are defined as

$$p_i(\vec{\epsilon}) = \frac{\Gamma_i(\vec{\epsilon})}{\sum_{j=1}^{4} \Gamma_j(\vec{\epsilon})}. \tag{6.6}$$

The diffusivity of CI (d_{CI}) and transition rate (Γ) are directly linked by considering the diffusion as a random walk process at the atomic level. To keep track of the actual physical time, the average time for each migration step can be calculated as

$$\Delta t(\vec{\epsilon}) = \frac{1}{\sum_{j=1}^{4} \Gamma_j(\vec{\epsilon})}. \tag{6.7}$$

In one dimension, the following relation holds for CI diffusivity (d_{CI}):

$$d_{\mathrm{CI}}(\vec{\epsilon}) = \frac{1}{2t(\vec{\epsilon})} \left\langle \Delta x(\vec{\epsilon})^2 \right\rangle, \tag{6.8}$$

where $\langle \Delta x^2 \rangle$ is the average of the square of the displacement in the x-direction after an N-step random walk process, and t is the physical system time, which can be calculated by summing the time for each migration process (Eq. 6.7). The prediction of the relative d_{CI} change under biaxial strain is shown in Fig. 6.4[a]. The detailed information to setup this KLMC simulation under biaxial stress condition using a random walk process can be found in Appendix F. In the case of biaxial strain, the stress dependence of the equilibrium CI concentration can be expressed as:

$$\frac{C^*_{\mathrm{CI}}(\vec{\epsilon})}{C^*_{\mathrm{CI}}(0)} = \frac{2}{3} \exp\left[\frac{-\Delta E_f^{\mathrm{CI(in)}}(\vec{\epsilon})}{kT}\right] + \frac{1}{3} \exp\left[\frac{-\Delta E_f^{\mathrm{CI(out)}}(\vec{\epsilon})}{kT}\right], \tag{6.9}$$

where $\Delta E_f^{\mathrm{CI(in)}}$ is the change in energy for the in-plane component of $\mathrm{CI}_{\mathrm{split}}$, whereas $\Delta E_f^{\mathrm{CI(out)}}$ is the change for out-of-plane components. With the multiplication of Eqs. 6.8 and 6.9, one can predict the effective diffusivity change ($D_{\mathrm{C}}(\vec{\epsilon})/D_{\mathrm{C}}(0)$) of C under biaxial strain, which is shown in Fig. 6.4[b]. The prediction indicates that both in-plane and out-of-plane diffusivities for C (D_{C}) are enhanced under biaxially tensile strain and reduced under biaxially compressive strain. Using the same approach, we can also predict the effective diffusivity change of C under uniaxial stress (see Fig. 6.5).

6.2 C Clustering

A possible clustering reaction to reduce the silicon interstitial concentration is the CI-C_s pairing (Eq. 6.10), which forms a stable and immobile carbon complex [147].

$$\mathrm{C_s} + \mathrm{CI} \Longleftrightarrow \mathrm{C_2I} \tag{6.10}$$

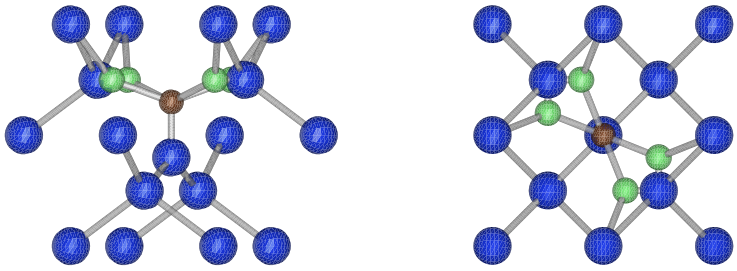

[a] [b]

Figure 6.3: An example of accessible neighbor sites. The vertically-oriented [001] split CI (brown atom) can only hop with a minimum migration energy to 4 possible neighbor sites with orientations of [100], [010], [$\bar{1}$00], and [0$\bar{1}$0] (green atoms). Left is the side view; right is the top view.

Table 6.3: Formation energies of various carbon complexes with respect to substitutional C and bulk Si.

	CI $\langle 100 \rangle$	C_2I $\langle 100 \rangle$	C_2I (A)	C_2I (B)	C_2I_2	CI_2
E_f (eV)	1.97	0.51	0.98	0.95	2.16	3.34

In equilibrium,

$$C^*_{C_2I} = 3\frac{C^2_{C_s}}{C_{Si}} \exp\left(-\frac{E_f^{C_2I}}{kT}\right), \tag{6.11}$$

where $E_f^{C_2I}$ is the formation energy for C_2I, C_{Si} is the density of lattice sites, C_{C_s} is the concentration of substitutional carbon, and the factor of 3 accounts for the 3 possible orientations on each lattice site.

Table 6.3 also shows the calculation results for formation energies of other small carbon complexes. Our calculations confirmed the results from Liu *et al.* [101], which identified the most stable C_2I configuration as a $\langle 100 \rangle$ split (dumbbell), as shown in Fig. 6.6[a]. Leary *et al.* [96] and Capaz *et al.* [13] identified two other C_2I configurations in Si. The type "**A**" configuration (see Fig. 6.6[b]) consists of a $\langle 100 \rangle$ split CI, slightly perturbed by a neighboring substitutional carbon. In the type "**B**" configuration (see Fig. 6.6[c]), a Si interstitial is

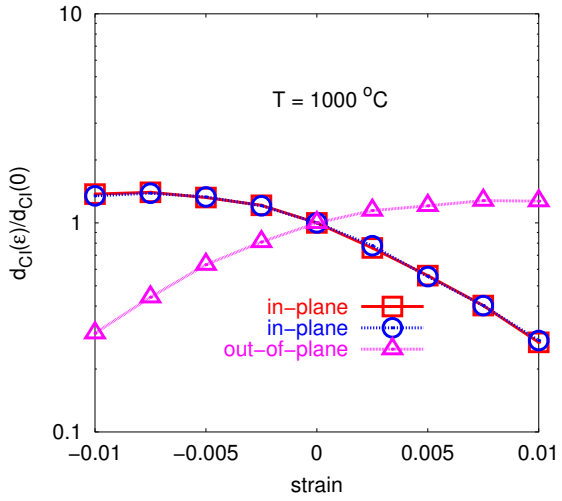

[a]

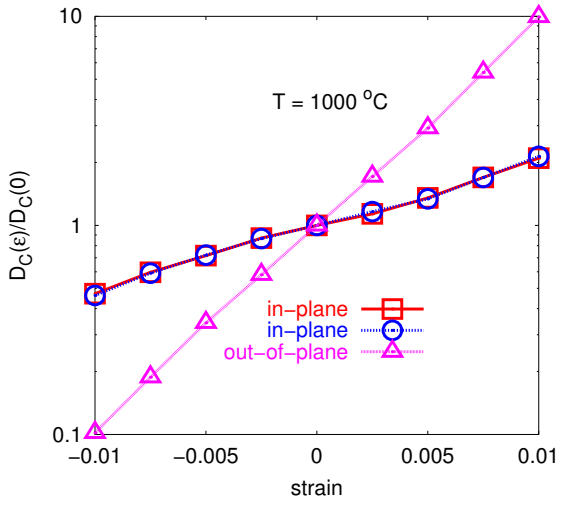

[b]

Figure 6.4: The relative change of C diffusivity ([a] d_{CI} and [b] D_{C}) under biaxial strain at 1000^{o}C determined by the KLMC analysis. [a]: CI in-plane diffusivity (d_{CI}) is reduced under tensile strain, but has a weak dependence under compressive strain. The out-of-plane diffusivity for CI shows the opposite behavior. [b]: both in-plane and out-of-plane diffusivities for C (D_{C}) are enhanced under tensile strain and reduced under compressive strain. Note that out-of-plane diffusivity for C shows a stronger dependence on the strain condition.

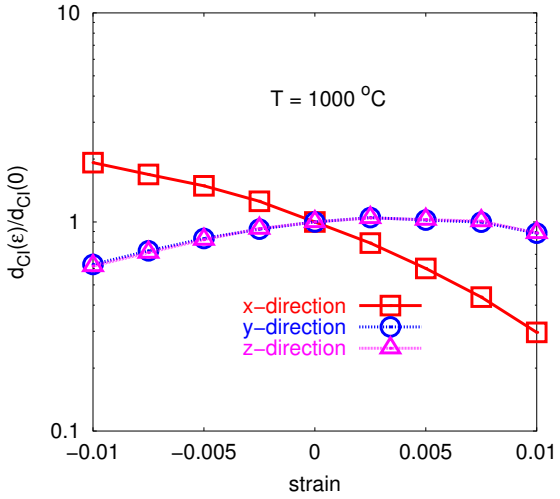

[a]

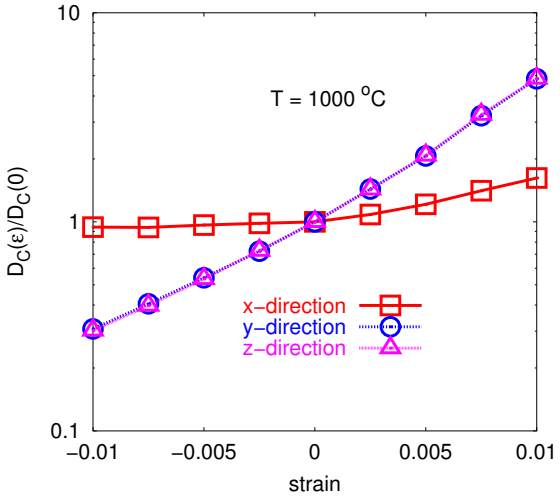

[b]

Figure 6.5: The relative change of C diffusivity ([a]: d_{CI} and [b]: D_{C}) under uniaxial strain (x-direction) at 1000^{o}C determined by the KLMC analysis. [a]: CI diffusivity (d_{CI}) in the x-direction is reduced under tensile strain but enhanced under compressive strain. The diffusivity of CI in the y- and z-directions is decreased under compressive strain, but has a weak dependence under tensile strain. [b]: the diffusivities for C (D_{C}) in the y- and z-directions are enhanced under tensile strain and reduced under compressive strain. Note that the diffusivity for C (D_{C}) in the x-direction shows a much weaker dependence on the strain condition.

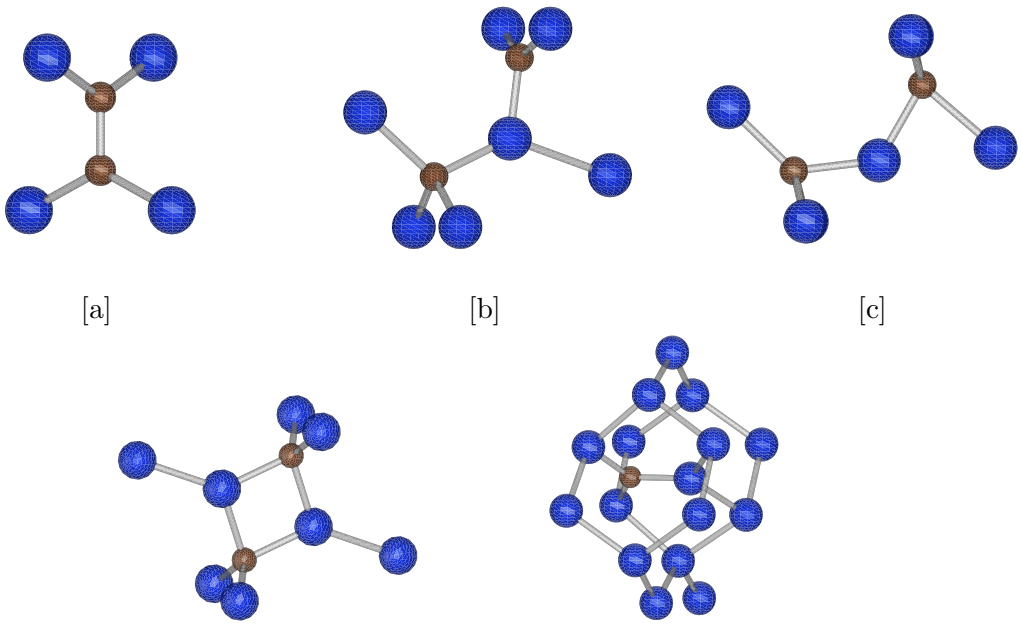

Figure 6.6: Various small carbon clusters. C_2I with different configurations are shown in the top row: [a] $\langle 100 \rangle$ split, [b] type A, and [c] type B. [d] and [e] are C_2I_2 and CI_2. Blue and brown atoms are Si and C respectively.

accommodated between two substitutional carbon atoms. Mattoni *et al.* [110] reported the type "**A**" configuration to be favored over the type "**B**" by 0.4 eV, and the formation energy for a $\langle 100 \rangle$ split CI to be 0.2 eV higher than the type "**A**" configuration. However, we found the formation energy of C_2I in $\langle 100 \rangle$ split configuration to be lower than the two Capaz structures by 0.4 eV or more, which is consistent with the results from Liu *et al.* [101]. A possible explanation for this discrepancy could be the different setup for VASP calculations. Mattoni *et al.* [110] used a much lower cutoff energy (160eV), which might not be sufficient in this application. Mattoni *et al.* [110] further suggested two other possible stable carbon complexes (C_2I_2 and CI_2), as shown in Fig. 6.6[d] and [e]. We also performed calculations to obtain their formation energies (see Table 6.3).

Note that the formation energies for all C complexes in Table 6.3 are positive, which implies that in the absence of a strong interstitial supersaturation, the concentrations of all

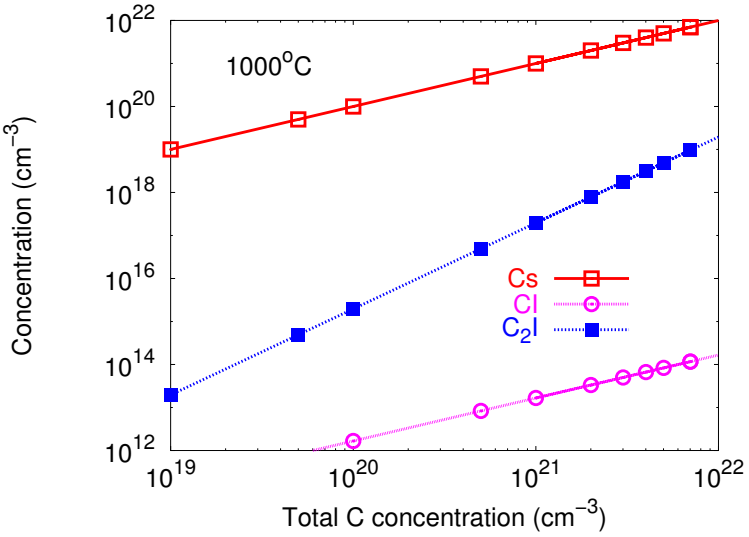

Figure 6.7: The local equilibrium concentrations of C_s, CI and C_2I as a function of total C concentration at 1000°C at $C_I/C_I^* = 1$.

these complexes are expected to be well below that of the substitutional carbon, C_s. The equilibrium concentration of C_nI_m can be defined as

$$C^*_{C_nI_m} \approx \theta_{C_nI_m} C_{Si} \left(\frac{C_{C_s}}{C_{Si}}\right)^n \left(\frac{C_I}{C_{Si}}\right)^m \exp\left(-\frac{E_f^{C_{C_nI_m}}}{kT}\right), \tag{6.12}$$

where $E_f^{C_{C_nI_m}}$ is the formation energy for $C_{C_nI_m}$, C_{Si} is the silicon lattice site density ($\approx 5\times10^{22}\text{cm}^{-3}$), and $\theta_{C_nI_m}$ is the number of possible cluster configurations per lattice site. Considering only three species (C_s, CI, and C_2I), the total carbon concentration, C_C^{tot}, can be written as Eq. 6.13, which is a function of C_{C_s}, E_f, and the interstitial concentration. Fig. 6.7 illustrates the result at 1000°C at $C_I/C_I^* = 1$, which suggests that the cluster concentrations are much lower than C_{C_s}. This indicates that C clustering is only significant in the presence of a large interstitial supersaturation.

$$C_C^{tot}(C_{C_s}) = C_{C_s} + C_{CI} + 2C_{C_2I} \tag{6.13}$$

6.3 SiC *Precipitation*

The formation of cubic SiC precipitates (β-SiC) can reduce the total energy in a SiC alloy system. The structure of β-SiC is shown in Fig. 6.8. In the presence of SiC precipitates, carbon solubility has an Arrhenius dependence and can be expressed as (neglecting differences in formation entropy)

$$C_{ss}^{\mathrm{C}} \sim C_{\mathrm{Si}} \exp\left(\frac{\Delta E_f^{\mathrm{SiC}}}{kT}\right), \tag{6.14}$$

where

$$\Delta E_f^{\mathrm{SiC}} = \frac{1}{32} E_{\mathrm{Si_{32}C_{32}}} - E_{\mathrm{Si_{63}C_s}} + \frac{31}{32} E_{\mathrm{Si_{64}}} = -2.0\mathrm{eV}. \tag{6.15}$$

$E_{\mathrm{Si_{32}C_{32}}}$, $E_{\mathrm{Si_{64}}}$, and $E_{\mathrm{Si_{63}C_s}}$ are the energies from VASP calculations with a 64-atom supercell. The comparison of carbon solubility between the experimental data and our calculated result is shown in Fig. 6.9. The calculated energy (-2.0 eV) in Eq. 6.15 is close to the reported value (-2.3 eV) from the literature [7].

In a simple analysis, assuming the precipitate has a spherical shape, the radius of a precipitate of size n can be derived from Eq. 6.16.

$$\frac{4}{3}\pi r_n^3 = n\Omega_{\mathrm{SiC}} \tag{6.16}$$

Ω_{SiC} is the atomic volume for a β-SiC. Our DFT calculations suggests the relaxed cubic lattice constant of β-SiC to be 4.3750 Å, which is much smaller than the 5.4566 Å value for silicon. The free energy for β-SiC precipitate with size n can be expressed as

$$\begin{aligned} \Delta G_{\mathrm{C}_n\mathrm{I}_n} &= -nkT \ln\left(\frac{C_{\mathrm{C}}}{C_{ss}^{\mathrm{C}}}\frac{C_{\mathrm{I}}}{C_{\mathrm{I}}^*}\right) + 4\pi r_n^2 \sigma \\ &= -nkT \ln\left(\frac{C_{\mathrm{C}}}{C_{ss}^{\mathrm{C}}}\frac{C_{\mathrm{I}}}{C_{\mathrm{I}}^*}\right) + 4\pi\sigma\left(\frac{3n\Omega_{\mathrm{SiC}}}{4\pi}\right)^{2/3}, \end{aligned} \tag{6.17}$$

where σ represents the associated interface energy per unit area (2000-8000 erg/cm^2 [148]), and C_{ss}^{C} is the carbon solubility from Eq. 6.14. The equilibrium concentration ($C_{\mathrm{C}_n\mathrm{I}_n}^*$) can then be written as

$$C_{\mathrm{C}_n\mathrm{I}_n}^* = C_{\mathrm{Si}}\left(\frac{C_{\mathrm{C}}}{C_{ss}^{\mathrm{C}}}\right)^n \left(\frac{C_{\mathrm{I}}}{C_{\mathrm{I}}^*}\right)^n \exp\left[-\frac{(4\pi)^{1/3}\sigma\,(3n\Omega_{\mathrm{SiC}}4\pi)^{2/3}}{kT}\right]. \tag{6.18}$$

$C_{\mathrm{C}_n\mathrm{I}_n}^*$ under various interstitial supersaturations using $\sigma = 8000$ erg/cm^2 is shown in Fig. 6.10. Because of the incoherent interface between silicon and β-SiC, a high surface

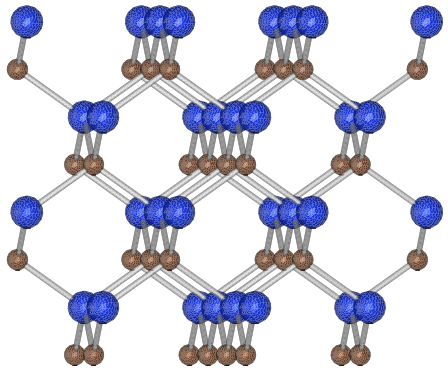

Figure 6.8: The structure of β-SiC. Si and C atoms are in blue and brown colors, respectively. Note that the lattice constant of this stable β-SiC (4.3750 Å) is much smaller than the silicon lattice constant (5.4566 Å).

energy leads to a large nucleation barrier and limits SiC precipitation. Thus, the nucleation of β-SiC precipitates is only expected in the presence of a high interstitial supersaturation.

6.4 Continuum Models

It has been demonstrated that the incorporation of a high C concentration enhances vacancy-assisted dopant diffusion (Sb, As) [95], while it retards interstitial-assisted dopant diffusion (B, P) [128, 129]. Our DFT calculations indicate no significance of pairing and clustering in modeling the dopant diffusion in a system with grown-in C. In these continuum models, we included both kick-out (Eq. 6.1) and Frank-Turnbull (Eq. 6.2) mechanisms to form CI. In the case of a high C concentration, mobile CI can diffuse out and pair with other substitutional carbon atoms. This clustering reaction reduces the silicon interstitial concentration via the formation of stable C_2I [147] (Eq. 6.10). The reactions of Eqs. 6.1, 6.2, and 6.10 deplete interstitials in the C-rich region, which is a consequence of the "chemical-pump effect". The corresponding rate equations for the reactions of Eqs. 6.1, 6.2, and 6.10 are

$$R_{\mathrm{C}_s/\mathrm{I}} = 4\pi a d_{\mathrm{CI}} \left(C_{\mathrm{C}_s} C_{\mathrm{I}} - C_{\mathrm{CI}} C^*_{\mathrm{C}_s/\mathrm{I}} \right) \tag{6.19}$$

$$R_{\mathrm{CI/V}} = 4\pi a (d_{\mathrm{CI}} + d_{\mathrm{V}}) \left(C_{\mathrm{CI}} C_{\mathrm{V}} - C_{\mathrm{C}_s} C^*_{\mathrm{CI/V}} \right) \tag{6.20}$$

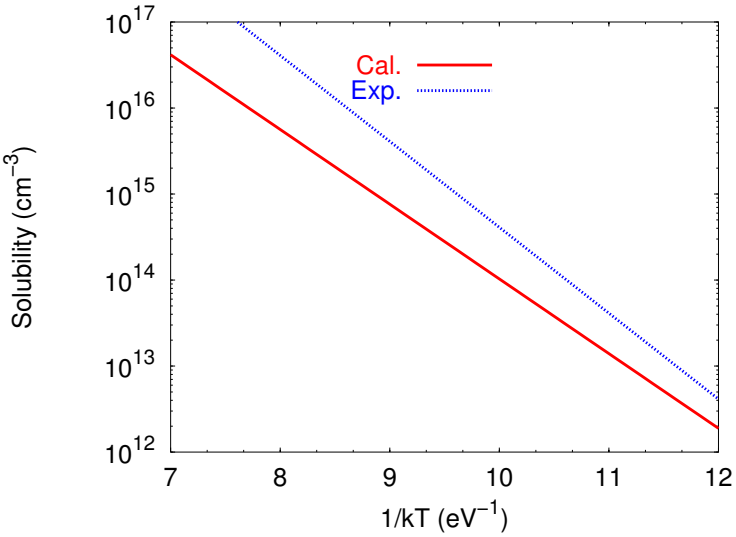

Figure 6.9: A comparison of experimental C solubility [7] to prediction from calculations (Eq. 6.14).

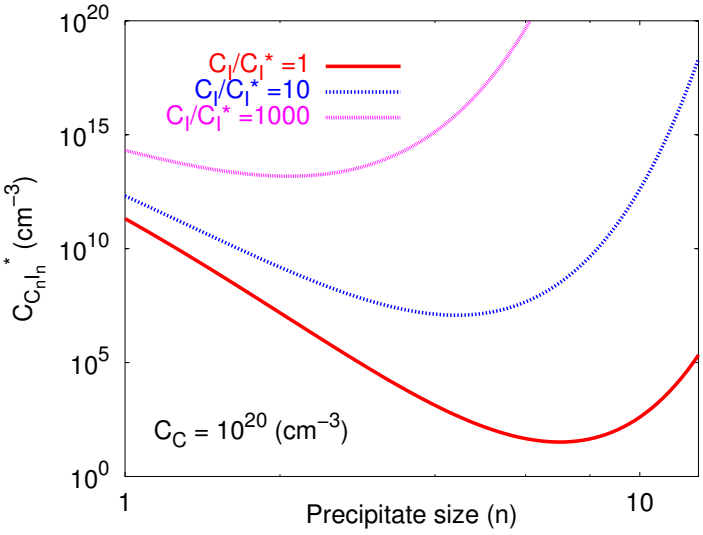

Figure 6.10: The equilibrium concentrations of C_nI_n at 1000°C under different interstitial supersaturations. To obtain SiC precipitation, interstitial supersaturation is necessary in order to overcome the nucleation barrier.

$$R_{\mathrm{C}_s/\mathrm{CI}} = 4\pi a d_{\mathrm{CI}} \left(C_{\mathrm{C}_s} C_{\mathrm{CI}} - C_{\mathrm{C_2I}} C^*_{\mathrm{C}_s/\mathrm{CI}} \right) \quad (6.21)$$

where d_x is the diffusivity for species x, a ($\sim$ 5 Å) is the effective reaction distance, and C^*s are the equilibrium constants for each reaction respectively. All the parameters are listed in Table 6.4. Note that $C^*_{\mathrm{C}_s/\mathrm{CI}}$ is taken from our *ab-initio* calculation, while the other parameters were extrapolated and derived from the literature.

All these models were implemented in FLOOPS-ISE [75]. In the following sections,

Table 6.4: Physical parameters used in this work.

Parameters	Prefactor	E_m, E_f(eV)	Reference
D_{I}	8.10×10^1 cm^2/s	0.90	[48]
C_{I^*}	9.16×10^{22} cm^{-3}	3.78	[48, 152]
D_{V}	1.00×10^{-4} cm^2/s	0.43	[48]
C_{V^*}	3.17×10^{28} cm^{-3}	4.43	[48, 152]
D_{C}	6.11 cm^2/s	3.29	[34, 118]
d_{CI}	4.40 cm^2/s	0.88	[44]
$C^*_{\mathrm{C}_s/\mathrm{I}}$	6.60×10^{21} cm^{-3}	-1.37	[34, 44, 48, 118, 152]
$C^*_{\mathrm{CI/V}}$	5.00×10^{22} cm^{-3}	-6.84	[34, 44, 48, 118, 152]
$C^*_{\mathrm{C}_s/\mathrm{CI}}$	4.40×10^{29} cm^{-3}	-1.46	DFT

we study the effects of high carbon concentrations on point defect concentrations and the resulting dopant diffusion via both interstitial (B) and vacancy (Sb) mechanisms.

6.4.1 B Diffusion in the Presence of C

Rücker *et al.* [129] observed B diffusion in the presence of C. In these experiments, the MBE-grown structure consisted of several delta B layers and a highly C-doped region. After annealing at 900°C for 45 min in an N_2 atmosphere, the SIMS profiles showed the reduction of B diffusion within the C-rich region. Our models exhibit good agreement between the experimental data and simulation results (see Fig. 6.11 [top]). In the C-rich

region, Si interstitials combine with carbon atoms and form CI and C_2I, which depletes the I concentration in the C-rich region (see Fig. 6.11 [bottom]). Boron atoms, which primarily diffuse via an interstitial mechanism, therefore diffuse much slower in the C-rich region because of the depletion of Si interstitials.

6.4.2 Sb Diffusion in the Presence of C

In the experiments performed by Lavëant *et al.* [95], enhanced Sb-diffusion was observed in the presence of a high C concentration. An MBE-grown Sb-box (200 nm thick) close to a highly C-doped region was annealed at 900°C for 3 and 6 h in an Ar environment. The SIMS profiles after 6 h annealing is shown in Fig. 6.12 [top]. Our models give an excellent agreement between the experimental data and simulation results. We also performed simulations which only included the kick-out mechanism (Eq. 6.1). However, this simple model underestimates the V supersaturation and results in less Sb diffusion.

Boundary conditions for the point defect generation/recombination in simulations are critical. In the experiments from Rücker *et al.* [129], a fast point defect generation/recombination was used as is standard for the Si/SiO_2 interface. In the case of Sb diffusion, the top surface was bare Si exposed to an Ar/vacuum environment, and generation/recombination at the top surface was modified with a much slower rate in order to match the experimental data from Lavëant *et al.* [95].

6.5 Summary

We have confirmed the migration path for C diffusion, which is consistent with the findings from Capaz *et al.* [12] and Zhu [167]. The results from first-principles calculations were used to obtain induced strains in order to describe the stress effects on C diffusion. Through KLMC simulations, we found that tensile stress enhances C diffusion under both uniaxial and biaxial strain, while compressive stress has the opposite impact. Carbon/interstitial clustering was investigated, and the *ab-initio* calculations suggested that these clustering reactions are only possible under a sufficient interstitial supersaturation. Despite the low C solubility in silicon, silicon carbide precipitates do not form readily in the absence of I

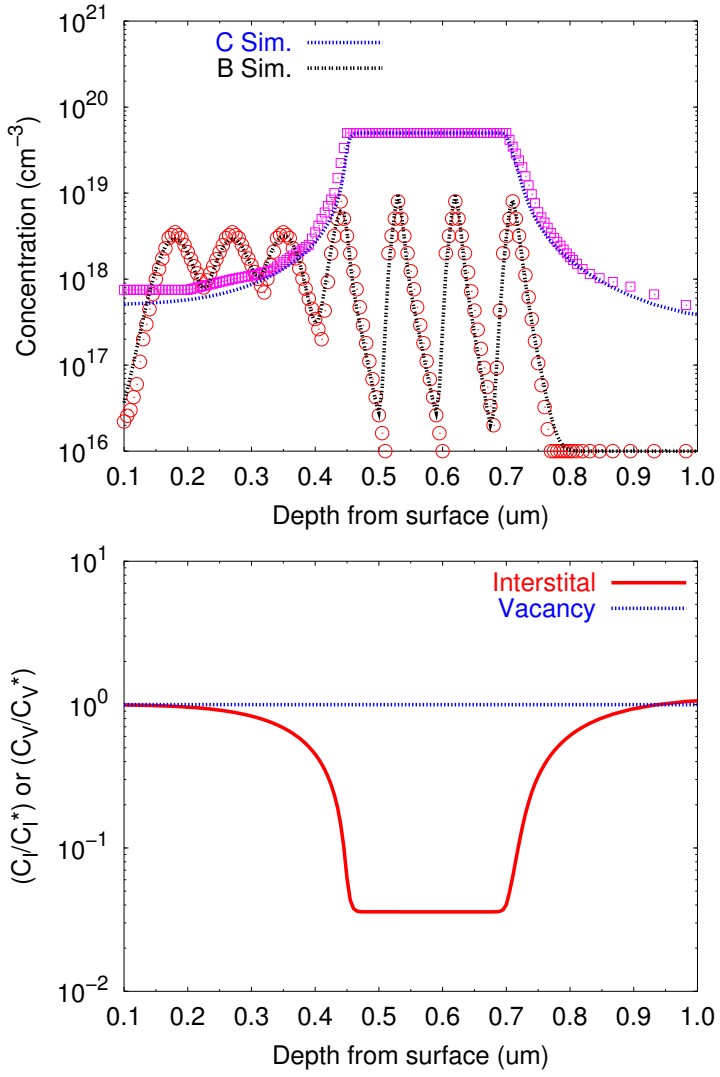

Figure 6.11: The diffusion of B and C marker layers after 45 min annealing at 900°C [129]. In the top plot, points are the SIMS profiles and lines are the simulation results. Corresponding point defect concentrations are shown in the bottom plot. An undersaturation of I is predicted within the C-rich region.

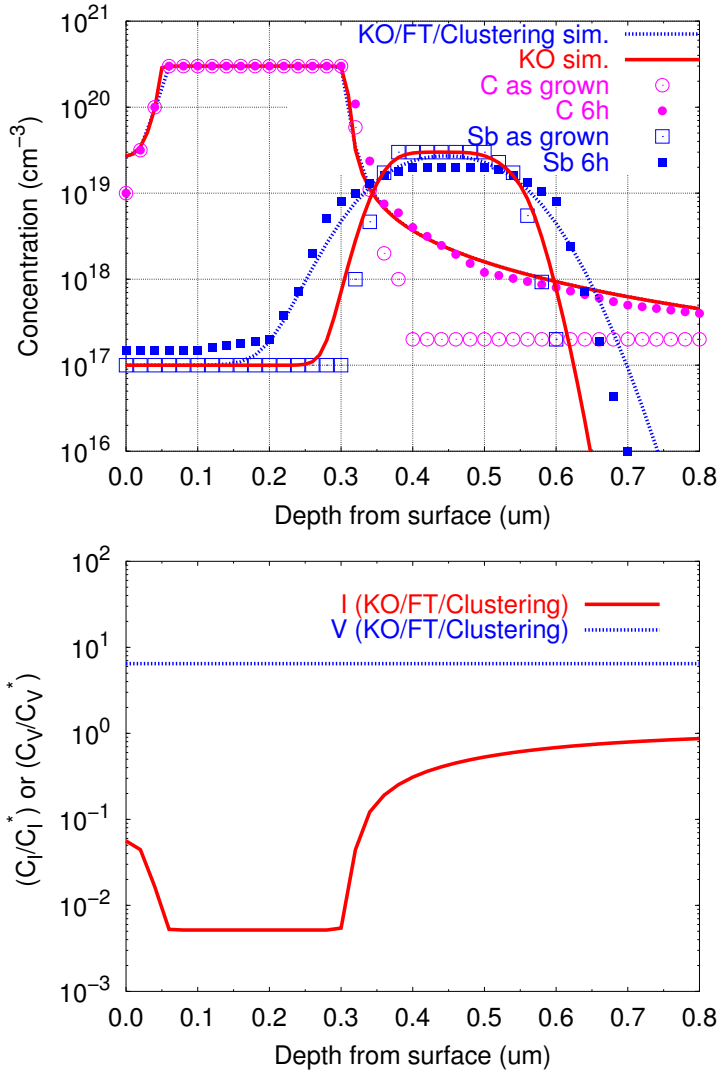

Figure 6.12: A comparison between the experimental data [95] and our simulation results. In the [top] plot, empty and solid points are the SIMS profiles before and after annealing. Lines are the simulation results. Corresponding point defect concentrations are shown in the [bottom] plot. An undersaturation of I is predicted within the C-rich region, while a supersaturation of vacancies enhances the Sb diffusion.

supersaturation. The incoherent interface has a high surface energy and leads to a nucleation barrier, which prevents the formation of silicon carbide.

We have also implemented continuum models for dopant (B, Sb) diffusion with the incorporation of C diffusion/clustering. These models predict suppressed B diffusion with the incorporation of a high C-doped region, consistent with the experimental data [129]. In a similar way, the enhancement of Sb diffusion is predicted in the presence of a high C-doped region and a good agreement was shown in comparison to the experimental results [95]. With the incorporation of models for excess point defect evolutions and boron-interstitial clustering (BICs) under stress conditions from Chapter 5, these models together can provide an insight into the ultra-shallow-junction formation process for future devices.

Chapter 7

SUMMARY AND FUTURE WORK

In this thesis, we described new methods for modeling of diffusion and precipitation processes and applied them to gettering processes and the formation of ultra shallow junctions. Results from *ab-initio* and KLMC calculations were used in the development of continuum models. This chapter gives brief summaries of the main contributions in this dissertation, and closes with suggestions for future work and a final conclusion.

7.1 Precipitation Models

In Chapter 3, we first discussed the *full kinetic precipitation model* (FKPM) [31, 40], which considers the evolution of a full size distribution. The *reduced moment-based model* (RKPM) [19] enhances the computing efficiency of the FKPM by tracking the time evolution of moments of the size distribution. In this work, we introduced the delta-function approximation (DFA) which both simplifies the implementation of RKPM and also provides parameters with clearer physical meaning. The resulting RKPM-DFA features improved computing efficiency, while accurately replicating the behavior of FKPM and previous RKPM.

7.2 Main Contributions of Gettering Study

(1) Developed continuum models to describe Cu out-diffusion and precipitation processes.

(2) Applied the RKPM-DFA for point defects to investigate Fe gettering technique via ion implantation.

In Chapter 4, we studied the mechanism of Cu out-diffusion, following our previous work [55]. A possible explanation for the unusual behavior of Cu out-diffusion due to the surface con-

ditions was proposed and validated by comparison to experimental results. By assuming Fermi level pinning at the wafer surface, we were able to modify the surface potential change under different surface treatments and thereby provide a quantitative understanding of Cu segregation and precipitation at the surface.

Using the RKPM-DFA to describe the evolution of point defects, we also studied Fe gettering via ion implantation. The capture of iron atoms by gettering sites was described and characterized by the experimental data. The results from both experiments and simulation indicated the high sensitivity of gettering capacity in the $R_p/2$ damage zone to the Si^+ ion implantation dose and annealing conditions.

7.3 Main Contributions of Study in the Formation of USJ

(1) Applied RKPM-DFA to describe the evolution of point defects (I and V), and {311} defects, which control transient enhanced diffusion (TED).

(2) Developed continuum models to describe dopant/defect clustering, which limits dopant activation.

(3) Predicted the effects of stress on TED using the results from *ab-initio* calculations.

(4) Explained C diffusion and clustering behavior using *ab-initio* calculations, and implemented the continuum models for dopant diffusion with the incorporation of C.

(5) Predicted the effects of stress on C diffusion and clustering using both *ab-initio* calculations and KLMC.

In Chapter 5, we specifically looked at point defect clusters which control the TED (I, V clusters, 311 defects) and dopant/defect clusters which limit dopant activation (B/I clusters). The evolution of point defect clusters was described by using the RKPM-DFA, which possesses an excellent computational efficiency and does not require table lookups. This model was successfully calibrated to give a good agreement with the annealing of {311}

defects following the ion implantation. We also applied *ab-initio* calculations to study stress effects on the point defect clustering. By including results from first principle calculations into the kinetic precipitation model, predictions show that the formation of free I was favored over small IC's and {311} defects under compressive stress. Furthermore, the formation of BICs was described by the well calibrated RKPM-DFA for {311} defects. With the models above, we captured the behavior of boron activation for a wide range of times and temperatures. We concluded this chapter with predictive models for diffusion, activation kinetics and extended defect evolution as a function of stress/strain.

In Chapter 6, using first-principles calculations, we confirmed the migration path for C diffusion, and studied the effects of stress on C diffusion/clustering. Through KLMC simulations, we found that tensile stress enhances C diffusion under both uniaxial and biaxial strain, while compressive stress has the opposite impact. Our analytical results suggest that C clustering and SiC precipitation are only significant under a high interstitial supersaturation. We have also implemented continuum models for dopant (B and Sb) diffusion in the presence of C diffusion/clustering. These models correctly predict suppressed B diffusion with the incorporation of a high C-doped region. In a similar way, the enhancement of Sb diffusion was predicted in the presence of a high C-doped region.

7.4 Suggestions for Future Work

Low temperature budgets and low metal contamination levels require novel gettering processes, which involve new physical phenomena, such as non-equilibrium metal solubility. These processes are strongly affected by details of the thermal cycle as well as the surface treatments and bulk defect distributions. We suggest investigation of the observed inconsistencies between the high-temperature models and observations made at low temperatures, in order to develop predictive models for the Fe/Cu/Ni gettering during low temperature processing. These models can then be used to develop effective processes to meet future gettering needs.

We have described and implemented models of Cu outdiffusion depending on the wafer surface conditions. Further work to study Cu gettering process in a p/p+ substrate is necessary. Due to the high diffusion coefficient of copper, its distribution in a p/p+ wafer is

determined by both high temperature anneal and gettering of the residual Cu concentration during cool-down and subsequent storage at a room temperature. We suggest analyzing the existing experimental data in order to develop physically meaningful models which can accurately capture the observed experimental behavior.

Relaxation gettering techniques involve precipitation of supersaturated metals at intentionally introduced structural defects, which can be either gettering sites in the substrate (e.g., oxygen precipitates) or proximity gettering sites (e.g., introduced by ion implantation). The driving force for relaxation gettering is the supersaturation of transition metals, which can be evaluated by comparing the dissolved metal concentration with the metal solubility at the gettering temperature. We suggest the study the kinetics of establishing the equilibrium solubility of iron at intermediate and low temperatures, in order to determine its effective non-equilibrium solubility during the transition period, and use this data to theoretically analyze the efficiency of low-temperature gettering. The results can be used to develop quantitative models of gettering processes and to design optimum gettering procedures for low metal contamination levels and low temperature budgets.

In CMOS device scaling, ultra-shallow profiles with super-activated high doping levels are necessary. Preamorphization and high dose of dopant implantation can lead to dislocation generation. These dislocations occur both near the end-of-range region and at more distant sites where high stresses exist. Depending on where they form, these extended defects can affect the dopant redistribution during annealing and degrade the performance and reliability of devices. Therefore, a more thorough understanding of dislocation dynamics is required for further development of continuum models. *Ab-initio* calculations can be used to provide the energies and structures of these dislocations, but a heavy load of computations may be expected. With the results from DFT calculations, KLMC provides a framework for modeling the formation and evolution of these dislocations in the presence of strain/stress conditions. These efforts can then provide a direction for fabrication processes to achieve ultra-shallow and super-activated doping profiles.

Si:C alloys have the potential to replace the material in the S/D regions of a P-MOSFET to introduce tensile stress into the channel region, which enhances electron mobility. We have investigated the stress effects of C diffusion/cluster in a Si:C alloy system. Of partic-

ular interests are the dopant diffusion and activation in a Si:C alloy system. Dopant atoms (e.g., P, As, Sb) may have local chemical interactions with these alloys. Both strain and chemical effects can potentially introduce non-uniformity and anisotropy into the diffusion and clustering of dopants and point defects. *Ab-initio* calculations can be used to separate out the strain and chemical effects, as well as to obtain the formation and migration energies of dopants, point defects, and complexes. The resulting information then becomes the input to KLMC simulations, which predict the evolution of active dopant distributions in Si:C alloys. The extracted behavior from the KLMC simulations forms the basis for continuum models of the dopant diffusion and activation. Future work on these models will provide insight and tools required to identify optimum alloy compositions to achieve shallow abrupt junctions, high activation and low contact resistance.

7.5 Final Conclusion

We have demonstrated the capability of TCAD tools to study the diffusion and precipitation mechanisms for semiconductor processes across the modeling hierarchy (ie, ab-initio, KLMC, and continuum modeling approaches). TCAD tools are essential for identifying diffusion path/reaction mechanisms and predicting the results under conditions that are experimentally difficult to access. For the IC industry, these tools substantially reduce manufacturing costs and provide guidance for designing new technologies.

BIBLIOGRAPHY

[1] The international technology roadmap for semiconductors, 2005. http://www.itrs.net/report.html.

[2] C. Ahn. Personal discussion.

[3] M. Aoki, A. Hara, and A. Ohsawa. Fundamental properties of intrinsic gettering of iron in a silicon wafer. *J. Appl. Phys.*, 72:895, 1992.

[4] M. Aoki, T.Itakura, and N. Sasaki. Gettering of iron impurities in p/p^+ epitaxial silicon wafers with heavily boron-doped substrates. *Appl. Phys. Lett*, 66:2709, 1995.

[5] T.A. Baginski and J.R. Monkowski. The role of chlorine in the gettering of metallic impurities from silicon. *J. Electrochem. Soc.*, 132:2031, 1985.

[6] L. Baldi, G. Cerofolini, and G. Ferla. Heavy metal gettering in silicon-device processing. *J. Electrochem. Soc.*, 127:164, 1980.

[7] A.R. Bean and R.C. Newman. The solubility of carbon in pulled silicon crystals. . *Phys. Chem. Solids*, 32:1211, 1971.

[8] J.L. Benton, K. Halliburton, S. Libertino, D.J. Eaglesham, and S. Coffa. Electrical signatures and thermal stability of interstitial clusters in ion implanted si. *J. Appl. Phys.*, 84:4749, 1998.

[9] J.L. Benton, P.A. Stolk, D.J. Eaglesham, D.C. Jacobson, J.-Y. Cheng, J.M. Poate, N.T. Ha, T.E. Haynes, and S.M. Myers. Iron gettering mechanisms in silicon. *J. Appl. Phys.*, 80:3275, 1996.

[10] A. Bongiorno, L. Colombo, and T.Diaz De la Rubia. Structural and binding properties of vacancy clusters in silicon. *Europhys. Lett.*, 43:695, 1998.

[11] T.M. Buck, K.A. Pickar, J.M. Poate, and C-M. Hsieh. Gettering rates of various fast-diffusing metal impurities at ion-damaged layers on silicon. *Appl. Phys. Lett*, 21:485, 1972.

[12] R.B. Capaz, A. Dal Pino, and J.D. Joannopoulos. Identification of the migration path of interstitial carbon in silicon. *Phys. Rev. B*, 50:7439, 1994.

[13] R.B. Capaz, A. Dal Pino, and J.D. Joannopoulos. Theory of carbon-carbon pairs in silicon. *Phys. Rev. B*, 58(15):9845–9850, 1998.

[14] M.S. Carroll, J.C. Sturm, and T. Buyuklimanli. Quantitative measurement of the surface silicon interstitial boundary condition and silicon interstitial injection into silicon during oxidation. *Phys. Rev. B*, 64:085316, 2001.

[15] M.J. Caturla, M.D. Johnson, and T.D. de la Rubia. The fraction of substitutional boron in silicon during ion implantation and thermal annealing. *Appl. Phys. Lett.*, 72:2736, 1998.

[16] F. Cembali, M. Seevidori, E. Landi, and S. Solmi. Influence of damage depth profile on the characteristics of shallow p+/n implanted junctions. *Phys. Stat. Sol. (a)*, 94:315, 1986.

[17] S. Chakravarthi. *Physics and Modeling of Ion Implantation Induced Transient Enhanced Deactivation and Diffusion Processes In Boron Doped Silicon.* PhD thesis, Boston University, MA, 2005.

[18] S. Chakravarthi and S.T. Dunham. A simple continuum model for boron clustering based on atomistic calculations. *J. Appl. Phys.*, 89:3650, 2001.

[19] I. Clejan and S.T. Dunham. A reduced moment-based model for precipictation kinetics and application to dopant activation in silicon. *J. Appl. Phys.*, 78:7327, 1995.

[20] C.F. Clement and M.H. Wood. Moment and fokker-planck equations for the growth and decay of small objects. *Pro. R. Soc. Lond A*, 371:553, 1980.

[21] C.B. Collins and R.O. Carlson. Properties of silicon doped with iron or copper. *Phys. Rev.*, 108:1409, 1957.

[22] N.E.B. Cowern, A. Caccito, J.S. Custer, F.W. Saris, and W. Vandenvorst. Roles of c and b clusters in transient diffusion of b in silicon. *Appl. Phys. Lett*, 68:1150, 1996.

[23] N.E.B. Cowern, H.F.F. Jos, and K.T.F. Janssen. Role of point defects in the transient diffusion and clustering of implanted boron in silicon. *Mater. Sci. Eng. B*, 4:101, 1989.

[24] N.E.B. Cowern, G. Mannino, P.A. Stolk, F. Roozeboom, J.G.M. van Barkum, F. Cristiano, A. Claverie, , and M. Jaraiz. Transient diffusion of ion-implanted b in si: Dose, time, and matrix dependence of atomic and electrical profiles. *J. Appl. Phys.*, 68:6191, 1990.

[25] N.E.B. Cowern, G.F.A. van de Walle, P.C. Zalm, and D.W.E. Vandenhoudt. Mechanisms of implant damage annealing and trasient enhanced diffusion in si. *Appl. Phys. Lett*, 65:2981, 1994.

[26] S.W. Crowder, P.B. Griffin, and J.D. Plummer. Nitridation enhanced diffusion of antimony in bulk and silicon-on-insulator material. In *Proceedings of the Fourth International Symposium on Process Physics and Modeling in Semiconductor Technology*, page 54, 1996.

[27] L. Demeio and B. Shizgal. Time dependent nucleation. ii. a semiclassical approach. *J. Chem. Phys.*, 98(7):5713, 1993.

[28] M. Diebel. *Application of Ab-initio Calculations to Modeling of Nanoscale Diffusion and Activation in Silicon*. PhD thesis, University of Washington, WA, 2004.

[29] S.T. Dunham. A quantitative model for the coupled diffusion of phosphorus and point defects in silicon. *J. Electrochem. Soc.*, 139:2628, 1992.

[30] S.T. Dunham. Growth kinetics of disc-shaped extended defects with constant thickness. *Appl. Phys. Lett.*, 63:464, 1993.

[31] S.T. Dunham. Modeling of the kinetics of dopant precipitation in silicon. *J. Electrochem. Soc.*, 142:2823, 1995.

[32] D.J. Eaglesham, P.A. Stolk, H.-J. Gossmann, T.E. Haynes, and J.M. Poate. Implant damage and transient enhanced diffusion in si. *Nucl. Instrum. Methods. Phys. Res. Sect. B*, 106:191, 1995.

[33] D.J. Eaglesham, P.A. Stolk, H.-J. Gossmann, and J.M. Poate. Implantation and transient b diffusion in si: The source of the interstitials. *Appl. Phys. Lett.*, 65:2305, 1994.

[34] N.A. Stolwijk F. Rollert and H. Mehrer. Diffusion of carbon-14 in silicon. *Mater. Sci. Forum*, 38-41:753, 1989.

[35] P.M. Fahey, P.B. Griffin, and J.D. Plummer. Point defects and dopant diffusion in silicon. *Rev. Mod. Phys.*, 61:289, 1989.

[36] C. Flink, H. Feick, S.A. McHugo, W. Seifert, H. Hieslmair, T. Heiser, A.A. Istratov, and E.R. Weber. Out-diffusion and precipitation of copper in silicon: An electrostatic model. *Phys. Rev. Lett.*, 85:4900, 2000.

[37] F.C. Frank and D. Turnbull. Mechanism of diffusion of copper in germanium. *Phys. Rev*, 104:617, 1956.

[38] U. Gösele, F. Morehead, W. Frank, and A. Seeger. Diffusion of gold in silicon: A new model. *Appl. Phys. Lett.*, 38:1981, 157.

[39] U. Gösele and H. Strunk. High-temperature diffusion of phosphorus and boron in silicon via vacancies or via self-interstitials? *Appl. Phys. A*, 20:265, 1979.

[40] A.H. Gencer. *Modeling and Simulation of Transient Enhanced Diffusion Based on Interactions of Point and Extended Defects.* PhD thesis, Boston University, MA, 1999.

[41] A.H. Gencer. User's guide and reference manual for dopdees, 1999.

[42] A.H. Gencer and S.T. Dunham. A predictive model for transient enhanced diffusion based on evolution of 311 defects. *J. Appl. Phys.*, 238:152, 1997.

[43] A.H. Gencer and S.T. Dunham. A combined model for {311} defect and dislocation loop evolution: Analytical formulation of kinetic precipitation model. *J. Appl. Phys.*, 91:2883, 2002.

[44] U. Gősele. In *Oxygen Carbon, Hydrogen and Nitrogen in Silicon*, volume 59 of *Mater Res Soc Symp Proc*, page 419, Pittsburgh, Pa., 1986. Materials Research Society.

[45] D. Gilles, W. Bergholz, and W.Schröter. Diffusion of manganese in silicon studied by deep-level transient spectroscopy and tracer measurements. *J. Appl. Phys.*, 59:3590, 1986.

[46] D. Gilles, E.R. Weber, and S.Hahn. Mechanism of internal gettering of interstitial impurities in czochralski-grown silicon. *Phys. Rev. B*, 64:196, 1990.

[47] D. Gilles, W.Schröter, and W. Bergholz. Impact of the electronic structure on the solubility and diffusion of 3d transition elements in silicon. *Phys. Rev. B*, 41:5770, 1990.

[48] G.H. Gilmer, T. Diaz de la Rubia, D.M. Stock, and H. Jaraiz. Diffusion and interactions of point defects in silicon: Molecular dynamics simulations. *Nucl. Instrum Methods B*, 102:247, 1995.

[49] M.E. Glicksman. *Diffusion in Solids: Field Theory, Solid-state Principles, and Applications.* John Wiley, 2000.

[50] M. Gordon. Cramming more components onto integrated circuits. *Electron.*, 38:114, 1965.

[51] M. Gordon. Progress in digital integrated electronics. *IEDM Tech. Dig.*, page 11, 1975.

[52] M. Gordon, 2003.

[53] K. Graff. In H.R. Huff, T. Abe, and B. Kolbesen, editors, *Semiconductor Silicon 1986*, page 175, Pennington, NJ, 1986. Electrochem. Soc.

[54] K. Graff. *Metal Impurities in Silicon-Device Fabrication*. Springer-Verlag, Berlin ; New York, 1995.

[55] H. Guo and S.T. Dunham. Accurate modeling of copper precipitation kinetics including fermi level dependence. *Appl. Phys. Lett*, 89:182106, 2006.

[56] H.-W Guo, S.T. Dunham, C-L. Shih, and C. Ahn. Modeling of defect evolution and ted under stress based on dft calculations. In *Proceedings of IEEE 2006 International Conference on Simulation of Semiconductor Processes and Devices*, page 71. SISPAD, 2006.

[57] R.N. Hall and J.H. Racette. Diffusion and solubility of copper in extrinsic and intrinsic germanium, silicon, and gallium arsenide. *J. Appl. Phys.*, 35:379, 1964.

[58] F.S. Ham. Diffusion-limited growth of precipitate particles. *J. Appl. Phys.*, 30:1518, 1959.

[59] T.E. Haynes, D.J. Eaglesham, P.A. Stolk, H.-J. Gossmann, D.C. Jacobson, and J.M. Poate. Interactions of ion-implantation-induced interstitials with boron at high concentrations in silicon. *Appl. Phys. Lett.*, 69:1376, 1996.

[60] G. Henkelman and H Jőnsson. Improved tangent estimate in the nudged elastic band method for finding minimum energy paths and saddle points. *J. Chem. Phys.*, 113:9978, 2000.

[61] G. Henkelman, B.P. Uberuaga, and H Jónsson. A climbing image nudged elastic band method for finding saddle points and minimum energy paths. *J. Chem. Phys.*, 113:9901, 2000.

[62] G. Henkleman, B. Uberuaga, S.T. Dunham, and H. Jönsson. Simulations of dopant clustering in silicon: Dimer calculations using dft forces. In *Technical Proceedings of the 2002 International Conference on Computational Nanoscience and Nanotechnology*, page 144. ICCN, 2002.

[63] H. Hieslmair, A.A. Istratov, S.A. McHugo, C.Flink, T. Heiser, and E.R.Weber. Gettering of iron by oxygen precipitates. *Appl. Phys. Lett*, 72:1460, 1998.

[64] H. Hieslmair, S.A. McHugo, A.A Istratov, and E.R Weber. *Gettering*. Robert Hull, London, 1999.

[65] S. Hocine and D. Mathiot. In *Proceedings of the 15th International Conference on Defects in Semiconductors*, volume 38-41 of *Materials science forum*, page 1, Aefermannsdorf, Switzerland, 1989. Trans. Tech. Defects in semiconductors 15.

[66] S. Hocine and D. Mathiot. In *Proceedings of the 15th International Conference on Defects in Semiconductors*, volume 38-41 of *Materials science forum*, page 725, Aefermannsdorf, Switzerland, 1989. Trans. Tech. Defects in semiconductors 15.

[67] S. Hocine and D. Mathiot. In *Proceedings of the 15th International Conference on Defects in Semiconductors*, volume 38-41 of *Materials science forum*, page 729, Aefermannsdorf, Switzerland, 1989. Trans. Tech. Defects in semiconductors 15.

[68] W.K. Hofker, H.W. Werner, D.P. Oosthoek, and N.J. Koeman. Redistribution effects associated with sequential implantations. *Appl. Phys. Lett.*, 4:125, 1974.

[69] K. Honda, A. Ohsawa, and T. Nakanishi. Behavior of fe impurity during hcl oxidation. *J. Electrochem. Soc.*, 142:3486, 1995.

[70] H.J Hrostowski and R.H. Kaiser. Infrared absorption of oxygen in silicon. *Phys. Rev.*, 107:966, 1957.

[71] S.M. Hu. Formation of stacking faults and enhanced diffusion in the oxidation of silicon. *J. Appl. Phys.*, 45:1567, 1974.

[72] K. Huang. *Statistical Mechanics*. John Wiley & Sons, New York, 1963.

[73] H.R Huff. Chemical impurities and structural imperfections in semiconductor silicon. ii. *Solid State Technol.*, 26:211, 1983.

[74] A. Ihlal, R. Rizk, and O.B.M. Hardouin Duparc. Correlation between the gettering efficiencies and the energies of interfaces in silicon bicrystals. *J. Appl. Phys.*, 80:2665, 1996.

[75] ISE. Floops-ise, 2004.

[76] S. Isomae, T. Ishiba, T. Ando, and M. Tamura. Annealing behavior of mev implanted carbon in silicon. *J. Appl. Phys.*, 74:3815, 1993.

[77] A.A. Istratov, C. Flink, H. Hieslmair, S.A. Mchugo, and E.R. Weber. Diffusion, solubility, and gettering of copper in silicon. *Mater. Sci. Eng. B*, 72:99, 2000.

[78] A.A. Istratov, C. Flink, H. Hieslmair, and E.R. Weber. Intrinsic diffusion coeffeicient of interstitial copper in silicon. *Phys. Rev. Lett.*, 81:1243, 1998.

[79] A.A Istratov, H. Hieslmair, and E.R Weber. Iron and its complexes in silicon. *Appl. Phys. A*, 69:13, 1999.

[80] A.A Istratov, H. Hieslmair, and E.R Weber. Iron contamination in silicon technology. *Appl. Phys. A*, 70:489, 2000.

[81] M. Jacob, P. Pichler, H. Ryssel, R. Falster, M. Cornara, D. Gambaro, M. Olmo, and M. Pagani. Observation of vacancy enhancement during rapid thermal annealing in nitrogen. *Sol. St. Phen.*, 57-58:349, 1997.

[82] M. Jaraiz, G.H. Gilmer, J.M. Poate, and T.D. De la Rubia. Atomistic calculations of ion implantation in si: Point defect and transient enhanced diffusion phenomena. *Appl. Phys. Lett.*, 68:409, 1996.

[83] N. Jeng and S.T. Dunham. Interstitial supersaturation during oxidation of silicon in steam ambients. *J. Appl. Phys.*, 72:2049, 1992.

[84] H. Jőnsson, G. Mills, and K.W. Jacobsen. *Classical and Quantum Dynamics in Condensed Phase Simulations*. World Scientific, Singapore, 1998.

[85] J.S. Kang and D.K. Schroder. Gettering in silicon. *J. Appl. Phys.*, 65:2974, 1989.

[86] R. Kögler, J.R. Kaschny, R.A. Yankov, P. Werner, A.B. Danilin, and W. Skorupa. Metal gettering by defective regions in carbon-implanted silicon. *Sol. St. Phen.*, 57-58:63, 1997.

[87] J. Kim, F. Kirchhoff, J.W. Wilkins, and F.S. Khan. Stability of si-interstitial defects: from point to extended defects. *Phys. Rev. Let.*, 84:503, 2000.

[88] J. Kim and J.W. Wilkins. Extended si {311} defects. *Phys. Rev. B*, 55:16186, 1996.

[89] L.C. Kimerling and J.L. Benton. Electronically controlled reactions of interstitial iron in silicon. *Physica B & C*, v 116 B&C:297, 1983.

[90] O. Kononchuk, R.A. Brown, Z. Radzimski, G.A. Rozgonyi, and F. Gonzalez. Gettering of fe to below 10^10cm^{-3} in mev self-implanted czochralski and float zone silicon. *Appl. Phys. Lett*, 69:4203, 1996.

[91] O.V. Kononchuk, R.A. Brown, S.V. Koveshnikov, K.L. Beaman, F. Gonzalez, and G.A. Rozgonyi. Metallic impurity gettering in mev implanted si. *Sol. St. Phen.*, 57-58:69, 1997.

[92] S.V. Koveshnikov and G.A. Rozgonyi. Mechanism of iron gettering in mev si ion implanted epitaxial silicon. *J. Appl. Phys.*, 84(6):3078, 1998.

[93] G. Kresse and J. Hafner. Norm-conserving and ultrasoft pseudopotentials for first-row and transition elements. *J. Phys. Condens. Matter*, 6:8245, 1994.

[94] G. Kresse and J. Hafner. Efficient iterative schemes for *ab initio* total-energy calculations using a plane-wave basis set. *Phys. Rev. B.*, 54:11169, 1996.

[95] P. Lavéant, P. Werner, N. Engler, and U. Gősele. Engineering the diffusion behavior of dopants (b, sb) in silicon by incorporation of carbon. *Nucl. Instrum Methods B*, 186:292, 2002.

[96] P. Leary, R. Jones, S. Öberg, and V. J. B. Torres. Dynamic properties of interstitial carbon and carbon-carbon pair defects in silicon. *Phys. Rev. B*, 55(4):2188–2194, 1997.

[97] T. Lenosky, S. Theiss, and T.D. de la Rubia. Personal discussion.

[98] T.J. Lenosky, B. Sadigh, S.K. Theiss, M.-J. Caturla, and T.D. de la Rubia. Ab initio energetics of boron-interstitial clusters in crystalline si. *Appl. Phys. Lett.*, 77:1834, 2000.

[99] A.D. Lilak, S.K. Earles, M.E. Law, and K.S. Jones. Evolution of {311} type defects in boron-doped structures: Experimental evidence of boron-interstitial cluster formation. *Appl. Phys. Lett.*, 74:2038, 1999.

[100] K.P. Lisiak and A.G. Milnes. Platinum as a lifetime-control deep impurity in silicon. *J. Appl. Phys.*, 46:5229, 1975.

[101] C.-L. Liu, W. Windl, L. Borucki, S. Lu, and X.-Y. Liu. Ab *initio* modeling and experimental study of c-b interactions in si. *Appl. Phys. Lett.*, 80:52, 2002.

[102] X.-Y. Liu, W. Windl, and M.P. Masquelier. Ab initio modeling of boron clustering in silicon. *Appl. Phys. Lett.*, 77:2018, 2000.

[103] G.W. Ludwig and H.H. Woodbury. In *Proc of the Int Conf on Defects in Semicond (Prague, 1960)*, volume 38-41, page 596, 1960.

[104] C. MaCarthy, M. Miyazaki, H. Horie, S. Okamoto, and H.Tsuya. In H.R. Huff, H. Tsuya, and U. Gösele, editors, *Semiconductor Silicon/1998*, page 692, Pennington, NJ, 1998. Electrochem. Soc.

[105] G. Mannino, N.E.B. Cowern, F. Roozeboom, and J.G.M. van Berkum. Roles of self- and boron-interstitial clusters in transient enhanced diffusion in silicon. *Appl. Phys. Lett.*, 76:855, 2000.

[106] G. Mannino, V. Privitera, S. Solmi, and N.E.B. Cowern. Issues on boron eletrical activation in silicon: Experiments on boron clusters and shallow junctions formation. *Nucl. Instrum. Methods. Phys. Res. Sect. B*, 186:246, 2002.

[107] G. Mannino, S. Solmi, V. Privitera, and M. Bersani. Electrical activation of b in the presence of boron-interstitials clusters. *Appl. Phys. Lett.*, 79:3764, 2001.

[108] D. Mathiot and J.C. Pfister. Influence of the nonequilibrium vacancies on the diffusion of phosphorus into silicon. *J. Appl. Phys.*, 53:3053, 1982.

[109] D. Mathiot and J.C. Pfister. Dopant diffusion in silicon: a consistent view involving nonequilibrium defects. *J. Appl. Phys.*, 55:3518, 1984.

[110] A. Mattoni, F. Bernardini, and L. Colombo. Self-interstitial trapping by carbon complexes in crystalline silicon. *Phys. Rev. B*, 66(19):195214, 2002.

[111] H.J. Mayer, H.Mehrer, and K. Maier. *Radiation Effects in Semiconductors 1976*, volume 31. Inst. of Physics, Bristol, London, 1977.

[112] S.A. McHugo, E.R.Weber, M. Mizuno, and F.G. Kirscht. A study of gettering efficiency and stability in czochralski silicon. *Appl. Phys. Lett*, 66:2840, 1994.

[113] S.A. McHugo, H. Hieslmair, and E.R. Weber. Gettering of metallic impurities in photovoltaic silicon. *Appl. Phys. A*, 64:127, 1997.

[114] E.J. Mets. Poisoning and gettering effects in silicon junctions. *Electrochem. Soc. – J*, 112:420, 1965.

[115] H. Meyer. Modeling of transient enhanced diffusion and simulation of boron activation and deactivation in silicon. Master's thesis, University of Washington, WA, 2002.

[116] A. Mokhberi, P.B. Briffin, and J.D. Plummer. Kinetics of boron activation. page 163. 2000 International Conference on Simulation Semiconductor Processes and Devices, 2000.

[117] E. Napolitani, D. De Salvador A. Coati, A. Carnera, S. Mirabella, S. Scalese, and F. Priolo. Complete suppression of the transient enhanced diffusion of b implanted in preamorphized si by interstitial trapping in a spatially separated c-rich layer. *Appl. Phys. Lett.*, 79:4145, 2001.

[118] R.C. Newamn and J. Wakefield. The diffusivity of carbon in silicon. *J. Phys. Chem. Solids*, 19:230, 1961.

[119] S. Nishikawa, A. Tanaka, and T. Yamaji. Reduction of transient boron diffusion in preamorphized si by carbon implantation. *Appl. Phys. Lett.*, 60:2270, 1992.

[120] Y. Ohkubo, K. Matsumoto, and K. Nagai. Acceleration of cu surface precipitation from bulk by adsorbed organic molecules. *Jpn. J. Appl. Phys.*, 44:3793, 2005.

[121] A. Ohsawa, K. Honda, and N. Toyokura. Metal impurities near the sio_2-si interface. *J. Electrochem. Soc.*, 131:2964, 1984.

[122] J. Partanen, T. Tuomi, M. Tilli, S. Hahn, C-C.D Wong, and A. Ponce. Thin film backside gettering in n-type (100) czochralski silicon during simulated cmos process cycles. *J. Mater. Res.*, 4:623, 1989.

[123] B.J. Pawlak, T. Janssens, B. Brijs, W. Vandervorst, E. J.H. Collart, S.B. Felch, and N.E.B. Cowern. Effect of amorphization and carbon co-doping on activation and diffusion of boron in silicon. *Appl. Phys. Lett.*, 89:062110, 2006.

[124] L. Pelaz, G.H. Gilmer, H.-J. Gossmann, C.S. Rafferty, M. Jaraiz, and J. Barbolla. B cluster formation and dissolution in si: A scenario based on atomistic modeling. *Appl. Phys. Lett.*, 74:3657, 1999.

[125] L. Pelaz, M. Jaraiz, G.H. Gilmer, H.-J. Gossmann, C.S. Rafferty, and D.J. Eaglesham. B diffusion and clustering in ion implanted si: The role of b cluster precursors. *Appl. Phys. Lett.*, 70:2285, 1997.

[126] J.D. Plummer, M.D. Deal, and P.B. Griffin. *Silicon VLSI Technology: Fundamentals, Practice, and Modeling.* Prentice Hall, Upper Saddle River, NJ, 2000.

[127] C.L Reed and K.M Mar. Effects of abrasion gettering on silicon material with swirl defects. *J. Electrochem. Soc.*, 127:2058, 1980.

[128] H. Rűcker, B. Heinemann, and R. Kurps. Nonequilibrium point defects and dopant diffusion in carbon-rich silicon. *Phys. Rev. B*, 64:073202, 2001.

[129] H. Rűcker, B. Heinemann, W. Rőpke, R. Kurps, D. Krűger, G. Lipper, and H.J. Osten. Suppressed diffusion of boron and carbon in carbon-rich silicon. *Appl. Phys. Lett.*, 73:1682, 1998.

[130] K. Rim, J.L. Hoyt, and J.F Gibbons. Fabrication and analysis of deep submicron strained-si n-mosfet's. *IEEE Trans. Electron Devices*, 47:1406, 2000.

[131] D.J. Roth, R.Y.S Huang, J.D. Plummer, and R.W. Dutton. Silicon interstitial absorption during thermal oxidation at 900 degrees c by extended defects formed via silicon implantation. *Appl. Phys. Lett.*, 62:2498, 1993.

[132] M.B Shabani, S. Okuuchi, and Y. Shimanuki. In B.O. Kolbesen, C. Claeys, P. Stallhofer, F. Tardif, J.L. Benton, P. Rai-Choudhury, T.J. Shaffner, D. K. Shroder, and M. Tajima, editors, *Analytical and diagnostic techniques for semiconductor materials, devices and processes*, page 510, Pennington, NJ, 1999. Electrochem. Soc.

[133] G.G. Shahidi. Soi technology for the ghz era. *IBM J. Res. Dev.*, 46:121–, 2002.

[134] B. Shen, T. Sekiguchi, J. Jablonski, and K. Sumino. Gettering of copper by bulk stacking faults and punched-out dislocations in czochralski-grown silicon. *J. Appl. Phys.*, 76:4540, 1994.

[135] C.-L. Shih. *Low Thermal Budget Silicon Processing*. PhD thesis, University of Washington, WA, 2005.

[136] W. Shockley. The path to the conception of the junction transistor. *IEEE Trans. Electron Devices*, 23:597, 1976.

[137] W. Shockley and J.T. Last. Statistics of the charge distribution for a localized flaw in a semiconductor. *Phys. Rev.*, 107:392, 1957.

[138] W. Shockley and W. T. Read. Statistics of the recombinations of holes and electrons. *Phys. Rev.*, 87:835, 1952.

[139] D. Skarlatos, M. Omri, A. Claverie, and D. Tsoukalas. Estimation of the number of interstitial atoms injected in silicon during thin oxide formation. *J. Electrochem. Soc.*, 146:2276, 1999.

[140] S. Solmi, M. Bersani, M. Sbetti, J.L. Hansen, and A.N Larsen. Boron-interstitial silicon clusters and their effects on transient enhanced diffusion of boron in silicon. *J. Appl. Phys.*, 88:4547, 2000.

[141] L.W. Song and G.D. Watkins. Epr identification of the single-acceptor state of interstitial carbon in silicon. *Phys. Rev. B*, 42:5759, 1990.

[142] P.A. Stolk, J.L. Benton, D.J. Eaglesham, D.C. Jacobson, J.-Y. Cheng, J.M. Poate, S. M. Myers, and T.E. Haynes. The mechanism of iron gettering in boron-doped silicon. *Appl. Phys. Lett*, 68:51, 1996.

[143] P.A. Stolk, D.J. Eaglesham, H.-J. Gossmann, and J.M. Poate. Carbon incorporation in silicon for suppressing interstitial-enhanced boron diffusion. *Appl. Phys. Lett.*, 66:1370, 1995.

[144] P.A. Stolk, H.-J Gossmann, D.J. Eaglesham, D.C. Jacobson, H.S Luftman, and M. Poate. Understanding and controlling transient enhanced dopant diffusion in silicon. In *Proceedings of the 1994 MRS Fall Meeting*, volume 354 of *Mater Res Soc Symp Proc*, page 307, Pittsburgh, Pa., 1995. Materials Research Society.

[145] P.A. Stolk, H.-J. Gossmann, D.J. Eaglesham, D.C. Jacobson, J.M. Poate, and H.S. Luftman. Trap-limited interstitial diffusion and enhanced boron clustering in silicon. *Appl. Phys. Lett.*, 66:568, 1995.

[146] P.A. Stolk, H.-J. Gossmann, D.J. Eaglesham, D.C. Jacobson, C.S. Rafferty, H.S. Luftman, and T.E. Haynes. Physical mechanisms of transient enhanced dopand diffusion in ion-implanted silicon. *J. Appl. Phys.*, 81:6031, 1997.

[147] P.A. Stolk, H.-J. Gossmann, D.J. Eaglesham, and J.M. Poate. The effect of carbon on diffusion in silicon. *Mater. Sci. Eng. B*, 36:275, 1996.

[148] W.J. Taylor, T.Y. Tan, and U. Gősele. Carbon precipitation in silicon: Why is it so difficult? *Appl. Phys. Lett.*, 62:3336, 1993.

[149] R.D. Thompson and K. N. Tu. Low temperature gettering of cu, ag, and au across a wafer of si by al. *Appl. Phys. Lett*, 41:440, 1982.

[150] S.E Thompson, M. Armstrong andC. Auth, S. Cea, R. Chau, G. Glass, T. Hoffman, J. Klaus, Zhiyong Ma, B. Mcintyre, A. Murthy, B. Obradovic, L. Shifren, S. Sivakumar, S. Tyagi, T. Ghani, K. Mistry, M. Bohr, and Y. El-Mansy. A logic nanotechnology featuring strained-silicon. *IEEE Electron Device Lett.*, 25:191, 2004.

[151] S.E Thompson, R.S Chau, T. Ghani, K. Mistry, S. Tyagi, and M.T. Bohr. In search of forever continued transistor scaling one new material at a time. *IEEE Trans. ESemiconductor Manufacturing*, 18:26, 2005.

[152] A. Ural, P.B. Griffin, and J.D. Plummer. Self-diffusion in silicon: Similarity between the properties of native point defects. *Phys. Rev. Lett.*, 83:3454–3457, 1999.

[153] D. Vanderbilt. Soft self-consistent pseudopotentials in a generalized eigenvalue formalism. *Phys. Rev. B*, 41:7892, 1990.

[154] H. V*ä*in*ö*l*ä*, E.Saarnilehto, M. Yli-Koski, A. Haarahiltunen, J. Sinkkonen, G. Berenyi, and T. Pavelka. Quantitative copper measurement in oxidized p-type silicon wafers using microwave photoconductivity decay. *Appl. Phys. Lett.*, 87:032109, 2005.

[155] P. Wagner, H. Hage, H. Prigge, T. Prescha, and J. Weber. In H. Huff, K.G. Barraclough, and J i. Chikawa, editors, *Proceedings of the Sixth International Symposium on Silicon Materials Science and Technology: Semiconductor Silicon 1990*, page 675, Pennington, NJ, 1990. Electrochem. Soc.

[156] A.J. Walker, P.H. Woerlee, H.G. Pomp, and N.E.B. Cowern. Shallow boron junctions and preamorphization for deep submicron silicon technology. *J. Appl. Phys.*, 73:4048, 1993.

[157] G. D. Watkins and K. L. Brower. Epr observation of the isolated interstitial carbon atom in silicon. *Phys. Rev. Lett.*, 36:1329, 1976.

[158] E.R. Weber. Transition metals in silicon. *Appl. Phys. A*, 30:1, 1983.

[159] J. Welser, J.L. Hoyt, and J.F Gibbons. Electron mobility enhancement in strained-si n-type metal-oxide-semiconductor field-effect transistors. *IEEE Trans. Electron Devices*, 15:100, 1994.

[160] W. Wijaranakula. The reaction kinetics of iron-boron pair formation and dissociation in p-type silicon. *J. Electrochem. Soc.*, 140:275, 1993.

[161] W. Windl, X.-Yang Liu, and M.P. Masquelier. First-principles modeling of boron clustering in silicon. *Phys. Stat. Sol. (b)*, 226:37, 2001.

[162] S. Wolf and R.N. Tauber. *Silicon Processing for the VLSI Era*, volume 1. Lattice Press, Sunset Beach, Calif, 2000.

[163] M. Yoshida. Numerical solution of phosphorous diffusion equationin silicon. *Jpn. J. Appl. Phys.*, 18:479, 1979.

[164] M. Yoshida. Diffusion of phosphorous in silicon. *Jpn. J. Appl. Phys.*, 22:1404, 1983.

[165] L.H. Zhang, K.S. Jones, P.H. Chi, and D.S. Simon. Transient enhanced diffusion without {311} defects in low energy b^+-implanted silicon. *Appl. Phys. Lett*, 67:2025, 1995.

[166] J. Zhu. Ab initio pseudopotential calculations of dopant diffusion in si. *Comput. Mater. Sci.*, 12:309, 1998.

[167] J. Zhu. Ab initio pseudopotential calculations of dopant diffusion in si. *Comput. Mater. Sci.*, 12:309, 1998.

[168] J. Zhu, T.D. dela Rubia, L.H. Yang, C. MailhiotGeorge, and H. Gilmer. Ab initio pseudopotential calculations of b diffusion and pairing in si. *Phys. Rev. B*, 54:4741, 1996.

[169] J.F. Ziegler, J.P. Biersack, and U. Littmark. *The Stopping and Range of Ions in Matter*. Pergamon Press, New York, 2003.

Appendix A

FIVE STREAM MODEL FOR DOPANT DIFFUSION

The *five stream model* [29] describes the coupled diffusion of dopants with point defects and is also referred as pair diffusion model [29, 35, 108, 109, 163, 164]. In Section 2.2.2, we listed all reactions for point defects and dopant/defect pairing including multiple charge states, Eqs. 2.35 to 2.40. We will briefly go through the derivations done by Chakravarthi *et al.* [17] regarding the corresponding reaction rates R's and fluxes J's in Eq. 2.41

For simplification, we assumed A to be an acceptor (A^-). As mentioned in Section 2.1.1, the concentration of charged point defects can be related to the concentration of neutral defects. Another assumption is that all ionization reactions are near equilibrium, since the electronic reactions are much faster then diffusion reactions. The concentrations of point defects and dopant/defect pairs can then expressed as

$$C_{X^i} = K_{X^i} C_{X^0} (n_i/n)^i , \tag{A.1}$$

$$C_{(AX)^i} = K_{(AX)^i} C_{(AX)^-} (n_i/n)^{i+1}, \tag{A.2}$$

where K's represent equilibrium constants for the electronic exchange, and n and n_i are the local and intrinsic electron concentrations. Note that in equilibrium, $C_{(AX)^-}$, the product of the pairing between A^- and X^0, can be written as

$$C_{(AX)^-} = K_{A^-/X^0} C_A C_{X^0}, \tag{A.3}$$

where K_{A^-/X^0} is the equilibrium constant for the pairing of a neutral point defect X^0 with a substitutional atom A^-.

The total concentration of point defects in all charged states can be written as

$$C_X = \sum_i C_{X^i} = \sum_i \left[K_{X^i} \left(\frac{n_i}{n} \right)^i C_{X^0} \right] = \chi_X C_{X^0}, \tag{A.4}$$

where C_{X^0} is the concentration of neutral point defects, and χ_X is defined as

$$\chi_X = \sum_i \left[K_{X^i} \left(\frac{n_i}{n} \right)^i \right]. \tag{A.5}$$

Since electronic exchange can occur before or after pairing and equilibrium concentration is independent of path,

$$K_{\mathrm{A}^-/\mathrm{X}^0} K_{(\mathrm{AX})^{i-1}} = K_{\mathrm{X}^i} K_{\mathrm{A}^-/\mathrm{X}^i}. \tag{A.6}$$

Using Eqs. A.1, A.2, A.3, and A.6, the total concentration for dopant/defect pairs in all charged states can then be expressed as

$$C_{\mathrm{AX}} = \sum_i C_{(\mathrm{AX})^i} = \pi_{\mathrm{X}} C_{\mathrm{A}} C_{\mathrm{X}^0}, \tag{A.7}$$

where

$$\pi_{\mathrm{X}} = K_{\mathrm{A}^-/\mathrm{X}^0} + K_{\mathrm{A}^-/\mathrm{X}^+} K_{\mathrm{X}^+} \left(\frac{p}{n_i}\right) + K_{\mathrm{A}^-/\mathrm{X}^-} K_{\mathrm{X}^-} \left(\frac{n}{n_i}\right). \tag{A.8}$$

Note that interaction with doubly charged defects in these equations can also be included. Given that A is an acceptor, $K_{\mathrm{A}^-/\mathrm{X}^-}$ is expected to be small due to Coulombic repulsion.

A.1 $\vec{J_{\mathrm{AI}}}$ *and* $\vec{J_{\mathrm{AV}}}$

Due to the gradient of the distribution of ionized dopant atoms, mobile species (I, V, AI, and AV) experience the electric field. Therefore, the flux $\vec{J_{\mathrm{AC}}}$ should include both drift and diffusion components, as well as all the charged states. We will first focus on the flux for AI, ($\vec{J_{\mathrm{AI}}}$).

$$\vec{J}_{(\mathrm{AI})^i} = \vec{J}^{\mathrm{diff}}_{(\mathrm{AI})^i} + \vec{J}^{\mathrm{drift}}_{(\mathrm{AI})^i} \tag{A.9}$$

Due to the assumption that A is a an acceptor, Eq. A.9 will be expanded in terms of $(\mathrm{AI})^-$, $(\mathrm{A}^- + \mathrm{I}^0)$. Using Eq. A.2 and Fick's law, the diffusion term can be expressed as

$$\begin{aligned} \vec{J}^{\mathrm{diff}}_{(\mathrm{AI})^i} &= -d_{(\mathrm{AI})^i} \nabla C_{(\mathrm{AI})^i} \\ &= -d_{(\mathrm{AI})^i} \nabla \left[K_{(\mathrm{AI})^i} C_{(\mathrm{AI})^-} (p/n_i)^{i+1} \right]. \end{aligned} \tag{A.10}$$

Using the Einstein's relationship, ($\mu = d/kT$), the drift term becomes

$$\begin{aligned} \vec{J}^{\mathrm{drift}}_{(\mathrm{AI})^i} &= \mu_{(\mathrm{AI})^i} i q \vec{\mathcal{E}} C_{(\mathrm{AI})^i} \\ &= d_{(\mathrm{AI})^i} (q/kT) i \vec{\mathcal{E}} C_{(\mathrm{AI})^i}, \end{aligned} \tag{A.11}$$

where μ is the mobility and $\vec{\mathcal{E}}$ is the electric field vector. The electric field can be calculated from the gradient of electrostatic potential, (Eq. C.2), given by a Boltzmann distribution.

$$\begin{aligned} \vec{\mathcal{E}} &= \nabla\left[(kT/q)\ln\left(p/n_i\right)\right] \\ &= (kT/q)\left(n_i/p\right)\nabla\left(p/n_i\right) \end{aligned} \tag{A.12}$$

Substituting Eqs. A.2 and A.12 into Eq. A.11,

$$\vec{J}^{\text{drift}}_{(\text{AI})^i} = id_{(\text{AI})^i}K_{(\text{AI})^i}C_{(\text{AI})^-}\left(p/n_i\right)^i\nabla\left(p/n_i\right). \tag{A.13}$$

Adding both the diffusion (Eq. A.10) and drift terms (Eq. A.13), the following is obtained:

$$\begin{aligned} \vec{J}_{(\text{AI})^i} &= -d_{(\text{AI})^i}K_{(\text{AI})^i}\left(p/n_i\right)^{i+1}\left[\nabla C_{(AI)^-} + C_{(\text{AI})^-}\nabla\ln\left(p/n_i\right)\right] \\ &= -d_{(\text{AI})^i}K_{(\text{AI})^i}K_{\text{A}^-/\text{I}^0}\left(p/n_i\right)^{i+1}\left[\nabla\left(\frac{C_{(\text{AI})}}{\pi_{\text{I}}}\right) + \frac{C_{(\text{AI})}}{\pi_{\text{I}}}\nabla\ln\left(\frac{p}{n_i}\right)\right]. \end{aligned} \tag{A.14}$$

The macroscopic diffusivity is given by

$$D_{\text{A}} = d_{(\text{AI})}\frac{C_{(\text{AI})}}{C_{\text{A}}}. \tag{A.15}$$

Using Eq. A.15, the sum of $\vec{J}_{(\text{AI})^i}$, (Eq. A.14), over all the the charge states can be expressed as

$$\begin{aligned} \vec{J}_{(\text{AI})} &= \sum_{i=-1}^{+1}\vec{J}_{(\text{AI})^i} \\ &= -\frac{\left[D^{\text{I}^0}_{\text{A}} + D^{\text{I}^+}_{\text{A}}\left(\frac{p}{n_i}\right) + D^{\text{I}^-}_{\text{A}}\left(\frac{n}{n_i}\right)\right]}{C^*_{\text{I}^0}}\left[\nabla\left(\frac{C_{(\text{AI})}}{\pi_{\text{I}}}\right) + \frac{C_{(\text{AI})}}{\pi_{\text{I}}}\nabla\ln\left(\frac{p}{n_i}\right)\right]. \end{aligned} \tag{A.16}$$

Following a similar approach, $\vec{J}_{(\text{AV})}$ can be written as

$$\begin{aligned} \vec{J}_{(\text{AV})} &= \sum_{i=-1}^{+1}\vec{J}_{(\text{AV})^i} \\ &= -\frac{\left[D^{\text{V}^0}_{\text{A}} + D^{\text{V}^+}_{\text{A}}\left(\frac{p}{n_i}\right) + D^{\text{V}^-}_{\text{A}}\left(\frac{n}{n_i}\right)\right]}{C^*_{\text{V}^0}}\left[\nabla\left(\frac{C_{(\text{AV})}}{\pi_{\text{V}}}\right) + \frac{C_{(\text{AV})}}{\pi_{\text{V}}}\nabla\ln\left(\frac{p}{n_i}\right)\right] \end{aligned} \tag{A.17}$$

A.2 $\vec{J}_{\mathrm{I}}$ *and* $\vec{J}_{\mathrm{V}}$

The total flux of point defects also consists of both diffusion and drift terms, as well as all the charge states. It can be written in terms of the gradient in the neutral concentration of point defects and the free carrier concentrations. For $\vec{J}_{\mathrm{I}}^{i}$,

$$\vec{J}_{\mathrm{I}^i} = -d_{\mathrm{I}^i}\left(\nabla C_{\mathrm{I}^i} - \frac{iq\mathcal{E}}{kT}C_{\mathrm{I}^i}\right) = -d_{\mathrm{I}^i}K_{\mathrm{I}^i}\left(\frac{n_i}{n}\right)^i \nabla C_{\mathrm{I}^0}, \tag{A.18}$$

where d_{I^i} represents the diffusivity of interstitials of charge state i. We assume that $d_{\mathrm{I}^i} = d_{\mathrm{I}^0}$ throughout this work. The total interstitial flux is then written as

$$\vec{J}_{\mathrm{I}} = \sum_i \vec{J}_{\mathrm{I}^i} = -d_{\mathrm{I}^0}\chi_{\mathrm{I}}\nabla C_{\mathrm{I}^0}, \tag{A.19}$$

where χ_{I} is from Eq. A.5 and written as

$$\chi_{\mathrm{I}} = 1 + K_{\mathrm{I}^+}\left(\frac{p}{n_i}\right) + K_{\mathrm{I}^-}\left(\frac{n}{n_i}\right). \tag{A.20}$$

As for vacancies,

$$\begin{aligned} \vec{J}_{\mathrm{V}} &= -d_{\mathrm{V}^0}\chi_{\mathrm{V}}\nabla C_{\mathrm{V}^0} \\ \chi_{\mathrm{V}} &= 1 + K_{\mathrm{V}^+}\left(\frac{p}{n_i}\right) + K_{\mathrm{V}^-}\left(\frac{n}{n_i}\right). \end{aligned} \tag{A.21}$$

A.3 *R's*

The net rates of pairing and recombination reactions, (Eqs. 2.35 to 2.40), are also summed over all the charge states. Using the definitions of χ_I, χ_V and π_I, π_V from Eq. A.5 and A.8, the net reaction rates of the pairing and recombination reactions are expressed as

$$\begin{aligned} R_{\mathrm{A/I}} &= k_{\mathrm{A/I}}\left[C_{\mathrm{A}}C_{\mathrm{I}} - \frac{\chi_{\mathrm{I}}}{\pi_{\mathrm{I}}}C_{(\mathrm{AI})}\right], \\ R_{\mathrm{A/V}} &= k_{\mathrm{A/V}}\left[C_{\mathrm{A}}C_{\mathrm{V}} - \frac{\chi_{\mathrm{I}}}{\pi_{\mathrm{I}}}C_{(\mathrm{AV})}\right], \\ R_{(\mathrm{AI})/\mathrm{V}} &= k_{(\mathrm{AI})/\mathrm{V}}\left(C_{(\mathrm{AI})}C_{\mathrm{V}} - C^*_{\mathrm{I}^0}C^*_{\mathrm{V}^0}\pi_{\mathrm{I}}\chi_{\mathrm{V}}C_{\mathrm{A}}\right), \\ R_{(\mathrm{AV})/\mathrm{I}} &= k_{(\mathrm{AV})/\mathrm{I}}\left(C_{(\mathrm{AV})}C_{\mathrm{I}} - C^*_{\mathrm{I}^0}C^*_{\mathrm{V}^0}\pi_{\mathrm{V}}\chi_{\mathrm{I}}C_{\mathrm{A}}\right), \\ R_{(\mathrm{AV})/(\mathrm{AI})} &= k_{(\mathrm{AV})/(\mathrm{AI})}\left(C_{(\mathrm{AV})}C_{(\mathrm{AI})} - C^*_{\mathrm{I}^0}C^*_{\mathrm{V}^0}\pi_{\mathrm{I}}\pi_{\mathrm{V}}C^2_{\mathrm{A}}\right). \end{aligned} \tag{A.22}$$

Assuming the reactions are diffusion limited, $k_{\mathrm{X/Y}}$ can then be written as

$$k_{\mathrm{X/Y}} = 4\pi a_0 \left(d_{\mathrm{X}} + d_{\mathrm{Y}}\right), \tag{A.23}$$

where a_0 is the effective capture radius.

Appendix B

DERIVATIONS OF KINETIC PRECIPITATION FACTORS FOR DIFFERENT GEOMETRY OF PRECIPITATES

To calculate the kinetic precipitation factors, steady state diffusion and reaction at the precipitated surface can be solved using the technique from Dunham *et al.* [30]. Gencer *et al.* [40] calculated and compared the kinetic precipitation factors for spherical, disc-shaped, and {311} defects. The capture cross sections for a spherical and {311} defect are shown in Fig. B.1 respectively.

For widely spaced precipitates, a simple expression first approximates a precipitate by a series of spheres with the same surface area. Then we can superimpose the diffusion fields due to the linearity of the diffusion equation. For a single sphere in an infinite domain, the concentration is given by $C_s b/r$, where C_s is the surface concentration, r is the distance from the center of the sphere, and b is the reaction distance (one lattice spacing). Assuming the system is in steady state, the diffusion flux of solute toward the precipitate surface is equal to the reaction flux at the surface. Thus,

$$\begin{aligned} \text{diffusion flux} &= \text{reaction flux} \\ -A_n D \left.\frac{\partial C}{\partial r}\right|_{r=\text{surface}} &= A_n k (C^i - C_n^*), \end{aligned} \tag{B.1}$$

where n is the precipitate size, A_n is the active attachment area, D is the solute diffusivity, k is the interface reaction rate, C^i the solute concentration near the precipitate surface, and C_n^* the the solute concentration at equilibrium with a precipitate of size n. The kinetic precipitation factor can be derived as

$$\lambda_n = \frac{A_n}{R_{eff} + \frac{D}{k}}, \tag{B.2}$$

where R_{eff} and A_n for different defects are listed in Table. B.1. Often the system is considered diffusion-limited from Ham *et al.* [58], $k^{-1} \approx 0$. Therefore, Eq. B.2 becomes

Eq. B.3.

$$\lambda_n = \frac{A_n}{R_{eff}} \tag{B.3}$$

Table B.1: The kinetic factors for defects with different geometry [40]. r_n and R_n are the radius of a sphere and a ring. b is the reaction distance. l and w are specified in Fig. B.1[b].

Defects	Area (A_n)	Effective radius (R_{eff})
Spherical	$4\pi(r_n+b)^2$	r_n+b
Disc-shaped	$4\pi^2 R_n b$	$b\ln\left(\frac{8R_n}{b}\right)$
{311}	$4\pi bw + 8\pi b^2$	$\frac{\ln\left[1+\sqrt{1+\left(\frac{2b}{w}\right)^2}\right] - \ln\left(\frac{b}{l+b}\right) + \ln\left[1+\sqrt{1+\left(\frac{2(b+l)}{w}\right)^2}\right]}{\left[b\sqrt{1+\left(\frac{2b}{w}\right)^2}\right]^{-1} + \left[(b+l)\sqrt{1+\left(\frac{2(b+l)}{w}\right)^2}\right]^{-1}}$

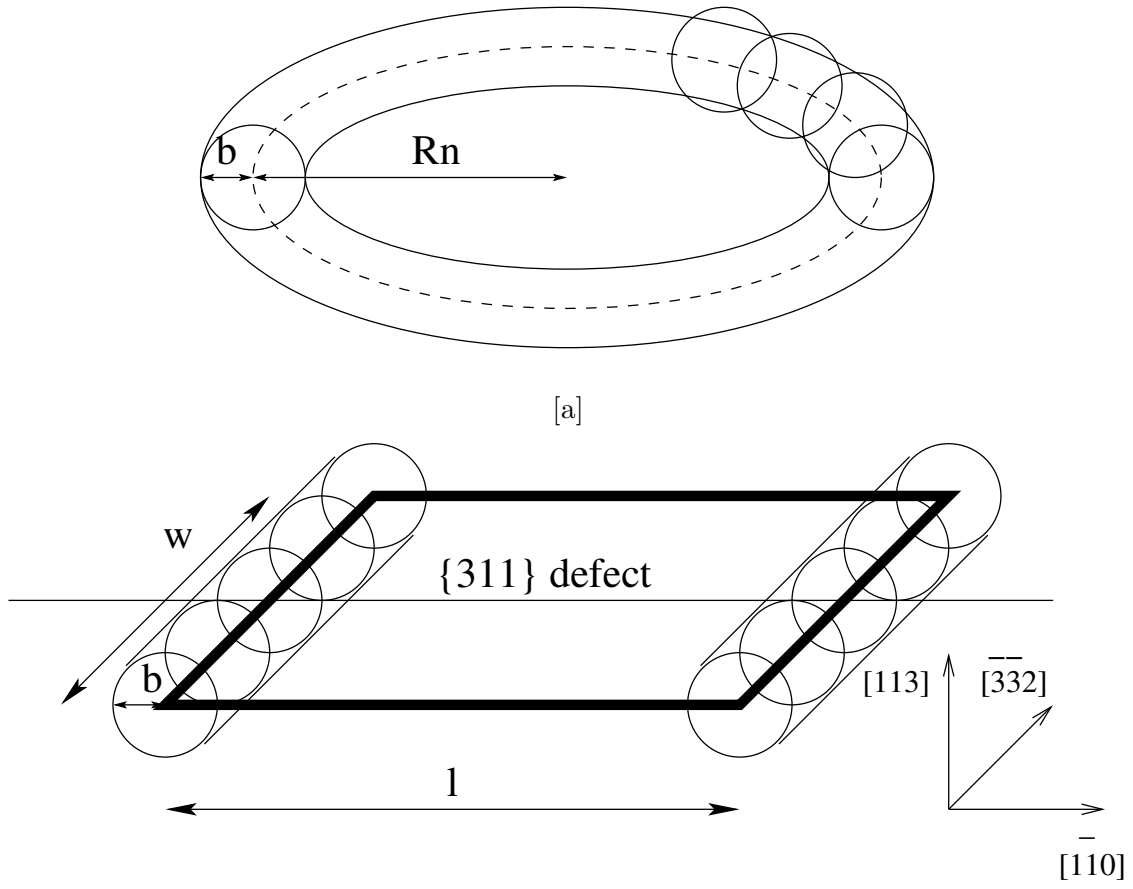

Figure B.1: The capture cross section of disc-shaped and {311} defects.

Appendix C

POISSON'S EQUATION: FROM ODE TO PDE

Conventionally, the electrostatic potential is defined in terms of the intrinsic Fermi level,

$$\Psi_i = -\frac{E_i}{q}. \tag{C.1}$$

The negative sign in Eq. C.1 is due to the fact that E_i is defined as electron energy while Ψ_i is defined for a positive charge. The electric field can then be written as

$$\mathcal{E} = -\frac{\partial \Psi_i}{\partial x}. \tag{C.2}$$

Poisson's equation is defined as

$$\frac{\partial^2 \Psi_i}{\partial x^2} = -\frac{\partial \mathcal{E}}{\partial x} = -\frac{\rho}{\epsilon_{\mathrm{Si}}}, \tag{C.3}$$

where ρ is the charge density per volume and ϵ_{Si} is the permittivity of silicon. The electron concentration can be expressed in terms of electrostatic potential as

$$n = n_i \exp\left[\frac{q(E_f - E_i)}{kT}\right] = n_i \exp\left[\frac{q(\Psi_i - \Psi_f)}{kT}\right]. \tag{C.4}$$

Eqs. C.3 and C.4 can be combined into

$$\frac{\partial^2 \Psi_i}{\partial x^2} = \frac{kT}{q}\frac{\partial^2}{\partial x^2}\left[\ln\left(\frac{n}{n_i}\right)\right] = \frac{q\left(p - n + N_d^+ - N_a^-\right)}{\epsilon_{\mathrm{Si}}}, \tag{C.5}$$

where N_d^+ and N_a^- are the concentrations of ionized donors and acceptors. n and p are the concentrations of electrons and holes. The hole concentration can be substituted by using mass action, Eq. C.6.

$$pn = n_i^2 \tag{C.6}$$

To form partial differential equation (PDE) for the solver we used (DOPDEES/PMM [41]), the ordinary differential equation (ODE) in Eq. C.5 is con-

verted to Eq. C.7.

$$\frac{\partial}{\partial t}\left[\ln\left(\frac{n}{n_i}\right)\right] = \frac{1}{\tau}\left\{\frac{q\left(\frac{n_i^2}{n} - n + N_d^+ - N_a^-\right)}{\epsilon_{\mathrm{Si}}} + \frac{kT}{q}\frac{\partial^2}{\partial x^2}\left[\ln\left(\frac{n}{n_i}\right)\right]\right\} \tag{C.7}$$

where τ is chosen large enough to make the expression in $\{\}$ in Eq.C.5 small, which enforces Eq.C.5.

Analytically, we can adopt the simple depletion approximation and calculate the depletion width, as well as the electron distribution. In analyzing Cu outdiffusion in Chapter 4, we pinned the Fermi level near mid-bandgap at the surface. The depletion width can then be written as

$$W_d = \sqrt{\frac{2\epsilon_{\mathrm{Si}}}{qN_a}} \approx 0.17\mu\mathrm{m}, \tag{C.8}$$

where $N_a = 1.5 \times 10^{16}\mathrm{cm}^{-3}$ is used. The resulting electrostatic field is express as

$$\Psi(x) = \Psi_s\left(1 - \frac{x}{W_d}\right)^2, \tag{C.9}$$

where Ψ_s is the electrostatic potential at the surface. The electron distribution is calculated and written as

$$n(x) = \frac{n_i^2}{N_a}\exp\left[\frac{q\Psi_s}{kT}\left(1 - \frac{x}{W_d}\right)^2\right]. \tag{C.10}$$

Fig. C.1 shows an excellent agreement between the electron distributions from both simple analytical approximation and the outdiffusion model.

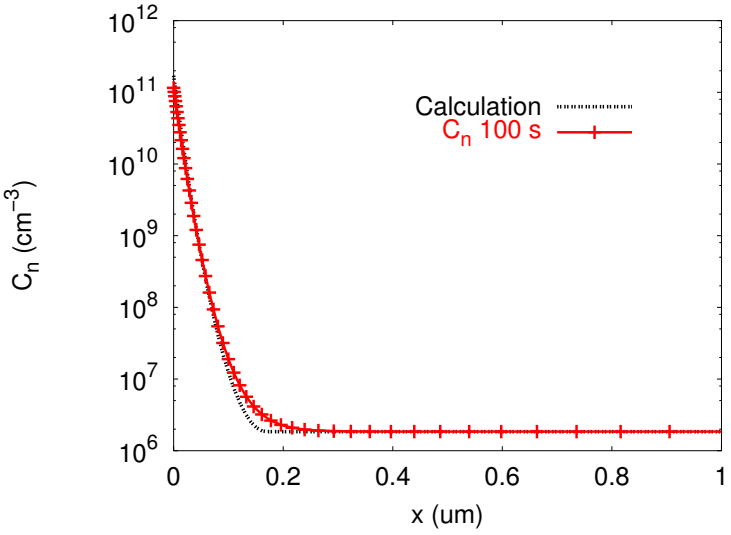

Figure C.1: Comparison of electron distribution between the simple analytical results and simulation results from outdiffusion model.

Appendix D

DERIVATIONS OF RATE EQUATIONS FOR BORON INTERSTITIAL CLUSTERS (BICS)

In the following derivation, the effect of charge states is included for the clustering model. We will discuss 3 critical forms of BICs, $(B_2I)^0$, $(B_3I)^0$, and $(BI_2)^+$, individually.

D.1 $(B_2I)^0$

$$(BI)^- + B^- \quad \Leftrightarrow \quad (B_2I)^0 + 2e^- \tag{D.1}$$

$$(BI)^0 + B^- \quad \Leftrightarrow \quad (B_2I)^0 + e^- \tag{D.2}$$

The reaction rates for Eq. D.1 and D.2 are expressed as

$$R_{(BI)^-/B^-} = k_{(BI)^-/B^-}\left[C_{(BI)^-}C_{B^-} - \frac{C_{(B_2I)^0}\left(\frac{n}{n_i}\right)^2}{K^{eq}_{(BI)^-/B^-}}\right], \tag{D.3}$$

$$R_{(BI)^0/B^-} = k_{(BI)^0/B^-}\left[C_{(BI)^0}C_{B^-} - \frac{C_{(B_2I)^0}\left(\frac{n}{n_i}\right)}{K^{eq}_{(BI)^0/B^-}}\right], \tag{D.4}$$

where

$$K^{eq}_{(BI)^-/B^-} = \frac{C_{(B_2I)^0}\left(\frac{n}{n_i}\right)^2}{C_{(BI)^-}C_{B^-}}, \tag{D.5}$$

$$K^{eq}_{(BI)^0/B^-} = \frac{C_{(B_2I)^0}\left(\frac{n}{n_i}\right)}{C_{(BI)^0}C_{B^-}}. \tag{D.6}$$

Using Eq. D.5 and. D.6, Eq. D.4 becomes

$$R_{(BI)^0/B^-} = k_{(BI)^0/B^-}\frac{C_{(BI)^0}}{C_{(BI)^-}}\left[C_{(BI)^-}C_{B^-} - \frac{C_{(B_2I)^0}\left(\frac{n}{n_i}\right)^2}{K^{eq}_{(BI)^-/B^-}}\right]. \tag{D.7}$$

Including

$$\frac{k_{(\mathrm{BI})^0/\mathrm{B}^-}}{k_{(\mathrm{BI})^-/\mathrm{B}^-}} = \frac{d_{(\mathrm{BI})^0}}{d_{(\mathrm{BI})^-}}, \tag{D.8}$$

the total reaction rate is then the sum of Eq. D.3 and D.4.

$$\begin{aligned} R_{(\mathrm{B_2I})^0} &= k_{(\mathrm{BI})^-/B^-}\left[1+\frac{k_{(\mathrm{BI})^0/(\mathrm{B_2I})^0}}{k_{(\mathrm{BI})^-/(\mathrm{B_2I})^0}}\frac{C_{(\mathrm{BI})^0}}{C_{(\mathrm{BI})^-}}\right]\left[C_{(\mathrm{BI})^-}C_{B^-}-\frac{C_{(\mathrm{B_2I})^0}\left(\frac{n}{n_i}\right)^2}{K^{eq}_{(\mathrm{BI})^-/B^-}}\right] \\ &= 4\pi a_0 d_{BI}\left[\frac{D_B^0+D_B^+\left(\frac{p}{n_i}\right)}{D_B^0}\right]K^{eq}_{(\mathrm{BI})^-}\left[\frac{C_{(\mathrm{BI})^-}C_{B^-}}{K^{eq}_{(\mathrm{BI})^-}}-\frac{C_{(\mathrm{B_2I})^0}\left(\frac{n}{n_i}\right)^2}{K^{eq}_{(\mathrm{B_2I})^0}}\right], \end{aligned} \tag{D.9}$$

where

$$K^{eq}_{(\mathrm{B_2I})^0} = K^{eq}_{(\mathrm{BI})^-/B^-}K^{eq}_{(\mathrm{BI})^-}. \tag{D.10}$$

D.2 $(\mathrm{B_3I})^0$

$$(\mathrm{BI})^- + (\mathrm{B_2I})^0 \Leftrightarrow (\mathrm{B_3I})^0 + \mathrm{I}^0 + e^- \tag{D.11}$$

$$(\mathrm{BI})^0 + (\mathrm{B_2I})^0 \Leftrightarrow (\mathrm{B_3I})^0 + \mathrm{I}^0 \tag{D.12}$$

The reaction rates for Eq. D.11and D.12 are expressed as

$$R_{(\mathrm{BI})^-/(\mathrm{B_2I})^0} = k_{(\mathrm{BI})^-/(\mathrm{B_2I})^0}\left[C_{(\mathrm{BI})^-}C_{(\mathrm{B_2I})^0}-\frac{C_{(\mathrm{B_3I})^0}C_{\mathrm{I}^0}\left(\frac{n}{n_i}\right)}{K^{eq}_{(\mathrm{BI})^-/(\mathrm{B_2I})^0}}\right], \tag{D.13}$$

$$R_{(\mathrm{BI})^0/(\mathrm{B_2I})^0} = k_{(\mathrm{BI})^0/(\mathrm{B_2I})^0}\left[C_{(\mathrm{BI})^0}C_{(\mathrm{B_2I})^0}-\frac{C_{(\mathrm{B_3I})^0}C_{\mathrm{I}^0}}{K^{eq}_{(\mathrm{BI})^0/(\mathrm{B_2I})^0}}\right], \tag{D.14}$$

where

$$K^{eq}_{(\mathrm{BI})^-/(\mathrm{B_2I})^0} = \frac{C_{(\mathrm{B_3I})^0}C_{\mathrm{I}^0}\left(\frac{n}{n_i}\right)}{C_{(\mathrm{BI})^-}C_{(\mathrm{B_2I})^0}}, \tag{D.15}$$

$$K^{eq}_{(\mathrm{BI})^0/(\mathrm{B_2I})^0} = \frac{C_{(\mathrm{B_3I})^0}C_{\mathrm{I}^0}}{C_{(\mathrm{BI})^0}C_{(\mathrm{B_2I})^0}}. \tag{D.16}$$

Using Eq. D.15 and. D.16, Eq. D.14 becomes

$$R_{(\mathrm{BI})^0/(\mathrm{B_2I})^0} = k_{(\mathrm{BI})^0/(\mathrm{B_2I})^0}\left[\frac{C_{(\mathrm{BI})^0}}{C_{(\mathrm{BI})^-}}\right]\left[C_{(\mathrm{BI})^-}C_{(\mathrm{B_2I})^0} - \frac{C_{(\mathrm{B_3I})^0}C_{\mathrm{I}^0}\left(\frac{n}{n_i}\right)}{K^{eq}_{(\mathrm{BI})^-/(\mathrm{B_2I})^0}}\right]. \tag{D.17}$$

The total reaction rate is the sum of Eq. D.13 and D.17.

$$R_{(\mathrm{B_3I})^0} = k_{(\mathrm{BI})^-/(\mathrm{B_2I})^0}\left[1 + \frac{k_{(\mathrm{BI})^0/(\mathrm{B_2I})^0}}{k_{(\mathrm{BI})^-/(\mathrm{B_2I})^0}}\frac{C_{(\mathrm{BI})^0}}{C_{(\mathrm{BI})^-}}\right]\left[C_{(\mathrm{BI})^-}C_{(\mathrm{B_2I})^0} - \frac{C_{(\mathrm{B_3I})^0}C_{\mathrm{I}^0}\left(\frac{n}{n_i}\right)}{K^{eq}_{(\mathrm{BI})^-/(\mathrm{B_2I})^0}}\right] \tag{D.18}$$

Including

$$\frac{k_{(\mathrm{BI})^0/(\mathrm{B_2I})^0}}{k_{(\mathrm{BI})^-/(\mathrm{B_2I})^0}} = \frac{d_{(\mathrm{BI})^0}}{d_{(\mathrm{BI})^-}}, \tag{D.19}$$

and

$$D^0_B = K^{eq}_{(\mathrm{BI})^-}C^*_{\mathrm{I}^0}d_{(\mathrm{BI})^-}, \tag{D.20}$$

Eq. D.18 can be expressed as

$$\begin{aligned}
R_{(\mathrm{B_3I})^0} &= \gamma 4\pi a_0 d_{(\mathrm{BI})^-}\left[1 + \frac{D^+_B\left(\frac{p}{n_i}\right)}{D^0_B}\right]\left[C_{(\mathrm{BI})^-}C_{(\mathrm{B_2I})^0} - \frac{C_{(\mathrm{B_3I})^0}C_{\mathrm{I}^0}\left(\frac{n}{n_i}\right)}{K^{eq}_{(\mathrm{BI})^-/(\mathrm{B_2I})^0}}\right] \\
&= \frac{\gamma 4\pi a_0}{C^*_{\mathrm{I}^0}}\left[D^0_B + D^+_B\left(\frac{p}{n_i}\right)\right]\left[\frac{C_{(\mathrm{BI})^-}C_{(\mathrm{B_2I})^0}}{K^{eq}_{(\mathrm{BI})^-}} - \frac{C_{(\mathrm{B_3I})^0}C_{\mathrm{I}^0}\left(\frac{n}{n_i}\right)}{K^{eq}_{(\mathrm{BI})^-}K^{eq}_{(\mathrm{BI})^-/(\mathrm{B_2I})^0}}\right] \\
&= \frac{\gamma 4\pi a_0}{C^*_{\mathrm{I}^0}}\left[D^0_B + D^+_B\left(\frac{p}{n_i}\right)\right]\left[\frac{C_{(\mathrm{BI})^-}C_{(\mathrm{B_2I})^0}}{K^{eq}_{(\mathrm{BI})^-}} - \frac{K^{eq}_{(\mathrm{B_2I})^0}C_{(\mathrm{B_3I})^0}C_{\mathrm{I}^0}}{K^{eq}_{(\mathrm{B_3I})^0}\left(\frac{p}{n_i}\right)}\right],
\end{aligned} \tag{D.21}$$

where γ represents a probability factor from Eq. 5.34, and

$$K^{eq}_{(\mathrm{B_3I})^0} = K^{eq}_{(\mathrm{BI})^-/(\mathrm{B_2I})^0}K^{eq}_{(\mathrm{BI})^-}K^{eq}_{(\mathrm{B_2I})^0}. \tag{D.22}$$

D.3 $(BI_2)^+$

$$(BI)^0 + I^+ \Leftrightarrow (BI_2)^+ \tag{D.23}$$

$$(BI)^0 + I^0 \Leftrightarrow (BI_2)^+ + e^- \tag{D.24}$$

$$(BI)^- + I^+ \Leftrightarrow (BI_2)^+ + e^- \tag{D.25}$$

$$(BI)^- + I^0 \Leftrightarrow (BI_2)^+ + 2e^- \tag{D.26}$$

The reaction rates for Eq. D.23, D.24, D.25and D.25 are expressed as

$$R_{(BI)^0/I^+} = k_{(BI)^0/I^+}\left[C_{(BI)^0}C_{I^+} - \frac{C_{(BI_2)^+}}{K^{eq}_{(BI)^0/I^+}}\right], \tag{D.27}$$

$$R_{(BI)^0/I^0} = k_{(BI)^0/I^0}\left[C_{(BI)^0}C_{I^0} - \frac{C_{(BI_2)^+}\left(\frac{n}{n_i}\right)}{K^{eq}_{(BI)^0/I^0}}\right], \tag{D.28}$$

$$R_{(BI)^-/I^+} = k_{(BI)^-/I^+}\left[C_{(BI)^-}C_{I^+} - \frac{C_{(BI_2)^+}\left(\frac{n}{n_i}\right)}{K^{eq}_{(BI)^-/I^+}}\right], \tag{D.29}$$

$$R_{(BI)^-/I^0} = k_{(BI)^-/I^0}\left[C_{(BI)^-}C_{I^0} - \frac{C_{(BI_2)^+}\left(\frac{n}{n_i}\right)^2}{K^{eq}_{(BI)^-/I^0}}\right], \tag{D.30}$$

where

$$K^{eq}_{(BI)^0/I^+} = \frac{C_{(BI_2)^+}}{C_{(BI)^0}C_{I^+}}, \tag{D.31}$$

$$K^{eq}_{(BI)^0/I^0} = \frac{C_{(BI_2)^+}\left(\frac{n}{n_i}\right)}{C_{(BI)^0}C_{I^0}}, \tag{D.32}$$

$$K^{eq}_{(BI)^-/I^+} = \frac{C_{(BI_2)^+}\left(\frac{n}{n_i}\right)}{C_{(BI)^-}C_{I^+}}, \tag{D.33}$$

$$K^{eq}_{(BI)^-/I^0} = \frac{C_{(BI_2)^+}\left(\frac{n}{n_i}\right)^2}{C_{(BI)^-}C_{I^0}}. \tag{D.34}$$

If we assume that $k_{(\mathrm{BI})^-/\mathrm{I}^0} = k_{(\mathrm{BI})^0/\mathrm{I}^0} = k_{(\mathrm{BI})^-/\mathrm{I}^+} = k_{(\mathrm{BI})^0/\mathrm{I}^+}$, the total reaction rate is then expressed as

$$\begin{aligned} R_{(\mathrm{BI}_2)^+} &= k_{(\mathrm{BI})^-/\mathrm{I}^0}\left(1+\frac{C_{(\mathrm{BI})^0}}{C_{(\mathrm{BI})^-}}\right)\left(1+\frac{C_{\mathrm{I}^+}}{C_{\mathrm{I}^0}}\right)\left[C_{(\mathrm{BI})^-}C_{\mathrm{I}^0}-\frac{C_{(\mathrm{BI}_2)^+}\left(\frac{n}{n_i}\right)^2}{K^{eq}_{(\mathrm{BI})^-/\mathrm{I}^0}}\right] \\ &= 4\pi a_0\left(d_{(\mathrm{BI})^-}+d_{\mathrm{I}^0}\right)\left[1+K_{\mathrm{I}^+}\left(\frac{p}{n_i}\right)\right]\left[1+\frac{D_B^+\left(\frac{p}{n_i}\right)}{D_B^0}\right]\cdot \\ & \quad K^{eq}{}_{(\mathrm{BI})^-}\left[\frac{C_{(\mathrm{BI})^-}C_{\mathrm{I}^0}}{K^{eq}{}_{(\mathrm{BI})^-}}-\frac{C_{(\mathrm{BI}_2)^+}\left(\frac{n}{n_i}\right)^2}{K^{eq}_{(\mathrm{BI}_2)^+}}\right], \end{aligned} \tag{D.35}$$

where

$$K^{eq}_{(\mathrm{BI}_2)^+} = K^{eq}_{(\mathrm{BI})^-/\mathrm{I}^-}K^{eq}_{(\mathrm{BI})^-}. \tag{D.36}$$

Appendix E

MODIFICATION OF THE DIFFUSIVITY FOR POINT DEFECTS UNDER STRESS

$$D_{\mathrm{X}}C_{\mathrm{X}}^{*} = \theta_{\mathrm{X}}C_S \exp\left(-\frac{E_f^{\mathrm{X}}}{kT}\right) D_0 \exp\left(-\frac{E_m^{\mathrm{X}}}{kT}\right) = \theta_{\mathrm{X}}C_S D_0 \exp\left(-\frac{E_f^{\mathrm{T}}}{kT}\right) \tag{E.1}$$

$$E_f^{\mathrm{T}}(\vec{\sigma}) = E_f^{\mathrm{T}}(0) + \Delta E_f^{\mathrm{T}}(\vec{\sigma}) \tag{E.2}$$

$$\frac{(D_{\mathrm{X}}C_{\mathrm{X}}^{*})(\vec{\sigma})}{(D_{\mathrm{X}}C_{\mathrm{X}}^{*})(0)} = \frac{(\theta_{\mathrm{X}}D_0)(\vec{\sigma})}{(\theta_{\mathrm{X}}D_0)(0)} \exp\left(-\frac{\Delta E_f^{\mathrm{T}}(\vec{\sigma})}{kT}\right) \approx \exp\left(-\frac{\Delta E_f^{\mathrm{T}}(\vec{\sigma})}{kT}\right) \tag{E.3}$$

$$\frac{D_{\mathrm{X}}(\vec{\sigma})}{D_{\mathrm{X}}(0)} = \frac{(D_{\mathrm{X}}C_{\mathrm{X}}^{*})(\vec{\sigma})}{(D_{\mathrm{X}}C_{\mathrm{X}}^{*})(0)} \cdot \frac{C_{\mathrm{X}}^{*}(\vec{\sigma})}{C_{\mathrm{X}}^{*}(0)} = \exp\left(-\frac{\Delta E_f^{\mathrm{T}}(\vec{\sigma}) - \Delta E_f^{\mathrm{X}}(\vec{\sigma})}{kT}\right) \tag{E.4}$$

Table E.1: Induced strains for I and V transition state from Diebel [28].

	$\mathrm{I}_{\mathrm{trans}}$	$\mathrm{V}_{\mathrm{trans}}$
$\Delta\epsilon$ (eV)	[0.5421, 0.0257, 0.1089]	-0.4199

Appendix F

TWO-STEP TRANSITION VECTORS FOR CI

Table F.1 shows the transition vectors between different states. Under stress-free condition, there are four possible transition paths with an equal probability for a given initial state (both position and orientation) as shown in Fig. 6.3. However, these four possible transition paths have different probabilities under stress. A modification of these transition barriers needs to be considered using Eqs. 5.19 and 6.5. Tables F.2-F.7 list all the detailed information required for KLMC simulation along with the random walk process under a biaxial stress condition (x and y direction). Note that the displacement after each hop is $\vec{t} \cdot a/4$, where a is the silicon lattice constant ($\sim$5.4566A).

Table F.1: Transition vectors for KLMC: first transition ($\vec{t_1}$) and second transition ($\vec{t_2}$).

$\vec{t_1}$	$\vec{t_2}$
(1, 1, 1)	(-1, -1 , -1)
(-1, -1, 1)	(1, 1 , -1)
(1, -1, -1)	(-1, 1 , 1)
(-1, 1, -1)	(1, -1 , 1)

Table F.2: The initial state is CI with a "[100]" orientation at position (0, 0, 0). First (fourth) column is the first (second) transition vector $\vec{t_1}$ ($\vec{t_2}$); Second (fifth) column shows both position and orientation after first (second) hopping step; third (sixth) column is the induced strain at the transition state during the first (second) hop; the last column summarizes the total displacement after two hopping steps.

$\vec{t_1}$	Pos./Orient.	$\Delta\vec{\epsilon}$	$\vec{t_2}$	Pos./Orient.	$\Delta\vec{\epsilon}$	$\Delta\vec{x}_{ij}$
[1,1,1]	$(\frac{5}{4},\frac{5}{4},\frac{5}{4})[0\bar{1}0]$	$[\epsilon,\epsilon,\bar{\epsilon}]$	$[\bar{1},\bar{1},\bar{1}]$	$(1,1,1)[100]$	$[\epsilon,\epsilon,\bar{\epsilon}]$	$(0,0,0)$
[1,1,1]	$(\frac{5}{4},\frac{5}{4},\frac{5}{4})[0\bar{1}0]$	$[\epsilon,\epsilon,\bar{\epsilon}]$	$[\bar{1},\bar{1},\bar{1}]$	$(1,1,1)[001]$	$[\bar{\epsilon},\epsilon,\epsilon]$	$(0,0,0)$
[1,1,1]	$(\frac{5}{4},\frac{5}{4},\frac{5}{4})[0\bar{1}0]$	$[\epsilon,\epsilon,\bar{\epsilon}]$	$[1,\bar{1},1]$	$(\frac{6}{4},1,\frac{6}{4})[\bar{1}00]$	$[\epsilon,\epsilon,\bar{\epsilon}]$	$(\frac{2}{4},0,\frac{2}{4})$
[1,1,1]	$(\frac{5}{4},\frac{5}{4},\frac{5}{4})[0\bar{1}0]$	$[\epsilon,\epsilon,\bar{\epsilon}]$	$[1,\bar{1},1]$	$(\frac{6}{4},1,\frac{6}{4})[00\bar{1}]$	$[\bar{\epsilon},\epsilon,\epsilon]$	$(\frac{2}{4},0,\frac{2}{4})$
[1,1,1]	$(\frac{5}{4},\frac{5}{4},\frac{5}{4})[00\bar{1}]$	$[\epsilon,\bar{\epsilon},\epsilon]$	$[\bar{1},\bar{1},\bar{1}]$	$(1,1,1)[100]$	$[\epsilon,\bar{\epsilon},\epsilon]$	$(0,0,0)$
[1,1,1]	$(\frac{5}{4},\frac{5}{4},\frac{5}{4})[00\bar{1}]$	$[\epsilon,\bar{\epsilon},\epsilon]$	$[\bar{1},\bar{1},\bar{1}]$	$(1,1,1)[010]$	$[\bar{\epsilon},\epsilon,\epsilon]$	$(0,0,0)$
[1,1,1]	$(\frac{5}{4},\frac{5}{4},\frac{5}{4})[00\bar{1}]$	$[\epsilon,\bar{\epsilon},\epsilon]$	$[1,1,\bar{1}]$	$(\frac{6}{4},\frac{6}{4},1)[\bar{1}00]$	$[\epsilon,\bar{\epsilon},\epsilon]$	$(\frac{2}{4},\frac{2}{4},0)$
[1,1,1]	$(\frac{5}{4},\frac{5}{4},\frac{5}{4})[00\bar{1}]$	$[\epsilon,\bar{\epsilon},\epsilon]$	$[1,1,\bar{1}]$	$(\frac{6}{4},\frac{6}{4},1)[0\bar{1}0]$	$[\bar{\epsilon},\epsilon,\epsilon]$	$(\frac{2}{4},\frac{2}{4},0)$
$[1,\bar{1},\bar{1}]$	$(\frac{5}{4},\frac{3}{4},\frac{3}{4})[010]$	$[\epsilon,\epsilon,\bar{\epsilon}]$	$[\bar{1},1,1]$	$(1,1,1)[100]$	$[\epsilon,\epsilon,\bar{\epsilon}]$	$(0,0,0)$
$[1,\bar{1},\bar{1}]$	$(\frac{5}{4},\frac{3}{4},\frac{3}{4})[010]$	$[\epsilon,\epsilon,\bar{\epsilon}]$	$[\bar{1},1,1]$	$(1,1,1)[00\bar{1}]$	$[\bar{\epsilon},\epsilon,\epsilon]$	$(0,0,0)$
$[1,\bar{1},\bar{1}]$	$(\frac{5}{4},\frac{3}{4},\frac{3}{4})[010]$	$[\epsilon,\epsilon,\bar{\epsilon}]$	$[1,1,\bar{1}]$	$(\frac{6}{4},1,\frac{2}{4})[\bar{1}00]$	$[\epsilon,\epsilon,\bar{\epsilon}]$	$(\frac{2}{4},0,\text{-}\frac{2}{4})$
$[1,\bar{1},\bar{1}]$	$(\frac{5}{4},\frac{3}{4},\frac{3}{4})[010]$	$[\epsilon,\epsilon,\bar{\epsilon}]$	$[1,1,\bar{1}]$	$(\frac{6}{4},1,\frac{2}{4})[001]$	$[\bar{\epsilon},\epsilon,\epsilon]$	$(\frac{2}{4},0,\text{-}\frac{2}{4})$
$[1,\bar{1},\bar{1}]$	$(\frac{5}{4},\frac{3}{4},\frac{3}{4})[001]$	$[\epsilon,\bar{\epsilon},\epsilon]$	$[\bar{1},1,1]$	$(1,1,1)[100]$	$[\epsilon,\bar{\epsilon},\epsilon]$	$(0,0,0)$
$[1,\bar{1},\bar{1}]$	$(\frac{5}{4},\frac{3}{4},\frac{3}{4})[001]$	$[\epsilon,\bar{\epsilon},\epsilon]$	$[\bar{1},1,1]$	$(1,1,1)[0\bar{1}0]$	$[\bar{\epsilon},\epsilon,\epsilon]$	$(0,0,0)$
$[1,\bar{1},\bar{1}]$	$(\frac{5}{4},\frac{3}{4},\frac{3}{4})[001]$	$[\epsilon,\bar{\epsilon},\epsilon]$	$[1,\bar{1},1]$	$(\frac{6}{4},\frac{2}{4},1)[\bar{1}00]$	$[\epsilon,\bar{\epsilon},\epsilon]$	$(\frac{2}{4},\text{-}\frac{2}{4},0)$
$[1,\bar{1},\bar{1}]$	$(\frac{5}{4},\frac{3}{4},\frac{3}{4})[001]$	$[\epsilon,\bar{\epsilon},\epsilon]$	$[1,\bar{1},1]$	$(\frac{6}{4},\frac{2}{4},1)[010]$	$[\bar{\epsilon},\epsilon,\epsilon]$	$(\frac{2}{4},\text{-}\frac{2}{4},0)$

Table F.3: The initial state is CI with a "[$\bar{1}$00]" orientation at position (0, 0, 0). First (fourth) column is the first (second) transition vector $\vec{t}_1$ ($\vec{t}_2$); Second (fifth) column shows both position and orientation after first (second) hopping step; third (sixth) column is the induced strain at the transition state during the first (second) hop; the last column summarizes the total displacement after two hopping steps.

$\vec{t}_1$	Pos./Orient.	$\Delta\vec{\epsilon}$	$\vec{t}_2$	Pos./Orient.	$\Delta\vec{\epsilon}$	$\Delta\vec{x}_{ij}$
[$\bar{1}$,$\bar{1}$,1]	($\frac{3}{4}$,$\frac{3}{4}$,$\frac{5}{4}$)[010]	[ϵ,ϵ,$\bar{\epsilon}$]	[1,1,$\bar{1}$]	(1,1,1)[$\bar{1}$00]	[ϵ,ϵ,$\bar{\epsilon}$]	(0 , 0 , 0)
[$\bar{1}$,$\bar{1}$,1]	($\frac{3}{4}$,$\frac{3}{4}$,$\frac{5}{4}$)[010]	[ϵ,ϵ,$\bar{\epsilon}$]	[1,1,$\bar{1}$]	(1,1,1)[001]	[$\bar{\epsilon}$,ϵ,ϵ]	(0 , 0 , 0)
[$\bar{1}$,$\bar{1}$,1]	($\frac{3}{4}$,$\frac{3}{4}$,$\frac{5}{4}$)[010]	[ϵ,ϵ,$\bar{\epsilon}$]	[$\bar{1}$,1,1]	($\frac{2}{4}$,1,$\frac{6}{4}$)[100]	[ϵ,ϵ,$\bar{\epsilon}$]	(-$\frac{2}{4}$, 0 , $\frac{2}{4}$)
[$\bar{1}$,$\bar{1}$,1]	($\frac{3}{4}$,$\frac{3}{4}$,$\frac{5}{4}$)[010]	[ϵ,ϵ,$\bar{\epsilon}$]	[$\bar{1}$,1,1]	($\frac{2}{4}$,1,$\frac{6}{4}$)[00$\bar{1}$]	[$\bar{\epsilon}$,ϵ,ϵ]	(-$\frac{2}{4}$, 0 , $\frac{2}{4}$)
[$\bar{1}$,$\bar{1}$,1]	($\frac{3}{4}$,$\frac{3}{4}$,$\frac{5}{4}$)[00$\bar{1}$]	[ϵ,$\bar{\epsilon}$,ϵ]	[1,1,$\bar{1}$]	(1,1,1)[$\bar{1}$00]	[ϵ,$\bar{\epsilon}$,ϵ]	(0 , 0 , 0)
[$\bar{1}$,$\bar{1}$,1]	($\frac{3}{4}$,$\frac{3}{4}$,$\frac{5}{4}$)[00$\bar{1}$]	[ϵ,$\bar{\epsilon}$,ϵ]	[1,1,$\bar{1}$]	(1,1,1)[0$\bar{1}$0]	[$\bar{\epsilon}$,ϵ,ϵ]	(0 , 0 , 0)
[$\bar{1}$,$\bar{1}$,1]	($\frac{3}{4}$,$\frac{3}{4}$,$\frac{5}{4}$)[00$\bar{1}$]	[ϵ,$\bar{\epsilon}$,ϵ]	[$\bar{1}$,$\bar{1}$,$\bar{1}$]	($\frac{2}{4}$,$\frac{2}{4}$,1)[100]	[ϵ,$\bar{\epsilon}$,ϵ]	(-$\frac{2}{4}$,-$\frac{2}{4}$, 0)
[$\bar{1}$,$\bar{1}$,1]	($\frac{3}{4}$,$\frac{3}{4}$,$\frac{5}{4}$)[00$\bar{1}$]	[ϵ,$\bar{\epsilon}$,ϵ]	[$\bar{1}$,$\bar{1}$,$\bar{1}$]	($\frac{2}{4}$,$\frac{2}{4}$,1)[010]	[$\bar{\epsilon}$,ϵ,ϵ]	(-$\frac{2}{4}$,-$\frac{2}{4}$, 0)
[$\bar{1}$,1,$\bar{1}$]	($\frac{3}{4}$,$\frac{5}{4}$,$\frac{3}{4}$)[0$\bar{1}$0]	[ϵ,ϵ,$\bar{\epsilon}$]	[1,$\bar{1}$,1]	(1,1,1)[$\bar{1}$00]	[ϵ,ϵ,$\bar{\epsilon}$]	(0 , 0 , 0)
[$\bar{1}$,1,$\bar{1}$]	($\frac{3}{4}$,$\frac{5}{4}$,$\frac{3}{4}$)[0$\bar{1}$0]	[ϵ,ϵ,$\bar{\epsilon}$]	[1,$\bar{1}$,1]	(1,1,1)[00$\bar{1}$]	[$\bar{\epsilon}$,ϵ,ϵ]	(0 , 0 , 0)
[$\bar{1}$,1,$\bar{1}$]	($\frac{3}{4}$,$\frac{5}{4}$,$\frac{3}{4}$)[0$\bar{1}$0]	[ϵ,ϵ,$\bar{\epsilon}$]	[$\bar{1}$,$\bar{1}$,$\bar{1}$]	($\frac{2}{4}$,1,$\frac{2}{4}$)[100]	[ϵ,ϵ,$\bar{\epsilon}$]	(-$\frac{2}{4}$, 0 ,-$\frac{2}{4}$)
[$\bar{1}$,1,$\bar{1}$]	($\frac{3}{4}$,$\frac{5}{4}$,$\frac{3}{4}$)[0$\bar{1}$0]	[ϵ,ϵ,$\bar{\epsilon}$]	[$\bar{1}$,$\bar{1}$,$\bar{1}$]	($\frac{2}{4}$,1,$\frac{2}{4}$)[001]	[$\bar{\epsilon}$,ϵ,ϵ]	(-$\frac{2}{4}$, 0 ,-$\frac{2}{4}$)
[$\bar{1}$,1,$\bar{1}$]	($\frac{3}{4}$,$\frac{5}{4}$,$\frac{3}{4}$)[001]	[ϵ,$\bar{\epsilon}$,ϵ]	[1,$\bar{1}$,1]	(1,1,1)[$\bar{1}$00]	[ϵ,$\bar{\epsilon}$,ϵ]	(0 , 0 , 0)
[$\bar{1}$,1,$\bar{1}$]	($\frac{3}{4}$,$\frac{5}{4}$,$\frac{3}{4}$)[001]	[ϵ,$\bar{\epsilon}$,ϵ]	[1,$\bar{1}$,1]	(1,1,1)[010]	[$\bar{\epsilon}$,ϵ,ϵ]	(0 , 0 , 0)
[$\bar{1}$,1,$\bar{1}$]	($\frac{3}{4}$,$\frac{5}{4}$,$\frac{3}{4}$)[001]	[ϵ,$\bar{\epsilon}$,ϵ]	[$\bar{1}$,1,1]	($\frac{2}{4}$,$\frac{6}{4}$,1)[100]	[ϵ,$\bar{\epsilon}$,ϵ]	(-$\frac{2}{4}$, $\frac{2}{4}$, 0)
[$\bar{1}$,1,$\bar{1}$]	($\frac{3}{4}$,$\frac{5}{4}$,$\frac{3}{4}$)[001]	[ϵ,$\bar{\epsilon}$,ϵ]	[$\bar{1}$,1,1]	($\frac{2}{4}$,$\frac{6}{4}$,1)[0$\bar{1}$0]	[$\bar{\epsilon}$,ϵ,ϵ]	(-$\frac{2}{4}$, $\frac{2}{4}$, 0)

Table F.4: The initial state is CI with a "[010]" orientation at position (0, 0, 0). First (fourth) column is the first (second) transition vector $\vec{t}_1$ ($\vec{t}_2$); Second (fifth) column shows both position and orientation after first (second) hopping step; third (sixth) column is the induced strain at the transition state during the first (second) hop; the last column summarizes the total displacement after two hopping steps.

$\vec{t}_1$	Pos./Orient.	$\Delta\vec{\epsilon}$	$\vec{t}_2$	Pos./Orient.	$\Delta\vec{\epsilon}$	$\Delta\vec{x}_{ij}$
[1,1,1]	$(\frac{5}{4},\frac{5}{4},\frac{5}{4})[\bar{1}00]$	$[\epsilon,\epsilon,\bar{\epsilon}]$	$[\bar{1},\bar{1},\bar{1}]$	$(1,1,1)[010]$	$[\epsilon,\epsilon,\bar{\epsilon}]$	$(0,0,0)$
[1,1,1]	$(\frac{5}{4},\frac{5}{4},\frac{5}{4})[\bar{1}00]$	$[\epsilon,\epsilon,\bar{\epsilon}]$	$[\bar{1},\bar{1},\bar{1}]$	$(1,1,1)[001]$	$[\epsilon,\bar{\epsilon},\epsilon]$	$(0,0,0)$
[1,1,1]	$(\frac{5}{4},\frac{5}{4},\frac{5}{4})[\bar{1}00]$	$[\epsilon,\epsilon,\bar{\epsilon}]$	$[\bar{1},1,1]$	$(1,\frac{6}{4},\frac{6}{4})[0\bar{1}0]$	$[\epsilon,\epsilon,\bar{\epsilon}]$	$(0,\frac{2}{4},\frac{2}{4})$
[1,1,1]	$(\frac{5}{4},\frac{5}{4},\frac{5}{4})[\bar{1}00]$	$[\epsilon,\epsilon,\bar{\epsilon}]$	$[\bar{1},1,1]$	$(1,\frac{6}{4},\frac{6}{4})[00\bar{1}]$	$[\epsilon,\bar{\epsilon},\epsilon]$	$(0,\frac{2}{4},\frac{2}{4})$
[1,1,1]	$(\frac{5}{4},\frac{5}{4},\frac{5}{4})[00\bar{1}]$	$[\bar{\epsilon},\epsilon,\epsilon]$	$[\bar{1},\bar{1},\bar{1}]$	$(1,1,1)[100]$	$[\epsilon,\bar{\epsilon},\epsilon]$	$(0,0,0)$
[1,1,1]	$(\frac{5}{4},\frac{5}{4},\frac{5}{4})[00\bar{1}]$	$[\bar{\epsilon},\epsilon,\epsilon]$	$[\bar{1},\bar{1},\bar{1}]$	$(1,1,1)[010]$	$[\bar{\epsilon},\epsilon,\epsilon]$	$(0,0,0)$
[1,1,1]	$(\frac{5}{4},\frac{5}{4},\frac{5}{4})[00\bar{1}]$	$[\bar{\epsilon},\epsilon,\epsilon]$	$[1,1,\bar{1}]$	$(\frac{6}{4},\frac{6}{4},1)[\bar{1}00]$	$[\epsilon,\bar{\epsilon},\epsilon]$	$(\frac{2}{4},\frac{2}{4},0)$
[1,1,1]	$(\frac{5}{4},\frac{5}{4},\frac{5}{4})[00\bar{1}]$	$[\bar{\epsilon},\epsilon,\epsilon]$	$[1,1,\bar{1}]$	$(\frac{6}{4},\frac{6}{4},1)[0\bar{1}0]$	$[\bar{\epsilon},\epsilon,\epsilon]$	$(\frac{2}{4},\frac{2}{4},0)$
$[\bar{1},1,\bar{1}]$	$(\frac{3}{4},\frac{5}{4},\frac{3}{4})[100]$	$[\epsilon,\epsilon,\bar{\epsilon}]$	$[1,\bar{1},1]$	$(1,1,1)[010]$	$[\epsilon,\epsilon,\bar{\epsilon}]$	$(0,0,0)$
$[\bar{1},1,\bar{1}]$	$(\frac{3}{4},\frac{5}{4},\frac{3}{4})[100]$	$[\epsilon,\epsilon,\bar{\epsilon}]$	$[1,\bar{1},1]$	$(1,1,1)[00\bar{1}]$	$[\epsilon,\bar{\epsilon},\epsilon]$	$(0,0,0)$
$[\bar{1},1,\bar{1}]$	$(\frac{3}{4},\frac{5}{4},\frac{3}{4})[100]$	$[\epsilon,\epsilon,\bar{\epsilon}]$	$[1,1,\bar{1}]$	$(1,\frac{6}{4},\frac{2}{4})[0\bar{1}0]$	$[\epsilon,\epsilon,\bar{\epsilon}]$	$(0,\frac{2}{4},-\frac{2}{4})$
$[\bar{1},1,\bar{1}]$	$(\frac{3}{4},\frac{5}{4},\frac{3}{4})[100]$	$[\epsilon,\epsilon,\bar{\epsilon}]$	$[1,1,\bar{1}]$	$(1,\frac{6}{4},\frac{2}{4})[001]$	$[\epsilon,\bar{\epsilon},\epsilon]$	$(0,\frac{2}{4},-\frac{2}{4})$
$[\bar{1},1,\bar{1}]$	$(\frac{3}{4},\frac{5}{4},\frac{3}{4})[001]$	$[\bar{\epsilon},\epsilon,\epsilon]$	$[1,\bar{1},1]$	$(1,1,1)[\bar{1}00]$	$[\epsilon,\bar{\epsilon},\epsilon]$	$(0,0,0)$
$[\bar{1},1,\bar{1}]$	$(\frac{3}{4},\frac{5}{4},\frac{3}{4})[001]$	$[\bar{\epsilon},\epsilon,\epsilon]$	$[1,\bar{1},1]$	$(1,1,1)[010]$	$[\bar{\epsilon},\epsilon,\epsilon]$	$(0,0,0)$
$[\bar{1},1,\bar{1}]$	$(\frac{3}{4},\frac{5}{4},\frac{3}{4})[001]$	$[\bar{\epsilon},\epsilon,\epsilon]$	$[\bar{1},1,1]$	$(\frac{2}{4},\frac{6}{4},1)[100]$	$[\epsilon,\bar{\epsilon},\epsilon]$	$(-\frac{2}{4},\frac{2}{4},0)$
$[\bar{1},1,\bar{1}]$	$(\frac{3}{4},\frac{5}{4},\frac{3}{4})[001]$	$[\bar{\epsilon},\epsilon,\epsilon]$	$[\bar{1},1,1]$	$(\frac{2}{4},\frac{6}{4},1)[0\bar{1}0]$	$[\bar{\epsilon},\epsilon,\epsilon]$	$(-\frac{2}{4},\frac{2}{4},0)$

Table F.5: The initial state is CI with a "[0$\bar{1}$0]" orientation at position (0, 0, 0). First (fourth) column is the first (second) transition vector $\vec{t}_1$ ($\vec{t}_2$); Second (fifth) column shows both position and orientation after first (second) hopping step; third (sixth) column is the induced strain at the transition state during the first (second) hop; the last column summarizes the total displacement after two hopping steps.

$\vec{t}_1$	Pos./Orient.	$\Delta\vec{\epsilon}$	$\vec{t}_2$	Pos./Orient.	$\Delta\vec{\epsilon}$	$\Delta\vec{x}_{ij}$
[$\bar{1}$,$\bar{1}$,1]	($\frac{3}{4}$,$\frac{3}{4}$,$\frac{5}{4}$)[100]	[ϵ,ϵ,$\bar{\epsilon}$]	[1,1,$\bar{1}$]	(1,1,1)[0$\bar{1}$0]	[ϵ,ϵ,$\bar{\epsilon}$]	(0 , 0 , 0)
[$\bar{1}$,$\bar{1}$,1]	($\frac{3}{4}$,$\frac{3}{4}$,$\frac{5}{4}$)[100]	[ϵ,ϵ,$\bar{\epsilon}$]	[1,1,$\bar{1}$]	(1,1,1)[001]	[ϵ,$\bar{\epsilon}$,ϵ]	(0 , 0 , 0)
[$\bar{1}$,$\bar{1}$,1]	($\frac{3}{4}$,$\frac{3}{4}$,$\frac{5}{4}$)[100]	[ϵ,ϵ,$\bar{\epsilon}$]	[1,$\bar{1}$,1]	(1,$\frac{2}{4}$,$\frac{6}{4}$)[010]	[ϵ,ϵ,$\bar{\epsilon}$]	(0 ,-$\frac{2}{4}$, $\frac{2}{4}$)
[$\bar{1}$,$\bar{1}$,1]	($\frac{3}{4}$,$\frac{3}{4}$,$\frac{5}{4}$)[100]	[ϵ,ϵ,$\bar{\epsilon}$]	[1,$\bar{1}$,1]	(1,$\frac{2}{4}$,$\frac{6}{4}$)[00$\bar{1}$]	[ϵ,$\bar{\epsilon}$,ϵ]	(0 ,-$\frac{2}{4}$, $\frac{2}{4}$)
[$\bar{1}$,$\bar{1}$,1]	($\frac{3}{4}$,$\frac{3}{4}$,$\frac{5}{4}$)[00$\bar{1}$]	[$\bar{\epsilon}$,ϵ,ϵ]	[1,1,$\bar{1}$]	(1,1,1)[$\bar{1}$00]	[ϵ,$\bar{\epsilon}$,ϵ]	(0 , 0 , 0)
[$\bar{1}$,$\bar{1}$,1]	($\frac{3}{4}$,$\frac{3}{4}$,$\frac{5}{4}$)[00$\bar{1}$]	[$\bar{\epsilon}$,ϵ,ϵ]	[1,1,$\bar{1}$]	(1,1,1)[0$\bar{1}$0]	[$\bar{\epsilon}$,ϵ,ϵ]	(0 , 0 , 0)
[$\bar{1}$,$\bar{1}$,1]	($\frac{3}{4}$,$\frac{3}{4}$,$\frac{5}{4}$)[00$\bar{1}$]	[$\bar{\epsilon}$,ϵ,ϵ]	[$\bar{1}$,$\bar{1}$,$\bar{1}$]	($\frac{2}{4}$,$\frac{2}{4}$,1)[100]	[ϵ,$\bar{\epsilon}$,ϵ]	(-$\frac{2}{4}$,-$\frac{2}{4}$, 0)
[$\bar{1}$,$\bar{1}$,1]	($\frac{3}{4}$,$\frac{3}{4}$,$\frac{5}{4}$)[00$\bar{1}$]	[$\bar{\epsilon}$,ϵ,ϵ]	[$\bar{1}$,$\bar{1}$,$\bar{1}$]	($\frac{2}{4}$,$\frac{2}{4}$,1)[010]	[$\bar{\epsilon}$,ϵ,ϵ]	(-$\frac{2}{4}$,-$\frac{2}{4}$, 0)
[1,$\bar{1}$,$\bar{1}$]	($\frac{5}{4}$,$\frac{3}{4}$,$\frac{3}{4}$)[$\bar{1}$00]	[ϵ,ϵ,$\bar{\epsilon}$]	[$\bar{1}$,1,1]	(1,1,1)[0$\bar{1}$0]	[ϵ,ϵ,$\bar{\epsilon}$]	(0 , 0 , 0)
[1,$\bar{1}$,$\bar{1}$]	($\frac{5}{4}$,$\frac{3}{4}$,$\frac{3}{4}$)[$\bar{1}$00]	[ϵ,ϵ,$\bar{\epsilon}$]	[$\bar{1}$,1,1]	(1,1,1)[00$\bar{1}$]	[ϵ,$\bar{\epsilon}$,ϵ]	(0 , 0 , 0)
[1,$\bar{1}$,$\bar{1}$]	($\frac{5}{4}$,$\frac{3}{4}$,$\frac{3}{4}$)[$\bar{1}$00]	[ϵ,ϵ,$\bar{\epsilon}$]	[$\bar{1}$,$\bar{1}$,$\bar{1}$]	(1,$\frac{2}{4}$,$\frac{2}{4}$)[010]	[ϵ,ϵ,$\bar{\epsilon}$]	(0 ,-$\frac{2}{4}$,-$\frac{2}{4}$)
[1,$\bar{1}$,$\bar{1}$]	($\frac{5}{4}$,$\frac{3}{4}$,$\frac{3}{4}$)[$\bar{1}$00]	[ϵ,ϵ,$\bar{\epsilon}$]	[$\bar{1}$,$\bar{1}$,$\bar{1}$]	(1,$\frac{2}{4}$,$\frac{2}{4}$)[001]	[ϵ,$\bar{\epsilon}$,ϵ]	(0 ,-$\frac{2}{4}$,-$\frac{2}{4}$)
[1,$\bar{1}$,$\bar{1}$]	($\frac{5}{4}$,$\frac{3}{4}$,$\frac{3}{4}$)[001]	[$\bar{\epsilon}$,ϵ,ϵ]	[$\bar{1}$,1,1]	(1,1,1)[100]	[ϵ,$\bar{\epsilon}$,ϵ]	(0 , 0 , 0)
[1,$\bar{1}$,$\bar{1}$]	($\frac{5}{4}$,$\frac{3}{4}$,$\frac{3}{4}$)[001]	[$\bar{\epsilon}$,ϵ,ϵ]	[$\bar{1}$,1,1]	(1,1,1)[0$\bar{1}$0]	[$\bar{\epsilon}$,ϵ,ϵ]	(0 , 0 , 0)
[1,$\bar{1}$,$\bar{1}$]	($\frac{5}{4}$,$\frac{3}{4}$,$\frac{3}{4}$)[001]	[$\bar{\epsilon}$,ϵ,ϵ]	[1,$\bar{1}$,1]	($\frac{6}{4}$,$\frac{2}{4}$,1)[$\bar{1}$00]	[ϵ,$\bar{\epsilon}$,ϵ]	($\frac{2}{4}$,-$\frac{2}{4}$, 0)
[1,$\bar{1}$,$\bar{1}$]	($\frac{5}{4}$,$\frac{3}{4}$,$\frac{3}{4}$)[001]	[$\bar{\epsilon}$,ϵ,ϵ]	[1,$\bar{1}$,1]	($\frac{6}{4}$,$\frac{2}{4}$,1)[010]	[$\bar{\epsilon}$,ϵ,ϵ]	($\frac{2}{4}$,-$\frac{2}{4}$, 0)

Table F.6: The initial state is CI with a "[001]" orientation at position (0, 0, 0). First (fourth) column is the first (second) transition vector $\vec{t}_1$ ($\vec{t}_2$); Second (fifth) column shows both position and orientation after first (second) hopping step; third (sixth) column is the induced strain at the transition state during the first (second) hop; the last column summarizes the total displacement after two hopping steps.

$\vec{t}_1$	Pos./Orient.	$\Delta\vec{\epsilon}$	$\vec{t}_2$	Pos./Orient.	$\Delta\vec{\epsilon}$	$\Delta\vec{x}_{ij}$
[1,1,1]	$(\frac{5}{4},\frac{5}{4},\frac{5}{4})[\bar{1}00]$	$[\epsilon,\bar{\epsilon},\epsilon]$	$[\bar{1},\bar{1},\bar{1}]$	$(1,1,1)[010]$	$[\epsilon,\epsilon,\bar{\epsilon}]$	$(0,0,0)$
[1,1,1]	$(\frac{5}{4},\frac{5}{4},\frac{5}{4})[\bar{1}00]$	$[\epsilon,\bar{\epsilon},\epsilon]$	$[\bar{1},\bar{1},\bar{1}]$	$(1,1,1)[001]$	$[\epsilon,\bar{\epsilon},\epsilon]$	$(0,0,0)$
[1,1,1]	$(\frac{5}{4},\frac{5}{4},\frac{5}{4})[\bar{1}00]$	$[\epsilon,\bar{\epsilon},\epsilon]$	$[\bar{1},1,1]$	$(1,\frac{6}{4},\frac{6}{4})[0\bar{1}0]$	$[\epsilon,\epsilon,\bar{\epsilon}]$	$(0,\frac{2}{4},\frac{2}{4})$
[1,1,1]	$(\frac{5}{4},\frac{5}{4},\frac{5}{4})[\bar{1}00]$	$[\epsilon,\bar{\epsilon},\epsilon]$	$[\bar{1},1,1]$	$(1,\frac{6}{4},\frac{6}{4})[00\bar{1}]$	$[\epsilon,\bar{\epsilon},\epsilon]$	$(0,\frac{2}{4},\frac{2}{4})$
[1,1,1]	$(\frac{5}{4},\frac{5}{4},\frac{5}{4})[0\bar{1}0]$	$[\bar{\epsilon},\epsilon,\epsilon]$	$[\bar{1},\bar{1},\bar{1}]$	$(1,1,1)[100]$	$[\epsilon,\epsilon,\bar{\epsilon}]$	$(0,0,0)$
[1,1,1]	$(\frac{5}{4},\frac{5}{4},\frac{5}{4})[0\bar{1}0]$	$[\bar{\epsilon},\epsilon,\epsilon]$	$[\bar{1},\bar{1},\bar{1}]$	$(1,1,1)[001]$	$[\bar{\epsilon},\epsilon,\epsilon]$	$(0,0,0)$
[1,1,1]	$(\frac{5}{4},\frac{5}{4},\frac{5}{4})[0\bar{1}0]$	$[\bar{\epsilon},\epsilon,\epsilon]$	$[1,\bar{1},1]$	$(\frac{6}{4},1,\frac{6}{4})[\bar{1}00]$	$[\epsilon,\epsilon,\bar{\epsilon}]$	$(\frac{2}{4},0,\frac{2}{4})$
[1,1,1]	$(\frac{5}{4},\frac{5}{4},\frac{5}{4})[0\bar{1}0]$	$[\bar{\epsilon},\epsilon,\epsilon]$	$[1,\bar{1},1]$	$(\frac{6}{4},1,\frac{6}{4})[00\bar{1}]$	$[\bar{\epsilon},\epsilon,\epsilon]$	$(\frac{2}{4},0,\frac{2}{4})$
$[\bar{1},\bar{1},1]$	$(\frac{3}{4},\frac{3}{4},\frac{5}{4})[100]$	$[\epsilon,\bar{\epsilon},\epsilon]$	$[1,1,\bar{1}]$	$(1,1,1)[0\bar{1}0]$	$[\epsilon,\epsilon,\bar{\epsilon}]$	$(0,0,0)$
$[\bar{1},\bar{1},1]$	$(\frac{3}{4},\frac{3}{4},\frac{5}{4})[100]$	$[\epsilon,\bar{\epsilon},\epsilon]$	$[1,1,\bar{1}]$	$(1,1,1)[001]$	$[\epsilon,\bar{\epsilon},\epsilon]$	$(0,0,0)$
$[\bar{1},\bar{1},1]$	$(\frac{3}{4},\frac{3}{4},\frac{5}{4})[100]$	$[\epsilon,\bar{\epsilon},\epsilon]$	$[1,\bar{1},1]$	$(1,\frac{2}{4},\frac{6}{4})[010]$	$[\epsilon,\epsilon,\bar{\epsilon}]$	$(0,-\frac{2}{4},\frac{2}{4})$
$[\bar{1},\bar{1},1]$	$(\frac{3}{4},\frac{3}{4},\frac{5}{4})[100]$	$[\epsilon,\bar{\epsilon},\epsilon]$	$[1,\bar{1},1]$	$(1,\frac{2}{4},\frac{6}{4})[00\bar{1}]$	$[\epsilon,\bar{\epsilon},\epsilon]$	$(0,-\frac{2}{4},\frac{2}{4})$
$[\bar{1},\bar{1},1]$	$(\frac{3}{4},\frac{3}{4},\frac{5}{4})[010]$	$[\bar{\epsilon},\epsilon,\epsilon]$	$[1,1,\bar{1}]$	$(1,1,1)[\bar{1}00]$	$[\epsilon,\epsilon,\bar{\epsilon}]$	$(0,0,0)$
$[\bar{1},\bar{1},1]$	$(\frac{3}{4},\frac{3}{4},\frac{5}{4})[010]$	$[\bar{\epsilon},\epsilon,\epsilon]$	$[1,1,\bar{1}]$	$(1,1,1)[001]$	$[\bar{\epsilon},\epsilon,\epsilon]$	$(0,0,0)$
$[\bar{1},\bar{1},1]$	$(\frac{3}{4},\frac{3}{4},\frac{5}{4})[010]$	$[\bar{\epsilon},\epsilon,\epsilon]$	$[\bar{1},1,1]$	$(\frac{2}{4},1,\frac{6}{4})[100]$	$[\epsilon,\epsilon,\bar{\epsilon}]$	$(-\frac{2}{4},0,\frac{2}{4})$
$[\bar{1},\bar{1},1]$	$(\frac{3}{4},\frac{3}{4},\frac{5}{4})[010]$	$[\bar{\epsilon},\epsilon,\epsilon]$	$[\bar{1},1,1]$	$(\frac{2}{4},1,\frac{6}{4})[00\bar{1}]$	$[\bar{\epsilon},\epsilon,\epsilon]$	$(-\frac{2}{4},0,\frac{2}{4})$

Table F.7: The initial state is CI with a "[00$\bar{1}$]" orientation at position (0, 0, 0). First (fourth) column is the first (second) transition vector $\vec{t}_1$ ($\vec{t}_2$); Second (fifth) column shows both position and orientation after first (second) hopping step; third (sixth) column is the induced strain at the transition state during the first (second) hop; the last column summarizes the total displacement after two hopping steps.

$\vec{t}_1$	Pos./Orient.	$\Delta\vec{\epsilon}$	$\vec{t}_2$	Pos./Orient.	$\Delta\vec{\epsilon}$	$\Delta\vec{x}_{ij}$
[1,$\bar{1}$,$\bar{1}$]	($\frac{5}{4}$,$\frac{3}{4}$,$\frac{3}{4}$)[$\bar{1}$00]	[ϵ,$\bar{\epsilon}$,ϵ]	[$\bar{1}$,1,1]	(1,1,1)[0$\bar{1}$0]	[ϵ,ϵ,$\bar{\epsilon}$]	(0 , 0 , 0)
[1,$\bar{1}$,$\bar{1}$]	($\frac{5}{4}$,$\frac{3}{4}$,$\frac{3}{4}$)[$\bar{1}$00]	[ϵ,$\bar{\epsilon}$,ϵ]	[$\bar{1}$,1,1]	(1,1,1)[00$\bar{1}$]	[ϵ,$\bar{\epsilon}$,ϵ]	(0 , 0 , 0)
[1,$\bar{1}$,$\bar{1}$]	($\frac{5}{4}$,$\frac{3}{4}$,$\frac{3}{4}$)[$\bar{1}$00]	[ϵ,$\bar{\epsilon}$,ϵ]	[$\bar{1}$,$\bar{1}$,$\bar{1}$]	(1,$\frac{2}{4}$,$\frac{2}{4}$)[010]	[ϵ,ϵ,$\bar{\epsilon}$]	(0 ,-$\frac{2}{4}$,-$\frac{2}{4}$)
[1,$\bar{1}$,$\bar{1}$]	($\frac{5}{4}$,$\frac{3}{4}$,$\frac{3}{4}$)[$\bar{1}$00]	[ϵ,$\bar{\epsilon}$,ϵ]	[$\bar{1}$,$\bar{1}$,$\bar{1}$]	(1,$\frac{2}{4}$,$\frac{2}{4}$)[001]	[ϵ,$\bar{\epsilon}$,ϵ]	(0 ,-$\frac{2}{4}$,-$\frac{2}{4}$)
[1,$\bar{1}$,$\bar{1}$]	($\frac{5}{4}$,$\frac{3}{4}$,$\frac{3}{4}$)[010]	[$\bar{\epsilon}$,ϵ,ϵ]	[$\bar{1}$,1,1]	(1,1,1)[100]	[ϵ,ϵ,$\bar{\epsilon}$]	(0 , 0 , 0)
[1,$\bar{1}$,$\bar{1}$]	($\frac{5}{4}$,$\frac{3}{4}$,$\frac{3}{4}$)[010]	[$\bar{\epsilon}$,ϵ,ϵ]	[$\bar{1}$,1,1]	(1,1,1)[00$\bar{1}$]	[$\bar{\epsilon}$,ϵ,ϵ]	(0 , 0 , 0)
[1,$\bar{1}$,$\bar{1}$]	($\frac{5}{4}$,$\frac{3}{4}$,$\frac{3}{4}$)[010]	[$\bar{\epsilon}$,ϵ,ϵ]	[1,1,$\bar{1}$]	($\frac{6}{4}$,1,$\frac{2}{4}$)[$\bar{1}$00]	[ϵ,ϵ,$\bar{\epsilon}$]	($\frac{2}{4}$, 0 ,-$\frac{2}{4}$)
[1,$\bar{1}$,$\bar{1}$]	($\frac{5}{4}$,$\frac{3}{4}$,$\frac{3}{4}$)[010]	[$\bar{\epsilon}$,ϵ,ϵ]	[1,1,$\bar{1}$]	($\frac{6}{4}$,1,$\frac{2}{4}$)[001]	[$\bar{\epsilon}$,ϵ,ϵ]	($\frac{2}{4}$, 0 ,-$\frac{2}{4}$)
[$\bar{1}$,1,$\bar{1}$]	($\frac{3}{4}$,$\frac{5}{4}$,$\frac{3}{4}$)[100]	[ϵ,$\bar{\epsilon}$,ϵ]	[1,$\bar{1}$,1]	(1,1,1)[010]	[ϵ,ϵ,$\bar{\epsilon}$]	(0 , 0 , 0)
[$\bar{1}$,1,$\bar{1}$]	($\frac{3}{4}$,$\frac{5}{4}$,$\frac{3}{4}$)[100]	[ϵ,$\bar{\epsilon}$,ϵ]	[1,$\bar{1}$,1]	(1,1,1)[00$\bar{1}$]	[ϵ,$\bar{\epsilon}$,ϵ]	(0 , 0 , 0)
[$\bar{1}$,1,$\bar{1}$]	($\frac{3}{4}$,$\frac{5}{4}$,$\frac{3}{4}$)[100]	[ϵ,$\bar{\epsilon}$,ϵ]	[1,1,$\bar{1}$]	(1,$\frac{6}{4}$,$\frac{2}{4}$)[0$\bar{1}$0]	[ϵ,ϵ,$\bar{\epsilon}$]	(0 , $\frac{2}{4}$,-$\frac{2}{4}$)
[$\bar{1}$,1,$\bar{1}$]	($\frac{3}{4}$,$\frac{5}{4}$,$\frac{3}{4}$)[100]	[ϵ,$\bar{\epsilon}$,ϵ]	[1,1,$\bar{1}$]	(1,$\frac{6}{4}$,$\frac{2}{4}$)[001]	[ϵ,$\bar{\epsilon}$,ϵ]	(0 , $\frac{2}{4}$,-$\frac{2}{4}$)
[$\bar{1}$,1,$\bar{1}$]	($\frac{3}{4}$,$\frac{5}{4}$,$\frac{3}{4}$)[0$\bar{1}$0]	[$\bar{\epsilon}$,ϵ,ϵ]	[1,$\bar{1}$,1]	(1,1,1)[$\bar{1}$00]	[ϵ,ϵ,$\bar{\epsilon}$]	(0 , 0 , 0)
[$\bar{1}$,1,$\bar{1}$]	($\frac{3}{4}$,$\frac{5}{4}$,$\frac{3}{4}$)[0$\bar{1}$0]	[$\bar{\epsilon}$,ϵ,ϵ]	[1,$\bar{1}$,1]	(1,1,1)[00$\bar{1}$]	[$\bar{\epsilon}$,ϵ,ϵ]	(0 , 0 , 0)
[$\bar{1}$,1,$\bar{1}$]	($\frac{3}{4}$,$\frac{5}{4}$,$\frac{3}{4}$)[0$\bar{1}$0]	[$\bar{\epsilon}$,ϵ,ϵ]	[$\bar{1}$,$\bar{1}$,$\bar{1}$]	($\frac{2}{4}$,1,$\frac{2}{4}$)[100]	[ϵ,ϵ,$\bar{\epsilon}$]	(-$\frac{2}{4}$, 0 ,-$\frac{2}{4}$)
[$\bar{1}$,1,$\bar{1}$]	($\frac{3}{4}$,$\frac{5}{4}$,$\frac{3}{4}$)[0$\bar{1}$0]	[$\bar{\epsilon}$,ϵ,ϵ]	[$\bar{1}$,$\bar{1}$,$\bar{1}$]	($\frac{2}{4}$,1,$\frac{2}{4}$)[001]	[$\bar{\epsilon}$,ϵ,ϵ]	(-$\frac{2}{4}$, 0 ,-$\frac{2}{4}$)

VITA

Ph.D. Electrical Engineering, University of Washington, Seattle, WA (2008).

M.S. Electrical Engineering, University of Washington, Seattle, WA (2001).

B.S. Power Mechanical Engineering, National Tsing-Hua University, Taiwan (1999).